Chiral Vibrational Sum Frequency Generation Study of Water Around DNA

A Dissertation

Presented to the Faculty of the Graduate School

of Cornell University

In Partial Fulfillment of the Requirements for the Degree of

Doctor of Philosophy

by

Martin Luke McDermott

January 2017

Chiral Vibrational Sum Frequency Generation Study of Water Around DNA

Martin Luke McDermott, Ph. D.

Cornell University 2017

This dissertation presents the results of nonlinear spectroscopic studies with the goal to better understand the structure of water around DNA. The flexibility, function, and structure of DNA are partially dependent on the layers of surrounding water that hydrogen-bond to DNA. The first part of this dissertation describes chiral sum frequency generation spectroscopy (SFG) as a label-free, surface-specific, chiral-sensitive, nonlinear vibrational spectroscopy. By controlling the frequency and polarization of the beams involved in SFG experiments, chiral study of biomolecules and the water around them is possible.

The second part of this dissertation develops a robust method for chiral SFG using polarization multiplexing and self-referencing. The simple combination of a polarizer, achromatic waveplate, and beam displacer precisely controls the polarization of detected light. Through demonstration on archetypal achiral and chiral samples, the method is shown to increase signal-to-noise ratio, reduce detection time, and provide robustness to both interference and pure chiral SFG experiments.

The third part of this dissertation describes the application of the newly developed chiral SFG method to the water around DNA. A copper-free click reaction was adapted to bond DNA strands to visible- and infrared-transparent prisms. Two 24-base pair sequences of DNA—alternating thymines and adenines and alternating

guanines and cytosines—were studied dry and wet using chiral SFG. The nonzero chiral response across the OH stretch region indicated the heterogeneous structure of water around DNA. Waters bound strongly to DNA, waters hydrogen-bound to other waters, and waters with extremely weak hydrogen-bonding all appear in the chiral SFG spectrum. These results confirm the presence of a strongly bound minor groove spine of hydration, but they also could support "soft" waters in the major groove that are affected by the chirality of the DNA structure, but do not bind directly to the DNA. There is additional evidence of non-hydrogen bonding waters that may be facing non-polar structures in DNA. The vibrational spectroscopic access to only the waters around DNA in an *in situ*, room temperature experiment is unprecedented. Future work is discussed that capitalizes on the advances shown in this dissertation.

Biographical Sketch

Martin Luke McDermott was born in Bryn Mawr, Pennsylvania in 1988 to Edwin Joseph McDermott and Wenyu Tseng McDermott. He completed his high school diploma at Delaware County Christian School in 2006. At the Schreyer Honors College at the Pennsylvania State University in 2010, he completed a Bachelor of Science degree in Chemistry, a Bachelor of Arts degree with Honors in German Language Teaching, a Bachelor of Science degree in International Studies, as well as a Chinese Language Minor. From 2008 to 2009, Martin attended the University of Marburg in Germany. In 2010 he began his Ph.D. studies at Cornell University, where he joined the Petersen Group for his graduate research.

Acknowledgements

Special thanks to all the people who made the work included possible.

Table of Contents

List of Figures

List of Tables

Chapter 1: Introduction

Chirality

Chirality—"handedness"—is a subtle phenomenon with a vast reach. Biology and related fields have inherent interest in studying chirality, because of chiral amino acids, sugars, and other essential chiral molecules. Current research in chirality ranges from ancient chirality (studying the rise of homochirality in simulating evolution) to modern industrial chirality (controlling drug chirality in medicine) to extraterrestrial chirality (searching for signs of homochirality on distant planets).

Identifying chiral structures and monitoring interfacial interactions between chiral structures is essential for advancing our understanding of life's mechanics. Conventional chiroptic methods include linear spectroscopies such as circular dichroism (CD) and Raman optical activity. However, CD and other linear chiroptical spectroscopies monitor small indications of chirality on large achiral backgrounds. Often these linear chiroptical spectroscopies reach detection limits that preclude in situ experiments in real time.

As innovation in linear chiroptical spectroscopies reaps diminishing returns, researchers have exploited the chiroptic response of even-order nonlinear spectroscopies such as second-harmonic generation (SHG) and sum frequency generation (SFG). These spectroscopies are surface-selective and chiral-sensitive with detection limits that allow study of sub-monolayer concentrations at interfaces. The first part of this dissertation describes technical advancements of chiral SFG made in our lab, while the second part describes new applications.

Water as a Biomolecule

Biological molecules are often portrayed on a blank background as if existing in a vacuum. However, all of biology occurs in water—the matrix of life.[1,2] Indeed, biomolecules are generally inactive in the absence of water. At biological interfaces—the surface of a cell, protein, or other biomolecule—there is a layer of non-bulk water that exhibits unique behavior dependent on the local environment.[3] In a crowded cell, interfacial water coats an enormous surface area; there is essentially no bulk water in the cell. To understand the structure, stability, and function of cellular processes, we must understand interfacial water in biology.

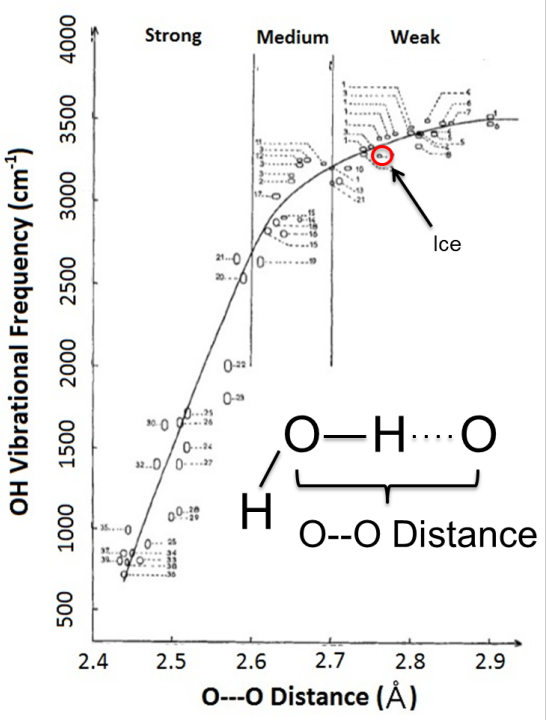

Figure 1. OH Stretch Frequency vs. O--O Distance. *OH stretch frequency is a sensitive probe of hydrogen bonding. Here the correlation between OH stretch frequency and O--O distance is shown for solids. Figure adapted from Novak.*[4]

The vibrational spectrum of water and particularly the OH stretch is an excellent probe of local structure and dynamics. The frequency of the OH stretch shifts in response to the local hydrogen-bonding environment, as shown in **Figure *1***.[4–7] The dynamics of the OH stretch in a time-resolved spectroscopy can also report on the local hydrogen-bonded environment and dynamics.[8–11] Vibrational SFG with a resonant infrared probe provides an interface-specific or chiral-specific vibrational spectrum. Therefore, vibrational SFG spectroscopy of the OH stretch frequency is a uniquely powerful tool in the study of water in biology.

Water around DNA

The surface of DNA has major and the minor grooves of different widths and depths that present many functional groups that interact with water, including ionic phosphate groups and polar sugars on the DNA backbone and nucleic bases. Consequently, the first layer of water around DNA is heterogeneous and different from bulk water.

The interfacial water stabilizes the DNA structure. For example, in the absence of adequate solvating waters (i.e. at least 20 water molecules per base pair), the structure of DNA transforms from the biologically relevant double helix B-form to the looser coiled A-form.

Interfacial water also enables DNA function. Water actively mediates molecular recognition between DNA and binding partners, using its flexible hydrogen-bonding network to probe the energy landscape.[12] Interfacial water patterns are a sequence-specific "hydration fingerprint" that facilitates the strong protein binding necessary for genetic integrity.[13]

A specific example of DNA's interfacial water is the "spine of hydration." X-ray diffraction and NMR experiments have found a remarkably stable zigzag "spine" of first- and second-shell hydration running along the bottom of the DNA minor groove, particularly at adenine-thymine sequences. Protein binding in the minor groove (especially in the narrow minor groove at AT sequences) is driven by the large entropy increase of displacing the "spine of hydration."

In efforts to understand the role of water in DNA function and structure, minor groove waters and other DNA-bound waters have been a popular focus of study as described below. However, many aspects of the role of water are not yet established. Part of this dissertation describes the application of vibrational chiral SFG to the interfacial water helix around DNA.

Previous Spectroscopy on the Hydration of DNA

In the early 2000's, Ahmed Zewail and coworkers completed high-profile work on the hydration of DNA using time-dependent fluorescence stokes shift experiments.[14,15] In these experiments, a fluorescent DNA minor groove binder was excited. The resultant fluorescence was monitored by fluorescence upconversion, which provided the time resolution. The probe's instantaneous (Franck–Condon) transition places an electric field on the solvent molecules. The solvent rearranges, giving rise to a red shift in the fluorescence. The dynamics of the Stokes shift reports on the solvent dynamics. In the Zewail experiment, a multiexponential fit produced several time scales, among which 20 ps was assigned to "dynamically ordered water."

However, the assignment of this extraordinary slow water (about 20 times slower than bulk) has been challenged.[16–20] As with many electronic spectroscopies, the

Stokes shift is not molecularly specific. The Stokes shift reflects structural dynamics of the entire environment around the fluorescent probe—including both the DNA structure and the water shell. Specifically, MD simulations by Steven Corcelli suggest that the slowest time scales are the reorganization of the DNA itself.[18] An unambiguous extraction of the water response from the Stokes shift data is impossible. Furthermore, the invasive nature of the probe alters the DNA and its hydration geometries.[21]

In contrast, vibrational spectroscopy is a direct probe of water structure. As mentioned above, the OH stretching frequency of water is sensitive to the hydrogen-bonding environment around the water.[6,7] Generally, more hydrogen-bonding or stronger hydrogen bonds cause a red shift in the OH stretch frequency as shown in **Figure 2**.[4,7]

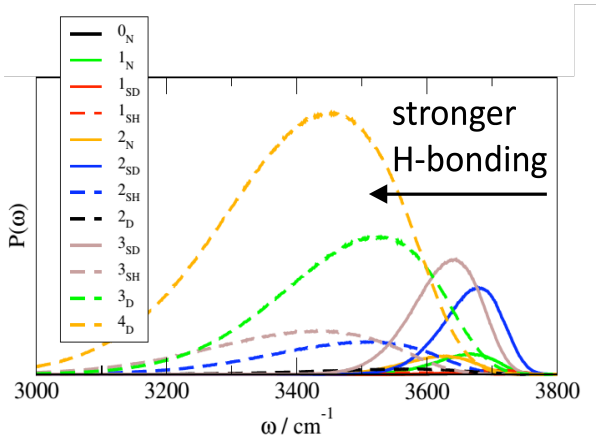

Figure 2. Water stretch frequency and hydrogen bonding environment
More hydrogen bonding generally leads to red shift in the OH stretch of water. Skinner and coworkers describe the possible H-bonding environments of a water with the nomenclature $\#_X$, where # represents the total number of hydrogen bonds the water molecule participates in and X represents the type of hydrogen bonding: $\#_S$ when the water is a single H-bond donor, $\#_D$ when the water is a double H-bond donor, and $\#_N$ when the water is a non-donor. The effect of each H-bonding environment is shown in their figure here.[6,7]

While all water-water hydrogen bonding is considered weak compared to the full range of hydrogen-bonding strengths, there are sub-categorizations. A dangling, non-hydrogen bonded OH at a water-air surface will stretch at 3700 cm^{-1}. A weakly hydrogen-bonded OH in water with about 3 partners or less will stretch at 3400 cm^{-1}. A relatively strong water-water hydrogen-bonded OH will stretch at 3200 cm^{-1}. The 2700-3200 cm^{-1} region would be medium strength hydrogen bonds and unlikely to be due to water-water H-bonding. Stretches below 2700 cm^{-1} would be strong hydrogen bonds. Later experiments described here see ~3000 cm^{-1} OH stretching in water around DNA, which is likely due to water hydrogen-bonded to DNA. In short, OH stretch vibrations in the infrared 3000-3700 cm^{-1} region can be matched with specific water hydrogen-bonding environments.

In addition to its frequency, the dynamics of an OH stretch vibration can also report on the hydrogen bonding environment. Bulk vibrational spectroscopy of hydrated DNA by Thomas Elsaesser and coworkers observed OH stretch spectral diffusion using 2DIR (two-dimensional infrared spectroscopy) experiments.[19,22] In the experiments, approximately 20 μm thick DNA hydrogel films were made of 23 base pair DNA with cetyltrimethylammonium counterions. In a hydration controlled sample cell, 2DIR spectra were collected at specific humidity levels and time delays. The water OH stretch showed spectral diffusion about 2.5 times slower than bulk water (about 250 fs vs. less than 100 fs). In the absence of another timescale less than 1 ps, the authors claimed a rigid first solvation shell that must have spectral diffusion slower than 1 ps (i.e. outside the time scale of their experiment).

The main complication of any bulk vibrational study of hydration is the large

infrared absorbance of bulk water. Elsaesser and coworkers' solution to this problem is dehydrated hydrogel thin films. Although bulk water is indeed removed, the remaining structure of the hydrogel does not necessarily replicate biology. As discussed above, DNA transforms in the absence of adequate solvation. There is also no way to know that the probed waters are at the DNA surface and not, for example, solvating the counterion. Therefore, a better way to remove the signal from bulk water is to use vibrational SFG spectroscopy, which can be surface-specific and chiral-specific.

Dissertation Organization

First efforts at studying hydration of DNA with chiral SFG called for more rigorous experimental methods. Chapter 2 first outlines the mathematical background of SFG and chiral SFG, and then reports the development of a robust, self-referencing method of chiral sum frequency generation spectroscopy. The method takes advantage of polarization multiplexing to interfere chiral and achiral signals. Self-referencing calibrates each sample. We demonstrate the new method by comparing results from chiral and achiral samples.

Chapter 3 presents the use of the newly developed chiral SFG method to study water around DNA. The chiral OH stretch SFG response of water around two 24-base pair sequences of DNA is collected. The chiral SFG response spans the OH stretch region, lending new insight into the heterogeneity of the waters most closely associated with DNA. Interpretations of the new spectral information are discussed.

Chapter 4 concludes the main portion of this dissertation, discussing the future outlook of chiral SFG experiments based on this dissertation.

Following the conclusion, three appendices discuss ongoing work on interfacial

water and other topics. Appendix A describes the synthesis of a metal carbonyl SAM as a vibrational SFG probe of hydration. Appendix B chronicles the development of 2DIR lipid membrane samples in collaboration with the Freed group. Appendix C outlines work on 2DIR investigations of aqueous proton transfer.

Chapter 2: Development of Robust, Self-Referencing Chiral SFG

Sum Frequency Generation

Sum frequency generation (SFG) is a nonlinear optical phenomenon in which two incoming photons induce a polarization, $P^{(2)}$, that oscillates at the sum of their two frequencies. The polarization then emits a third photon at the sum frequency. SFG is categorized as a second-order nonlinear process: the process depends on the square magnitude of the second order susceptibility, $\chi^{(2)}$, and the intensity of two incoming photons.

$$I_{SFG} \propto \left|\chi^{(2)} E_1 E_2\right|^2 \tag{1}$$

SFG is also known as a three-wave mixing process: $\chi^{(2)}$ is a third-rank tensor and the process involves three photons in total (two annihilated and one generated). SFG is a parametric process; the initial and final energy levels are identical.

Incident photons (at frequencies ω_a and ω_b) with electric fields $\vec{E}_{\omega_a}$ and $\vec{E}_{\omega_a}$ impinge on a sample and induce a second-order polarization, $\vec{P}^{(2)}_{\omega_a+\omega_b}$, that is proportional to the second-order nonlinear susceptibility tensor, $\chi^{(2)}$. This second-order polarization, $\vec{P}^{(2)}_{\omega_a+\omega_b}$, oscillates at the sum of the two incident frequencies, $\omega_a + \omega_b$, and emits a photon with electric field, $\vec{E}_{\omega_a+\omega_b}$, in the direction determined by conservation of the momentum of the incident photons.

SFG and other even-order nonlinear processes occur only in non-centrosymmetric media.[23] Under the electric dipole approximation (i.e. ignoring multipoles and magnetic moments), centrosymmetric media include bulk gas, liquids, and most solids. Useful exceptions are birefringent crystals such as barium borate (BaB_2O_4), calcite ($CaCO_3$), and lithium niobate ($LiNbO_3$). A simple proof can show that

the second-order susceptibility, $\chi^{(2)}$, vanishes in centrosymmetric media. Let I_{inv} be the inversion operator.

$$\vec{P}^{(2)}_{\omega_a+\omega_b} = \chi^{(2)}\,\vec{E}_{\omega_a}\,\vec{E}_{\omega_b} \tag{2}$$

$$I_{inv}[\vec{P}^{(2)}_{\omega_a+\omega_b} = \chi^{(2)}\,\vec{E}_{\omega_a}\,\vec{E}_{\omega_b}] \tag{3}$$

For centrosymmetric media: $I_{inv}[\chi^{(2)}] = \chi^{(2)}$ (4)

$$\therefore -\vec{P}^{(2)}_{\omega_a+\omega_b} = \chi^{(2)}(-\vec{E}_{\omega_a})(-\vec{E}_{\omega_b}) \tag{5}$$

$$-\vec{P}^{(2)}_{\omega_a+\omega_b} = \chi^{(2)}\,\vec{E}_{\omega_a}\,\vec{E}_{\omega_b} \tag{6}$$

$$-\vec{P}^{(2)}_{\omega_a+\omega_b} = \vec{P}^{(2)}_{\omega_a+\omega_b} \tag{7}$$

$$\therefore \chi^{(2)} = 0 \tag{8}$$

An important case of broken centrosymmetry is interfaces between two centrosymmetric media. Although both bulk media produce no SFG, the broken symmetry at the interface produces a surface-specific SFG signal. The depth of the origin of the signal is simply the depth of the net polar orientation. For the neat water-vapor interface, heterodyned SFG experiments suggest that the SFG signal originates mainly from the first monolayer (0.3 nm).[24,25] For more complex surfaces (e.g. charged surfaces or ionic solutions), the surface can extend to a few water layers.[26,27]

When used for spectroscopy, SFG employs resonance to generate molecule-specific signals. In this dissertation, a broadband infrared light source is centered on the resonance of interest (e.g. OH stretch) and upconverted by SFG to a detected visible photon. Mathematically, this process, also known as vibrational SFG, can be explained rigorously as an infrared excitation followed by an anti-Stokes Raman scattering, as

shown in the electric dipole approximation of SFG below.

Electric Dipole Approximation of SFG

Within the electric dipole approximation, linear (Raman) polarizability is:

$$\alpha_{ij} = \frac{\partial^2 H}{\partial E_i \, \partial E_j} \tag{9}$$

where α is the polarizability, H is the Hamiltonian of the sample, and E_i is the electric field of the *i*th photon.

When the strength of the field is increased, additional anharmonic contributions become significant. The hyperpolarizability, β, is given by:

$$\beta_{ijk} = \frac{\partial^3 H}{\partial E_i \, \partial E_j \, \partial E_k} \tag{10}$$

These formulae come with the caveat that they only apply in the adiabatic limit. To get around this limit requires time-dependent perturbation theory and sum-over-states expressions. The easiest way to picture this is by drawing energy-level diagrams and then writing out the equations to connect them. (Feynman diagrams are another popular strategy). The energy level diagrams are shown in **Figure *3***. With three different energy beams, there are six (3!) possible pathways for the triple product of transition moments that make up the hyperpolarizability. By changing the time ordering, the six possible pathways are quickly illustrated. When the energy level is far from resonance, it is shown as a dashed line indicating a virtual state. The first energy level is the sum over states *n* and the second energy level is the sum over states *m*.

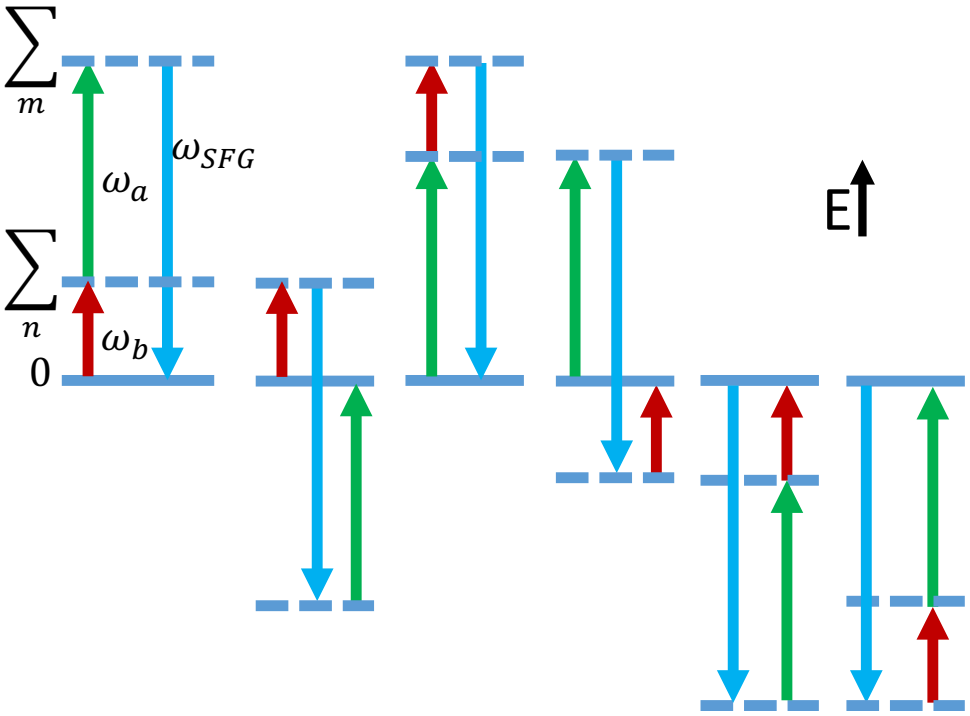

Figure 3. Sum Frequency Generation energy level diagrams
The six possible energy level diagrams for a given set of three photons. Energy increases upwards and time increases to the right within each pathway. The first energy level is a sum over states n and the second energy level is a sum over states m.

For a signal at ω_{SFG} with incoming frequencies ω_a and ω_b, there will be six possible orderings of the three frequencies. The six energy level diagrams correspond to the following six terms:

$$\beta^{ijk}(-\omega_{SFG};\omega_a,\omega_b) \tag{11}$$
$$= -\frac{1}{4\hbar^2}\sum_{n,m}\Big\{\mu^i_{0m}\mu^k_{mn}\mu^j_{n0}\Big[\frac{1}{(\omega_m + \omega_{SFG} + i\Gamma_m)(\omega_n + \omega_a + i\Gamma_n)}$$
$$+\frac{1}{(\omega_m - \omega_{SFG} - i\Gamma_m)(\omega_n - \omega_a - i\Gamma_n)}\Big]$$
$$+\mu^j_{0m}\,\mu^k_{mn}\,\mu^i_{n0}\Big[\frac{1}{(\omega_m - \omega_a - i\Gamma_m)(\omega_n - \omega_{SFG} - i\Gamma_n)}$$
$$+\frac{1}{(\omega_m + \omega_a + i\Gamma_m)(\omega_n + \omega_{SFG} + i\Gamma_n)}\Big]$$
$$+\mu^i_{0m}\,\mu^j_{mn}\,\mu^k_{n0}\Big[\frac{1}{(\omega_m + \omega_{SFG} + i\Gamma_m)(\omega_n + \omega_b + i\Gamma_n)}$$
$$+\frac{1}{(\omega_m - \omega_{SFG} - i\Gamma_m)(\omega_n - \omega_b - i\Gamma_n)}\Big]$$
$$+\mu^k_{0m}\,\mu^j_{mn}\,\mu^i_{n0}\Big[\frac{1}{(\omega_m - \omega_b - i\Gamma_m)(\omega_n - \omega_{SFG} - i\Gamma_n)}$$
$$+\frac{1}{(\omega_m + \omega_b + i\Gamma_m)(\omega_n + \omega_{SFG} + i\Gamma_n)}\Big]$$
$$+\mu^k_{0m}\,\mu^i_{mn}\,\mu^j_{n0}\Big[\frac{1}{(\omega_m - \omega_b - i\Gamma_m)(\omega_n + \omega_a + i\Gamma_n)}$$
$$+\frac{1}{(\omega_m + \omega_b + i\Gamma_m)(\omega_n - \omega_a - i\Gamma_n)}\Big]$$
$$+\mu^j_{0m}\,\mu^i_{mn}\,\mu^k_{n0}\Big[\frac{1}{(\omega_m - \omega_a - i\Gamma_m)(\omega_n + \omega_b + i\Gamma_n)}$$
$$+\frac{1}{(\omega_m + \omega_a + i\Gamma_m)(\omega_n - \omega_b - i\Gamma_n)}\Big]\Big\}$$

where ω_m and ω_n are the frequencies matching the *0* to *m* energy and *0* to *n* energy and μ^k_{0m} is the transition dipole moment for the *0* to *m* transition when matched by the *k*th photon (the SFG photon in this nomenclature) and Γ_n is the damping coefficient for the *n*th level.[a]

[a] The sign on the damping term (i.e. $i\Gamma$) must match the sign on the term before it (e.g. ω_b). This is the only sign that works with stimulated emission.[28]

Close to molecular resonances, many terms are negligible. When ω_b is resonant with energy level n, the dominant terms simplify to:

$$\beta^{ijk}\left(-\omega_{SFG};\omega_a,\underline{\omega_b}\right) = -\frac{1}{\hbar^2}\sum_{m,n}\left\{\frac{\mu^i_{0m}\,\mu^j_{mn}\,\mu^k_{n0}}{(\omega_m - \omega_{SFG} - i\Gamma_m)(\omega_n - \omega_b - i\Gamma_n)} + \frac{\mu^j_{0m}\,\mu^i_{mn}\,\mu^k_{n0}}{(\omega_m + \omega_a + i\Gamma_m)(\omega_n - \omega_b - i\Gamma_n)}\right\} \tag{12}$$

Grouping the terms into pairs sharing common initial to first virtual state transitions leads to the molecular hyperpolarizability rewritten using definitions for Raman and one-photon transition dipoles.

$$\beta^{ijk}\left(-\omega_{SFG};\omega_a,\underline{\omega_b}\right) = -\frac{1}{2\hbar}\sum_{n}\frac{\mu^k_{n0}}{(\omega_n - \omega_b - i\Gamma_n)}\sum_{m}\frac{1}{\hbar}\left\{\frac{\mu^i_{0m}\,\mu^j_{mn}}{(\omega_m - \omega_{SFG} - i\Gamma_m)} + \frac{\mu^j_{0m}\,\mu^i_{mn}}{(\omega_m + \omega_a + i\Gamma_m)}\right\} \tag{13}$$

where the term summing over energy level *m* is the sum-over-states expression for anti-Stokes Raman, which leads to the further simplification:

$$\beta^{ijk}\left(-\omega_{SFG};\omega_a,\underline{\omega_b}\right) = -\frac{1}{2\hbar}\sum_{n}\frac{\left(\alpha^{ij}_{0n}\right)_{AR}\mu^k_{n0}}{\omega_n - \omega_b - i\Gamma_n} \tag{14}$$

Close to vibrational resonance, the molecular tensor in Equation 14 is given by the direct product of the anti-Stokes Raman tensor and the one-photon transition moment.[28] The other terms in Equation 11 reduce to a nonresonant contribution that is not frequency-dependent over the vibrational frequency range.

Chiral SFG vs. Linear Chiral Spectroscopies

Put simply, chiral SFG is possible because chirality is a form of non-centrosymmetry. Therefore, a chiral SFG signal can be collected with no achiral

background, which contrasts with linear chiral spectroscopy.

The two most common linear chiroptical measurements are circular dichroism (CD) and optical rotatory dispersion (ORD). Both of these rely on non-local effects over the length of the molecule. The strength of their rotational effect, R, is dependent on electric-dipolar and magnetic-dipolar transitions:

$$R = \vec{\mu} \cdot \vec{m} \tag{15}$$

Neither the transition dipole moment μ nor the Raman tensor α alone can describe the chiral symmetry. Therefore the transition dipole moment (as shown in Equation 15) or the Raman tensor (not shown) must couple to a magnetic dipole.[29] Magnetic dipole coupling is usually weak, which explain why linear chiroptical effects are usually very weak. Often the effect is only about 0.1% of the absorbance, because of the weakness of the magnetic-dipolar transition. With the large achiral absorbance and weak chiral signal, signal-to-noise difficulties can arise.

In contrast, second-order nonlinear effects such as chiral SFG give chiral-specific signals that arise in the electric dipole approximation. The chiral SFG signal is proportional to the vector product of three transition dipole moments (or one transition dipole moment and the Raman tensor) as shown above in Equations 12-14. The vector product of these three transition dipole moments is much stronger than the magnetic-dipole coupling for linear chiral measurements (Equation 15). Intensity differences in second-order effects can therefore be several orders of magnitude larger than their linear optical activity measurement counterparts. Depending on the chirality of the sample, the chiral SFG response can be more than 10% of the magnitude of the corresponding achiral SFG signal.

Perhaps more importantly, the intrinsic chirality response of stereocenters dominates linear chiroptical signals, but the structural or orientational chirality of achiral molecules arranged in chiral structures dominates second-order nonlinear chiroptical signals.[30–32] Intrinsic chirality is defined as the difference between the hyperpolarizability, β, and its mirror image. In other words, intrinsic chirality occurs when the transition dipole moment, μ, does not lie in the plane of the elements of the Raman tensor, α. Intrinsic chirality originates from a single chromophore. However, SFG experiments occur over an ensemble of chromophores. To a first-order approximation, the SFG response is a coherent summation or orientational average over the contribution of each chromophore. Even after accounting for the intrinsic chirality of individual chromophores, there is often chirality left over in the SFG response. This chirality originates from the orientation of achiral chromophores into macroscopically chiral structures. The origin of this structural or orientational chirality is analogous to a propeller where the chirality in the ensemble originates from the relative orientation of the blades.[33]

Third order effects probing chirality have been seen,[34–36] but their intensity suffers from the same limitation as linear methods: dependence on the weak magnetic-dipolar transition.

Chiral vs. Achiral SFG

In a typical SFG experiment, a nonresonant visible photon and a resonant infrared photon induce a non-linear polarization in the sample that emits a detected photon at the sum frequency.

$$\omega_{SFG} = \omega_{vis} + \omega_{IR} \tag{16}$$

SFG intensity depends on the second-order polarization's square magnitude.

$$I_{SFG} \propto \left|P^{(2)}\right|^2 \tag{17}$$

In turn, the polarization that generates the output sum frequency depends on the visible and infrared incident electric fields as well as the effective second-order nonlinear susceptibility.

$$P^{(2)} = \chi^{(2)}_{eff} E_{vis} E_{IR} \tag{18}$$

For vibrational SFG, the second-order susceptibility, $\chi^{(2)}$, consists of a non-resonant term, $\chi^{(2)}_{NR}$, and a sum of vibrationally resonant terms, $\chi^{(2)}_i$:

$$\chi^{(2)} = \chi^{(2)}_{NR} + \sum_i \chi^{(2)}_i = \chi^{(2)}_{NR} + \sum_i \frac{A_i}{\omega_{IR} - \omega_i - i\Gamma_i} \tag{19}$$

where A_i is the SFG transition moment and Γ_i is the line width of the *i*th transition.

Within the xyz lab frame of reference, there are 27 tensor elements in the second-order nonlinear susceptibility, χ^2 (i.e. a third-rank tensor). In this dissertation, monolayers at the solid-air or solid-liquid surface are studied. For achiral molecules, a reasonable approximation for the overall surface structure is an isotropic achiral surface with $C_{\infty v}$ symmetry, giving four independent (seven total) nonzero $\chi^{(2)}_{eff}$ elements:

$$\chi^{(2)}_{xxz} = \chi^{(2)}_{yyz}$$

$$\chi^{(2)}_{xzx} = \chi^{(2)}_{yzy}$$

$$\chi^{(2)}_{zxx} = \chi^{(2)}_{zyy}$$

$$\chi^{(2)}_{zzz}$$

However, a chiral surface will have different symmetry considerations.

Orthogonal elements, $\chi^{(2)}_{IJK,(I\neq J\neq K)}$ are characteristic for chiral surfaces. A chiral surface with C_∞ symmetry adds an additional six nonzero elements:

$$\chi^{(2)}_{xyz}, \chi^{(2)}_{xzy}, \chi^{(2)}_{yxz}, \chi^{(2)}_{yzx}, \chi^{(2)}_{zxy}, \chi^{(2)}_{zyx}$$

The origin of the chiral sensitivity of the SFG signal has been discussed previously.[30] Simply put, chirality is another form of non-centrosymmetry and chiral materials have even-order nonlinear responses. Second-order nonlinear versions of CD, ORD, and LD were shown with second harmonic generation two decades ago.[32,37–39] Pioneers of sum frequency generation followed with chiral SFG from bulk liquids.[40] Later work demonstrated chiral SFG at surfaces by studying amide I vibrations of two proteins at a solid-liquid interface.[41] The electric dipole approximation was used to explain the origin of the surface chiral sum frequency signal.[30,33] As noted above, chirality in even-order nonlinear optics does not require chirality within a chromophore. Instead, chirality in SFG can arise from macromolecular chiral orientation (i.e. chiral assemblies of achiral chromophores).

At the experimental level, waveplates and polarizers control the polarization of each of the three beams (sum frequency, visible, and infrared) to be parallel (*p* for the German *parallel*) or perpendicular (*s* for the German *senkrecht*) relative to the plane of incidence of the visible and infrared beams on the sample. Polarizations are listed in descending order of photon frequency (e.g. the *ssp* experiment shown in **Figure *4*** has *s*-polarized SFG, *s*-polarized visible, and *p*-polarized IR beams). Hence, there are eight (2^3) possible combinations for the polarization settings:

1) *ssp*

2) *sps*

3) *pss*

4) *ppp*

5) *sss*

6) *psp*

7) *spp*

8) *pps*

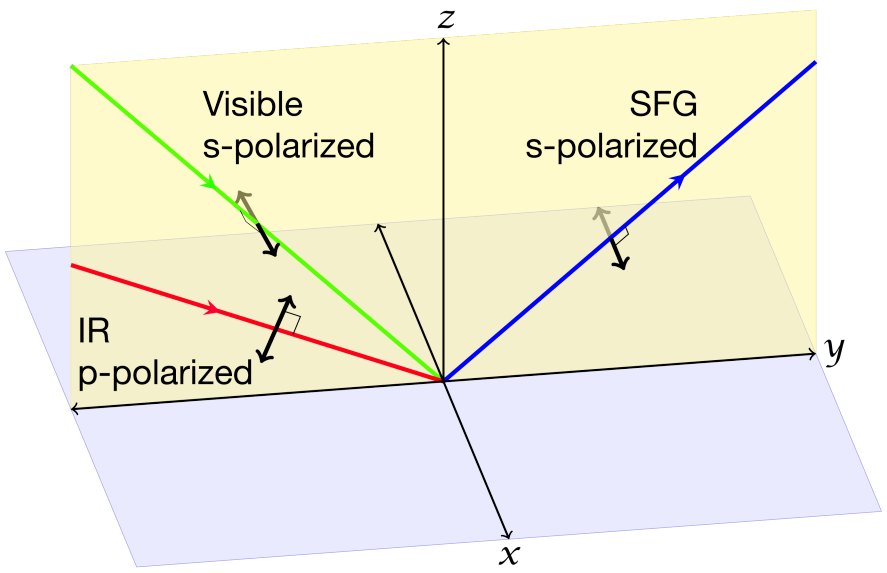

Figure 4. *ssp* polarization illustration

For a surface that is symmetric under rotation about the surface normal (i.e. $C_{\infty v}$ or C_{∞}), four of the possible SFG polarization combinations—*ppp*, *ssp*, *sps*, *pss*—measure vibrations from achiral structures and three combinations—*psp*, *spp*, *pps*—measure vibrations from chiral structures. *sss* is completely in the plane of the sample and is zero. A rule of thumb is that the achiral combinations always have an odd number of *p*-polarized beams, while the chiral combinations have an even number of *p*-polarized beams. Comprehensive treatments of chiral SFG theory are available in the literature.[29–31,33,42–44]

The seven second-order susceptibilities can be expressed in terms of the thirteen chiral and achiral $\chi^{(2)}$ elements.

Achiral:

$$\chi_{ssp}^{(2)} = L_{yy}(\omega_{SFG})L_{yy}(\omega_{vis})L_{zz}(\omega_{IR})\sin\alpha_{IR}\,\chi_{yyz}^{(2)} \tag{20}$$

$$\chi_{sps}^{(2)} = L_{yy}(\omega_{SFG})L_{zz}(\omega_{vis})L_{yy}(\omega_{IR})\sin\alpha_{vis}\,\chi_{yzy}^{(2)} \tag{21}$$

$$\chi_{pss}^{(2)} = L_{zz}(\omega_{SFG})L_{yy}(\omega_{vis})L_{yy}(\omega_{IR})\sin\alpha_{SFG}\,\chi_{zyy}^{(2)} \tag{22}$$

$$\chi_{ppp}^{(2)} \tag{23}$$

$$= -L_{xx}(\omega_{SFG})L_{xx}(\omega_{vis})L_{zz}(\omega_{IR})\cos\alpha_{SFG}\cos\alpha_{vis}\sin\alpha_{IR}\,\chi_{xxz}^{(2)}$$

$$- L_{xx}(\omega_{SFG})L_{zz}(\omega_{vis})L_{xx}(\omega_{IR})\cos\alpha_{SFG}\sin\alpha_{vis}\cos\alpha_{IR}\,\chi_{xzx}^{(2)}$$

$$+ L_{zz}(\omega_{SFG})L_{xx}(\omega_{vis})L_{xx}(\omega_{IR})\cos\alpha_{SFG}\sin\alpha_{vis}\cos\alpha_{IR}\,\chi_{zxx}^{(2)}$$

$$+ L_{zz}(\omega_{SFG})L_{zz}(\omega_{vis})L_{zz}(\omega_{IR})\sin\alpha_{SFG}\sin\alpha_{vis}\sin\alpha_{IR}\,\chi_{zzz}^{(2)}$$

Chiral:

$$\chi_{psp}^{(2)} = L_{zz}(\omega_{SFG})L_{yy}(\omega_{vis})L_{xx}(\omega_{IR})\sin\alpha_{SFG}\cos\alpha_{IR}\,\chi_{zyx}^{(2)} \tag{24}$$

$$- L_{xx}(\omega_{SFG})L_{yy}(\omega_{vis})L_{zz}(\omega_{IR})\cos\alpha_{SFG}\sin\alpha_{IR}\,\chi_{xyz}^{(2)}$$

$$\chi_{spp}^{(2)} = L_{yy}(\omega_{SFG})L_{zz}(\omega_{vis})L_{xx}(\omega_{IR})\sin\alpha_{vis}\cos\alpha_{IR}\,\chi_{yzx}^{(2)} \tag{25}$$

$$- L_{yy}(\omega_{SFG})L_{xx}(\omega_{vis})L_{zz}(\omega_{IR})\cos\alpha_{SFG}\sin\alpha_{vis}\,\chi_{yxz}^{(2)}$$

$$\chi_{pps}^{(2)} = L_{zz}(\omega_{SFG})L_{xx}(\omega_{vis})L_{yy}(\omega_{IR})\sin\alpha_{SFG}\cos\alpha_{vis}\,\chi_{zxy}^{(2)} \tag{26}$$

$$- L_{xx}(\omega_{SFG})L_{zz}(\omega_{vis})L_{yy}(\omega_{IR})\cos\alpha_{SFG}\sin\alpha_{vis}\,\chi_{xzy}^{(2)}$$

where α_i is the incident/reflected angle of laser beam *i* in relation to the surface normal and $L_{nn}(\omega_i)$ are diagonal elements of the Fresnel matrix determined by the two refractive indices of the interface.

When ω_{SFG} and ω_{vis} are both far from resonance, the antisymmetric Raman polarizability is often negligible (under the adiabatic approximation for electron-vibration coupling).[45] With only the symmetric Raman polarizability,

$$\chi_{xyz}^{(2)} = \chi_{yxz}^{(2)} \tag{27}$$

$$\chi^{(2)}_{zxy} = \chi^{(2)}_{xzy} \tag{28}$$

$$\chi^{(2)}_{yzx} = \chi^{(2)}_{zyx} \tag{29}$$

C_4 is a subgroup of the C_∞ point group and provides the useful relations $x \to -y$ and y$\to x$, which leads to:

$$\chi^{(2)}_{xyz} = \chi^{(2)}_{(-y)xz} \tag{30}$$

$$\chi^{(2)}_{xyz} = -\chi^{(2)}_{yxz} \tag{31}$$

$$\chi^{(2)}_{xyz} = -\chi^{(2)}_{xyz} \tag{32}$$

$$\chi^{(2)}_{xyz} = 0 \tag{33}$$

$$\chi^{(2)}_{yxz} = 0 \tag{34}$$

Similarly,

$$\chi^{(2)}_{zxy} = \chi^{(2)}_{z(-y)x} \tag{35}$$

$$\chi^{(2)}_{zxy} = -\chi^{(2)}_{zyx} \tag{36}$$

These produce the following $\chi^{(2)}_{eff}$ that all depend on the same chiral susceptibility element, $\chi^{(2)}_{zyx}$.[42]

$$\chi^{(2)}_{psp} = L_{zz}(\omega_{SFG})L_{yy}(\omega_{vis})L_{xx}(\omega_{IR}) \sin\alpha_{SFG} \cos\alpha_{IR}\, \chi^{(2)}_{zyx} \tag{37}$$

$$\chi^{(2)}_{spp} = L_{yy}(\omega_{SFG})L_{zz}(\omega_{vis})L_{xx}(\omega_{IR}) \sin\alpha_{vis} \cos\alpha_{IR}\, \chi^{(2)}_{zyx} \tag{38}$$

$$\chi^{(2)}_{pps} = L_{xx}(\omega_{SFG})L_{zz}(\omega_{vis})L_{yy}(\omega_{IR}) \cos\alpha_{SFG} \sin\alpha_{vis}\, \chi^{(2)}_{zyx} - L_{zz}(\omega_{SFG})L_{xx}(\omega_{vis})L_{yy}(\omega_{IR}) \sin\alpha_{SFG} \cos\alpha_{vis}\, \chi^{(2)}_{zyx} \tag{39}$$

Therefore, the choice between *spp*, *psp*, and *pps* depends only on interface-

dependent Fresnel factors, beam angles, and optics.[b]

State of Affairs in Chiral SFG

As with most spectroscopies, the uses of chiral SFG are limited by feasible signal-to-noise ratios. In particular, the existence of systematic experimental errors caused by imperfect alignment complicate chiral SFG. Recent research in chiral SFG has concentrated on expanding the signal-to-noise limits to allow study of faster processes and more dilute or weaker chromophores. For example, heterodyned chiral SFG amplifies signals significantly.[46,47] Doubly resonant electronic and vibrational-resonant chiral SFG used a tunable visible beam to study cytochrome c.[48] However, both of these advances significantly complicate the experiment, requiring a local oscillator for heterodyning and a tunable visible beam for doubly resonant chiral SFG. In contrast, the robust, self-referencing chiral SFG method described below is simple, cheap (roughly $1000), and can be incorporated into virtually any SFG spectrometer (including heterodyned, doubly resonant or more complicated spectrometers). There is no reason why the method should not be implemented in all current chiral SFG spectrometers. The method would greatly improve the reliability of chiral SFG and make chiral experiments more accessible as SFG spectrometers become more available.

The development of a new method of chiral SFG detection is recorded below and in published work.[49] The method greatly improves the signal-to-noise ratio and more importantly removes systematic errors that are otherwise difficult to detect in chiral SFG measurements. The improvements are due to the simultaneous measuring of two

[b] In achiral SFG the *sps* and *pss* spectra contain equivalent information when assuming a symmetric Raman polarizability tensor.

polarizations of the SFG signal (polarization-multiplexing) that diminish noise from laser fluctuations and the use of self-referencing that eliminate the systematic errors.

Previous Chiral SFG

Recent work in chiral SFG at surfaces has had several data collection schemes. The simplest method is to isolate a purely chiral SFG polarization. Many studies have used the psp polarization method. Experiments on the secondary structure of proteins at liquid-air interfaces used the strength and density of amide I and NH vibrational chromophores.[50–53] A less dense protein sample at supported planar lipid bilayers enhanced the chiral signal with visible- and infrared-resonant SFG of protein amide I signals.[48] Another study of the CH stretches of the air-limonene surface heterodyned the chiral SFG signal with a nonresonant local oscillator.[46]

Although pure chiral SFG signals can be on the same order of magnitude as achiral SFG signals, the chiral SFG signals are usually weak in absolute terms, due to dilute or weak chromophores. Furthermore, collecting only the pure chiral SFG signal relies on very accurate control of polarizations. In cases where achiral structures greatly outnumber chiral structures, the pure chiral experiment must make certain that the stronger achiral signal is not leaking into the chiral polarization detection.[54] Many experimental setups have no absolute determination of polarization and must rely on polarizers that have systematic leak-through of orthogonal polarizations.

In light of these experimental difficulties, Hongfei Wang and coworkers developed a very rigorous chiral SFG technique—the twin-polarization angle method. Simultaneously changing two beams' polarizations (e.g. the SFG and visible beams in Hongfei Wang's study of S- and R-limonene)[55] can reduce concerns about the accuracy

of polarization and bring the chiral signal definitively above signal-to-noise worries. In their experiment, Hongfei Wang and coworkers collected SFG signal at many points through a synchronous 360° rotation of the polarizations of the two beams, producing accurate degrees of chiral excess for CH peaks of S- and R-limonene liquid surfaces. The twin-polarization angle method is analogous to chiral SHG collection methods in that chirality is shown only as an intensity difference rather than as a spectral change. Instead of resolving the chirality as absorbance vs. frequency, the twin-polarization maps $\left|\chi_{eff}^{(2)}\right|^2$ vs. polarization angle. However, the method requires data at many polarizations, which is an inordinate amount of experimental effort. Consequently, no other twin-polarization angle experiments have been published.

Finally, the earliest chiral SFG spectra of surfaces took advantage of the tendency for much stronger achiral SFG signals by collecting interfering the strong achiral and weak chiral polarizations,[41] a method first developed for bulk solutions.[40] Proponents of the interference method collect the positive and negative interference polarizations separately, rotating polarizers and waveplates between data collection.[41,54–57] "Heterodyning" the weaker chiral signal with the stronger achiral signal helped bring chiral SFG above signal-to-noise. The method's results are analogous to those of circular dichroism in that the chirality shows in the difference between the positive and negative polarization combinations. An important benchmark for later parts of this manuscript is the interference chiral SFG of the CH stretch of dry DNA monolayers at the solid-air interface.[56]

The intermediate polarizations of the interference or pmp method can be written

as *s*- and *p*-polarized projections:

$$Polarization(\theta) = \cos\theta \cdot p + \sin\theta \cdot s \tag{40}$$

The trigonometric projections of show that $p + 45°p$ and $p - 45°p$ combinations can measure the psp chiral component by subtracting the two polarizations.

$$I_{p+45°p} \propto \left|\chi_{p+45°p}\right|^2 = \frac{1}{2}\left|\chi^{(2)}_{ppp} + \chi^{(2)}_{psp}\right|^2 \tag{41}$$

$$I_{p-45°p} \propto \left|\chi_{p-45°p}\right|^2 = \frac{1}{2}\left|\chi^{(2)}_{ppp} - \chi^{(2)}_{psp}\right|^2 \tag{42}$$

$$I_{p+45°p} - I_{p-45°p} \propto \left|\chi_{p+45°p}\right|^2 - \left|\chi_{p-45°p}\right|^2 = \frac{1}{2}\left|\chi^{(2)}_{ppp} + \chi^{(2)}_{psp}\right|^2 - \frac{1}{2}\left|\chi^{(2)}_{ppp} - \chi^{(2)}_{psp}\right|^2 \tag{43}$$

$$I_{p+45°p} - I_{p-45°p} \propto 2\chi^{(2)}_{ppp}\chi^{(2)}_{psp} \tag{44}$$

A similar analysis shows that the smp polarization scheme collects information on the spp chiral term and the same could be shown for interference in any of the three beams.

$$I_{s+45°p} - I_{s-45°p} \propto 2\chi^{(2)}_{spp}\chi^{(2)}_{ssp} \tag{45}$$

Difficulties in Previous Chiral SFG

As discussed above, within the C_∞ point group, the choice between chiral polarizations psp, spp, and pps should be a matter of Fresnel coefficients and beam angles. Each polarization combination probes the same $\chi^{(2)}_{zyx}$ element. In the first published chiral SFG at surfaces, however, the psp and spp spectra of tachyplesin I were slightly different, showing an additional peak in the psp spectrum.[41] Our results have also failed to show identical psp and spp spectra. Perhaps tachyplesin I and other chiral samples do not adhere to the geometry of the C_∞ point group.

Another minor chiral SFG controversy has arisen in the chiral spectra of S- and R-limonene. The pair of enantiomers were an early focus of chiral SFG.[40] The interference chiral SFG difference spectra were originally shown to be mirror images—an intuitive result. Work by the group of Hongfei Wang confirmed the general mirror image spectra of the air-liquid interface of S- and R-limonene in the process of demonstrating the twin polarization angle approach.[55] However, later work from the same group of the same interface produced conflicting spectra that were no longer mirror images.[54] Instead, one of the peaks was a mirror image, while another was the same sign in both S- and R-limonene, suggesting that the surface is diastereomeric and not enantiomeric. The difference was explained as arising from a change of beam angles. The first experiment from the Wang group had a visible angle of 63° and an IR angle of 50°. The second experiment had a visible angle of 45° and an IR angle of 55°. However, it is impossible to speculate on the origin of the conflicting spectra without firsthand knowledge of each of the experiments. Whatever the final conclusion of the limonene surface chiral SFG spectra controversy, a more robust experimental method with strong benchmarks is needed.

Early Development in Petersen Lab

First attempts by the author at interference chiral SFG using the $p \pm 45°p$ polarization combination showed spurious signs of chirality in nonresonant (e.g. gold) and achiral (e.g. octadecyltrichlorosilane self-assembled monolayers) samples. As briefly discussed above, inaccurate polarizations or polarization leakthrough can be a major problem for chiral SFG. Using interference chiral SFG can complicate the picture, because the method relies on subtracting the amplitudes of two spectra after changing

polarization by moving optics.

The relative size of the chiral and achiral signal causes leakthrough to more strongly affect the chiral signal. A polarization error of 1° or a leak-through of just 1% can lead to substantial errors. As illustrated by Hongfei Wang and coworkers, if the achiral $\chi^{(2)} = 5$ and the chiral $\chi^{(2)} = 0.5$, then the error in $\left|\chi^{(2)}\right|^2$ will be -58% for a -1° polarization error and +82% for +1° polarization error.[55]

Pointing was also a possible source of error, as optics were rotated in the visible beam before the beam approaches the sample. Slight deviations in pointing could easily change the overlap between infrared and visible beams, causing a change in amplitude that would be mistaken for chirality when subtracting $\pm 45°$ polarizations.

To eliminate erroneous chiral signals in interference chiral SFG, a robust self-referencing method was developed for pure and interference chiral SFG in addition to the method of polarization multiplexing. In the method, two polarizations are simultaneously collected so that alignment, laser power, and other conditions are identical. The simultaneous collections of multiple achiral polarizations (i.e. polarization multiplexing) with a calcite beam displacer was previously reported.[58] In that published work, a beam displacer was used to resolve the four orthogonal achiral SFG polarizations that were created using three incident beams: an infrared beam polarized close to the magic angle (i.e. containing both *s* and *p* polarizations) and two visible beams at *s* and *p*. For an achiral surface, the four beams matched the four nonzero achiral polarization combinations. The work presented here extends polarization multiplexing to chiral SFG without any additional beam or restrictions on the chirality of the surface.

Significantly, the beam displacer (and other additional optics) of the new method are placed after the sample. Thus the achromatic waveplate can be rotated without concerns about tiny pointing changes altering the overlap of the visible and infrared beams at the sample. The polarizer for self-referencing can be inserted and removed and the 2.7 cm-thick beam displacer can be used without affecting the timing, pointing, or dispersion of overlapping beams at the sample. The placement after the sample also leads to easy rearrangement when setting up a SFG experiment that does not require the chiral detection optics. Removing the optics after the sample does not disrupt the beams' spatial and temporal overlap at the sample. Furthermore, the optics (detailed below) are cheap and can be used in both pure and interference chiral SFG experiments. Chiral SFG spectrometers should adopt the optics and methods described here.

Figure *5* summarizes the placement of the optics in the detection arm of the SFG spectrometer. Orthogonal achiral (e.g. *ppp* shown in blue) and chiral (e.g. *spp* shown in red) sum frequency is emitted from a chiral and rotated 45° by an achromatic waveplate (i.e. with a retardation of $\lambda/2$ across a broad region). The rotated beams are then spatially separated by the beam displacer into vertically and horizontally polarized beams that are positive and negative combinations of the achiral and chiral signals. Finally, the two beams are simultaneously detected by CCD (charge-coupled device) camera. For the interference chiral SFG illustrated, simultaneous detection ensures that differences between positively and negatively interfered combinations are indeed chirality and not caused by pointing changes or fluctuating signal strength.

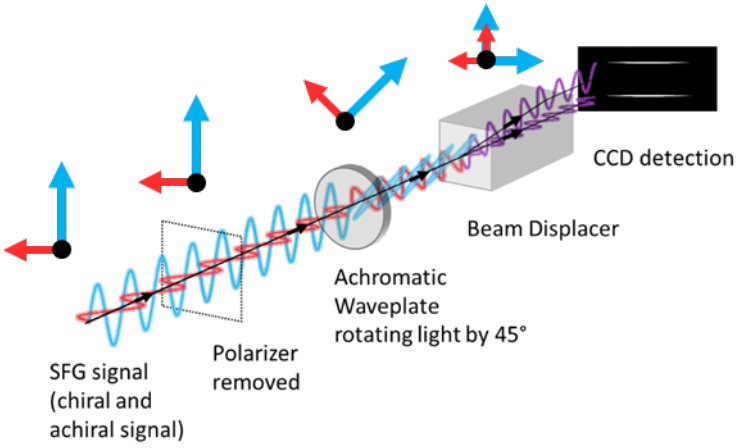

Figure 5. Interference chiral SFG detection optics
Optics arrangement in detection arm of polarization-multiplexed, interference chiral SFG. The waveplate and beam displacer allows the mixing of the stronger achiral signal (blue) and weaker chiral signal (red), so that the ±45° interference chiral SFG mixtures (purple) are simultaneously detected on the CCD array. The polarizer is absent except for self-referencing.

Pure chiral SFG is also easily accomplished as shown in **Figure *6***. The beam displacer offers a unique advantage over the polarizer of a traditional pure chiral SFG spectrometer. While a traditional polarizer would discard the unwanted achiral SFG beam, the beam displacer simultaneously collects the achiral and chiral signals together (e.g. *ppp* with *spp*). The achiral and chiral signals can be compared immediately to determine the success of the experiment and whether the strong achiral signal is leaking into the weak chiral signal.

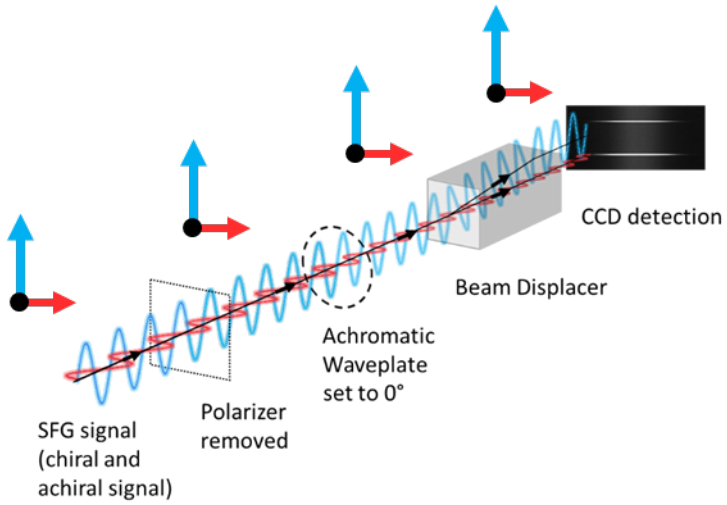

Figure 6. Pure chiral SFG detection optics
Optics in detection arm for simultaneous pure chiral and achiral SFG detection. Rotating the waveplate to 0° (or removal) allows the beam displacer to spatially separate the stronger achiral signal (blue) and weaker chiral signal (red) for detection.

To benchmark the method, a self-referencing technique was developed based on the insertion and removal of a polarizer as illustrated in **Figure *7*** for interference chiral SFG. The polarizer placed after the sample eliminates the chiral polarization. Subsequently, the pure achiral signal is rotated by the waveplate and split into equal parts by the beam displacer. When properly calibrated as described below, detection by the CCD camera shows two halves of a signal, confirming the setup's accuracy for each sample. Another referencing method attempted was to put a spot of gold on the sample and to reference to the nonresonant and achiral gold SFG signal. However, even the movement of the sample to the gold spot introduced uncertainty about the overlap of the beams and the pointing of the reflected SFG beam. In comparison to the gold spot and other methods, the insertion and removal of the polarizer is the least disturbing method for referencing. By placing the polarizer in a reproducible mounting, the

insertion and removal do not affect the achiral SFG significantly, as shown in the data below. Positioning the polarizer to block the smaller chiral signal is preferred to blocking the larger achiral signal, because blocking a small signal reduces the effect of error from leakthrough or polarization error. For the interference chiral SFG, the self-referencing polarizer eliminates differences between the $+45°$ and $-45°$ interference SFG signals. The self-referencing polarizer is a quick confirmation of the experiment for any sample.

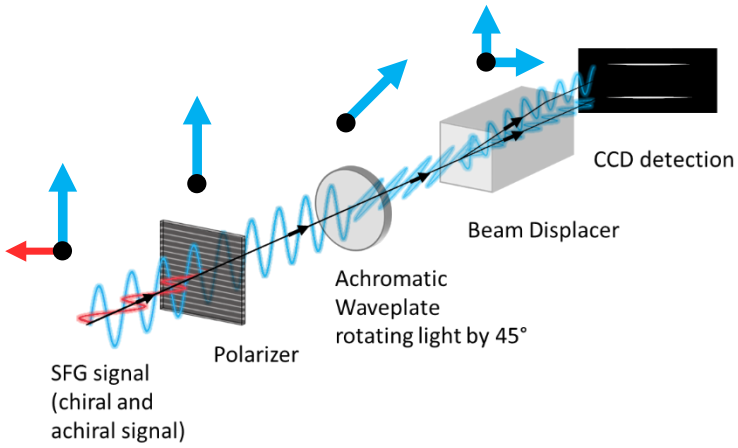

Figure 7. Self-referencing interference chiral SFG detection optics
Optics for self-referencing of interference chiral SFG. The polarizer blocks the chiral signal (red), transmitting only the achiral signal (blue). The waveplate rotates the signal 45°. The beam displacer splits the signal in halves for detection.

Self-referencing of pure chiral SFG detection is also possible as shown in **Figure *8***. With the polarizer inserted and the achromatic waveplate removed or rotated to 0°, only the achiral signal is transmitted. The CCD strip for the chiral signal is empty. The achiral signal should be unaffected by the polarizer, indicating proper alignment.

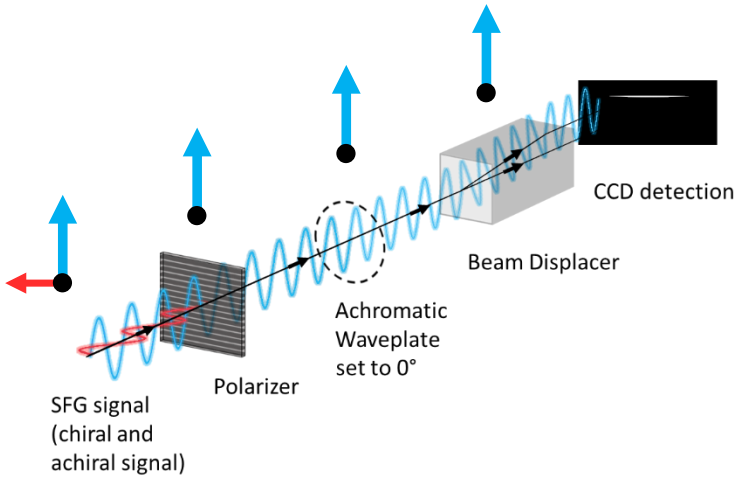

Figure 8. Self-referencing pure chiral SFG detection optics
Optics for self-referencing of pure chiral SFG detection. The inserted polarizer blocks the chiral signal (red), transmitting only the achiral signal (blue). The achromatic waveplate is set to 0° or removed. Only the achiral signal is detected.

Interference chiral SFG spectroscopy is particularly sensitive to misalignment, because spectra are subtracted. For example, the beam displacer must be installed orthogonal to the detector and SFG beam. If the beam displacer is rotated slightly or pointing into the detector is not perfectly orthogonal, then the two stripes can be slightly shifted in space and therefore in frequency. While the frequency shift is very small compared to the resolution of the spectrometer, the shift can cause problematic subtraction errors. Self-referencing is ideal for calibrating the beam displacer and the entire detection arm (waveplate and polarizer) so that there is no frequency shift between the two stripes. A simple way to do this is with the nonresonant $\pm 45°pp$ gold SFG spectrum. With perfect alignment, dividing the $+45°pp$ and $-45°pp$ signals produces a horizontal line vs. frequency with an intensity equal to the grating efficiency factor. Any nonzero slope indicates that one of the stripes is shifted in relation to the

other. The results of such a shift can lead to erroneous signs of chirality in interference chiral SFG. In **Figure *9*** below, the pure (red) and $\pm 45°pp$ interference chiral (green) SFG results for achiral sample OTS show erroneous chirality due to the shift of one region of interest versus the other. The telltale sign of the error is the approximately equal positive and negative areas in the difference interference spectrum. The positive area is caused by a slight shift of the intensity from the frequency of the negative area. Self-referencing and pure chiral SFG also play an integral role in recognizing false signals.

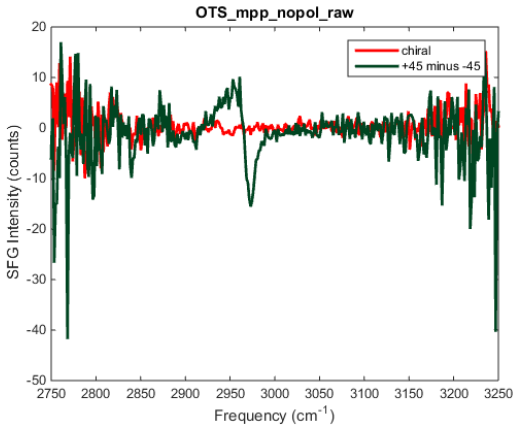

Figure 9. CCD stripe shift error
The pure spp (red) and $+45°pp - -45°pp$ interference chiral (green) SFG results for achiral sample OTS showing erroneous chirality due to the shift of one region of interest versus the other. While the pure spp chiral signal shows the absence of chirality and is unaffected by the frequency shift between the regions of interest, the difference between interference chiral SFG is acutely sensitive to alignment errors.

To counteract this, the detection optics should be adjusted until a zero slope is achieved. Additionally, one of the data sets can be shifted in relation to the other. For the data in this paper, the lower stripe of the CCD was offset by approximately 1.3 pixels

compared to the upper stripe. The shift was customized for each data set to adjust for pointing at different points in time. Using Matlab (Mathworks), the data is interpolated to ten times the pixel resolution using the *griddedInterpolant* function with the *pchip* option. *Circshift* then adjusts the self-referenced data until the grating efficiency factor reaches zero slope.[c] The slope must be maintained when rotating the waveplate and inserting and removing the self-referencing polarizer. The grating reflects light polarized horizontally to the plane of the table approximately 80% as efficiently as vertically polarized light. The exact efficiency difference was found to be incredibly sensitive to sample pointing. For example, translating the stage in the sample plane should not move the sample plane, but slight misalignments caused translation of the stage in the sample plane to slightly change the apparent grating efficiency difference. The best way to measure the exact efficiency difference is with the sample in the exact position using self-referencing as described below.

The accurate setup of the waveplate is also important. The Newport NSR1 rotation mount and NSC200 controller are used through homemade LabVIEW programs for maximal reproducibility. The mount's rotational repeatability is 0.25°. To benchmark the position of the waveplate to the position of the rotation mount, the mount was rotated in 125 microsteps (2°) through multiple revolutions as nonresonant SFG is

[c] The LabVIEW program for data collection also needed to be tweaked. One key setting is the "acquire focus mode" for the subVI "ExSubInitCam.vi". The comment in the our VI reads: "Acquire / focus mode; 3 is asynchronous; Camera will not take an image until ready"
When this mode is set for "3", the ratio of light in the bright strip (e.g. ppp) vs. the dark strip (e.g. spp) is ~30:1, but when this mode is set for "1", then this ratio is ~30:1 for the first frame, then the much higher ratio (~100:1) for the rest. The only way to get the correct number of counts (cf. Winspec) is to set the "dwell time" for the exposure time. This effectively doubles the experimental time, which is unreasonable. Alternatively, one can put any small dwell time (it doesn't seem to matter much) and one will lose just a small number of counts from the nth frame (n>2) and they will show up in the n+1th frame. Generally, the effect of these small overflowing counts is minor.

collected. As the waveplate is rotated, the beam displacer splits the constant SFG intensity into sinusoidally varying horizontal and vertical components. The areas under the SFG spectra are integrated and plotted versus mount position, fitted to sine curves using Origin, and normalized from 0 to 1. Other analyses produce similar results.

The results shown in **Figure *10*** indicate that 4000 microsteps corresponds to the λ/2 waveplate at 22.5° (i.e. 45° rotation of linearly polarized light) and 5460 microsteps corresponds to the λ/2 waveplate at 0°. The local oscillator SFG in the *msp* polarization, however, has slightly different polarizations. The collimating and focusing parabolic mirrors between the LO generation and SFG sample rotate the *s*-polarized LO SFG, resulting in a 5.6° rotation versus other SFG polarizations and sample positions. Generally, the polarization purity of the LO SFG is not an important consideration for experiments.

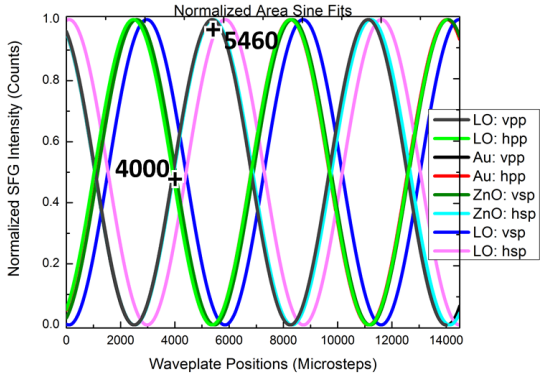

Figure 10. Waveplate rotation calibration
Normalized sine fits of integrated SFG data for achromatic waveplate positioning in Newport NSR1 rotation mount. The rotation of the waveplate causes the constant SFG intensity to be split by the beam displacer into different ratios of vertical and horizontal intensity. For most SFG generated at the sample position in reflection or the LO position in transmission, the λ/2 achromatic

waveplate is set to 0° at 5460 microsteps or 22.5° at 4000 microsteps. The exception is LO SFG in msp polarizations, which is rotated 5.6° relative to the other SFG.

Experimental Methods

For the SFG experiments in this chapter, a 3 mJ beam from a Ti:sapphire amplifier (Coherent, Legend Elite Duo, 793 nm, 1 kHz, 25 fs, 38 nm FWHM) pumps an OPA (OPerA Solo, Coherent) to generate infrared light. For the CH regions, the OPA produces 3400 nm infrared light (250 cm^{-1} FWHM, 30 μJ pulse energy), which is filtered (Germanium, 3000 nm longpass, Spectrogon) and focused at the sample at an incident angle of 40° with a pulse energy at the sample of 5 μJ. The infrared envelope is obtained from nonresonant gold SFG signals in the *ppp* polarization for normalization of SFG signals.

A separate 793 nm beam from the amplifier is filtered by an etalon (a.k.a. Fabry-Pérot interferometer) (TecOptics, 795nm, 0.6 nm, 10 cm^{-1}). Higher and lower order Fabry-Pérot transmission fringes are filtered with a bandpass filter (Thorlabs, FBH800-10, 800 nm, 10 nm FWHM) angle-tuned to maximize throughput. Increasing the angle of incidence away from the filter normal shortens the filter output's center frequency. The narrowband 793 nm pulse is then focused on the sample at an incident angle of 55° with a pulse energy of 5 μJ.

For robust chiral SFG spectroscopy, the reflected SFG signal of a sample is rotated by 45° when the achromatic λ/2 waveplate (air-spaced, Eksma 467-4205) is set to 22.5°. To increase reproducibility, the waveplate is placed in a motorized rotation mount (Newport NewStep NSR1) and controlled via LabVIEW. The use of an

achromatic waveplate is essential because of the breadth of SFG wavelengths in broadband SFG detection. The calculated retardation of the waveplate over the region of interest is 0.493 to 0.507 λ.[d]

The self-referencing polarizer is placed in a post collar (Newport) for reproducible height and rotation. The birefringent calcite beam displacer (Thorlabs BD27) vertically displaces vertically polarized light about 3 mm. The beam displacer is transparent throughout the visible and into the mid-infrared wavelengths. The separated horizontal and vertical projections are directed into a monochromator (Acton SP-2500i, Princeton Instruments, 1800 grooves/mm blazed at 500 mm) and collected on a liquid nitrogen-cooled CCD array (Spec-10, Princeton Instruments, 1340x400 pixels).

The polarization of the SFG signal greatly impacts the reflection efficiency of the grating. To calibrate for the reflection efficiency, the self-referencing polarizer eliminates the chiral signal. The achiral signal can then be rotated and split by the beam displacer. Dividing the spectra of the two beams reveals a scalar grating efficiency

[d]With a visible beam of 793 nm, the SFG wavelengths of interest for these experiments range from approximately 613 to 649 nm (corresponding to infrared frequencies of 2800 to 3700 cm^{-1}). For the Eksma air-spaced achromatic waveplate used (Stock # 467-4205), the calculated retardance over this range is 0.493 to 0.507 λ as shown in the figure modified from the Eksma catalog (http://eksmaoptics.com/optical-components/polarizing-optics/achromatic-air-spaced-waveplates/).

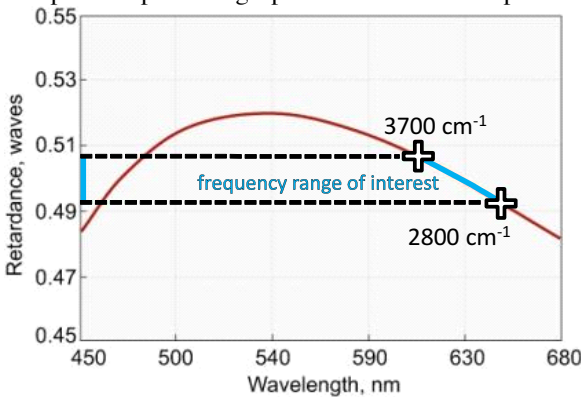

factor. The polarizer is removed and the grating efficiency factor can be used to calibrate interference and pure chiral SFG signals.

To demonstrate robust chiral SFG spectroscopy, four samples were used. Achiral samples were an octadecyltrichlorosilane (OTS) self-assembled monolayer (SAM) and spin-coated poly(methyl methacrylate) (PMMA) film, both of which are common benchmarks in SFG spectroscopy. The OTS (Sigma-Aldrich) was prepared at 2 mM in hexanes and deposited on SiO_2-coated CaF_2 windows. The CaF_2 windows (CeNing Optics) were coated with SiO_2 using atomic layer deposition. The film of PMMA (anisole solution, Microchem 495 PMMA A) was spin-coated (Laurell WS-400A-6NPP-LITE) onto a CaF_2 window (Crystran). The model chiral samples were adsorbed ubiquitin and drop-casted collagen film. Ubiquitin has previously been used as a model protein in SFG spectroscopy[59] and collagen has been a common benchmark for chiral SFG studies.[33,60,61] Ubiquitin from bovine erythrocytes (Sigma U6253) was dissolved in ultrapure water (EMD Millipore Milli-Q Advantage A10 system, 18.2 MΩ·cm @25°C, 5 ppb TOC) and placed in contact with a CaF_2 window overnight, then rinsed with ultrapure water. Collagen from rat tail (Sigma C7661) was dissolved at 1 mg/mL in acetic acid for 3 hours and drop cast onto a CaF_2 window and used immediately. All samples were confirmed by FTIR spectroscopy (Thermo Fisher Nicolet 8700) with a liquid nitrogen-cooled Mercury Cadmium Telluride detector using a homebuilt White cell with 8 transmissions.

Results

Results for the robust, self-referencing chiral SFG spectroscopy method are demonstrated below with the CH stretch region of several benchmark samples. Two

achiral and two chiral model samples are used: OTS and PMMA for the achiral and collagen and ubiquitin for the chiral. $\pm 45^{\circ} sp$, psp, $\pm 45^{\circ} sp$, and spp polarizations are demonstrated. *pps* and $\pm 45^{\circ} ps$ polarizations were not attempted, because the signals arising from the *s* polarization of the IR beam are generally weaker.[58]

The left column of each figure shows results for achiral samples, while the right column shows results for chiral samples. The first figures of each set present pure and interference chiral SFG. Pure chiral SFG is shown in red, while pure achiral SFG is shown in blue. Interfered chiral and achiral SFG are shown in black (-45°) and green ($+45^{\circ}$). For the achiral samples, the pure chiral SFG in red is zero and the positively and negatively interfered chiral SFG in black and green are identical, because of the lack of chirality. For the chiral samples, the pure chiral SFG in red is nonzero and the interfered chiral SFG in black and green are not identical, because of the chirality of the sample.

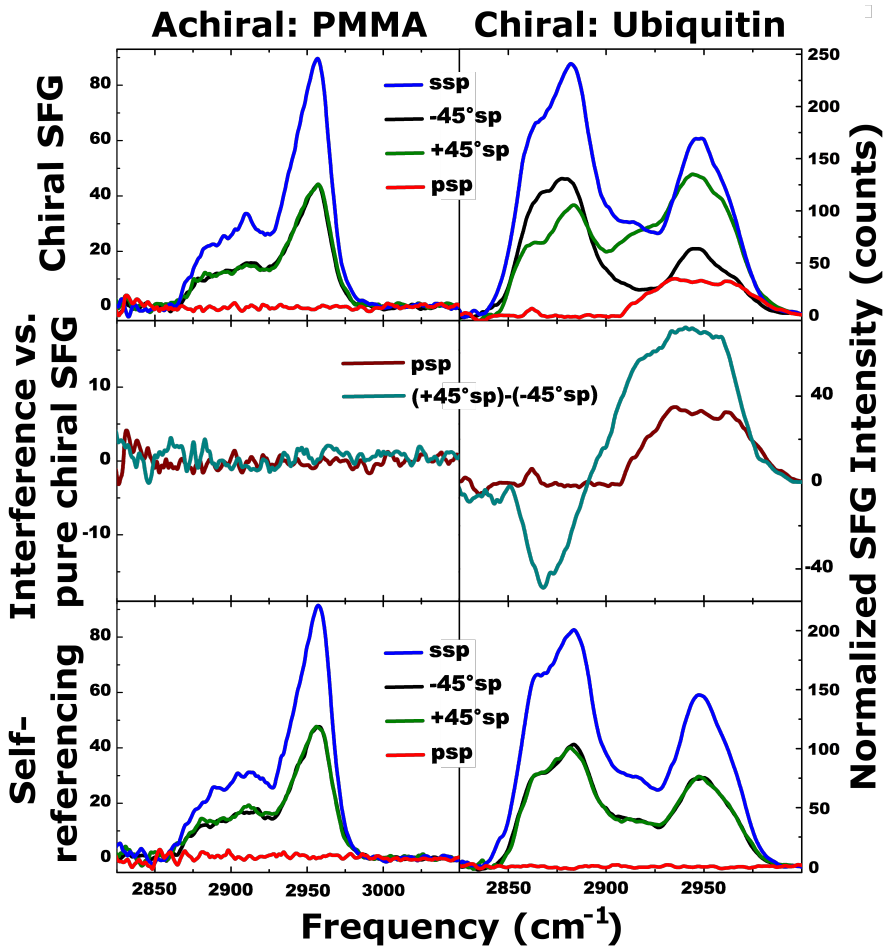

Figure 11. PMMA and ubiquitin *msp* chiral SFG results
θsp chiral SFG of the CH stretch of the achiral, spin-coated PMMA (left column) and the chiral, adsorbed ubiquitin (right column). Top: ±45°pp interference and pure chiral SFG. Middle: Interference and chiral SFG comparison. Bottom: Self-referencing.

The second figures of each set compare chiral results of interference and pure chiral SFG. Pure chiral SFG is shown in red, while the difference between positively and negatively interfered chiral SFG is shown in blue. For both pure and interference chiral SFG, the results clearly demonstrate achirality and chirality of the samples. For the achiral samples, both methods display zero chirality. For the chiral samples, the two methods display nonzero chirality in different ways. The pure chiral SFG results in wine

is proportional to the square magnitude of the chiral tensor element and is therefore positive.

$$I_{chiral} \propto \left|\chi^{(2)}_{chiral}\right|^2 \tag{46}$$

The interference chiral SFG results in turquoise, however, is proportional to the product of the chiral and achiral tensor elements and therefore produces positive and negative peaks.

$$\Delta I_{\pm 45^\circ} \propto 2\chi^{(2)}_{achiral}\chi^{(2)}_{chiral} \tag{47}$$

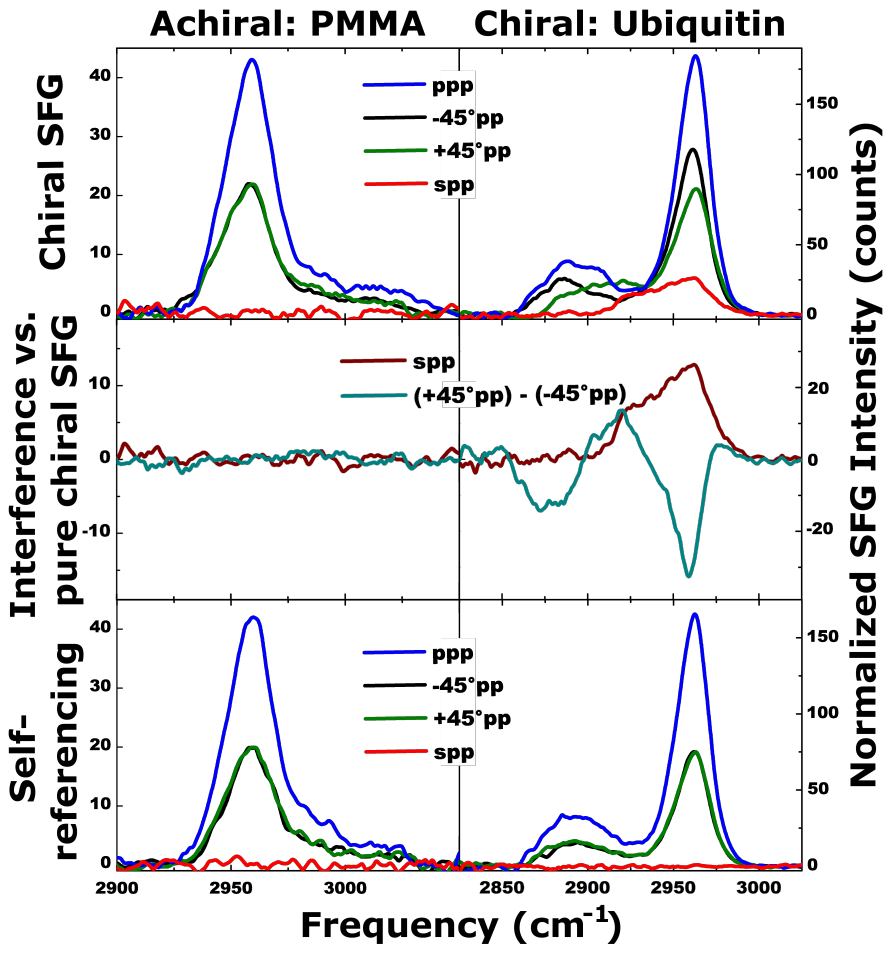

Figure 12. PMMA and ubiquitin *mpp* chiral SFG results
θpp chiral SFG of the CH stretch of the achiral, spin-coated PMMA (left

column) and the chiral, adsorbed ubiquitin (right column). Top: ±45°pp interference and pure chiral SFG. Middle: Interference and chiral SFG comparison. Bottom: Self-referencing.

The third figures of each set display self-referencing results for both pure and interference chiral SFG. Before and after inserting the self-referencing polarizer, the chiral SFG results for an achiral sample are identical. For a chiral sample, however, the self-referencing polarizer confirms that the resolved chirality for pure and interference chiral SFG are genuine. The self-referencing polarizer causes the pure chiral signal in red to vanish, the pure achiral signal in blue to remain the same, and the differences between the positively and negatively interfered chiral SFG in black and green to disappear. The self-referencing provides immediate assurance about the origin of chiral signals.

The top left of **Figure *11*** and **Figure *12*** shows the θpp and θsp chiral SFG results for the achiral, spin-coated PMMA. The ppp PMMA spectrum is dominated by a single methyl stretch at about 2960 cm^{-1}. The ssp PMMA spectrum has peaks at 2900 cm^{-1} and 2960 cm^{-1}, corresponding to methyl stretches. The $\pm 45° pp$ and $\pm 45° sp$ interference spectra are each half of the ppp and ssp spectrum as expected for an achiral sample. The p-polarized SFG and s-polarized SFG are simply split by the beam displacer. The middle left of **Figure *11*** and **Figure *12*** compares the pure and interference θpp and θsp chiral SFG results for the achiral, spin-coated PMMA. The difference and pure chiral spectra show no chirality. The bottom left of **Figure *11*** and **Figure *12*** shows the self-referencing θpp and θsp chiral SFG results for the achiral, spin-coated PMMA. The self-referencing spectra in the bottom left of **Figure *11*** and **Figure *12*** is identical to the corresponding spectra in the top left of **Figure *11*** and

Figure *12* as expected for achiral samples.

The top right of **Figure *11*** and **Figure *12*** show the θpp and θsp chiral SFG results for the chiral, adsorbed ubiquitin. The ppp SFG spectra of ubiquitin contains the methyl stretch at 2960 cm^{-1} as in PMMA. The ssp SFG spectra of ubiquitin appear to contain four peaks: two methyl stretches at 2890 and 2950 cm^{-1} and two methylene stretches at 2860 and 2920 cm^{-1}. An additional peak at about 2890 cm^{-1} corresponds to another methyl stretch. Furthermore, the nonzero resonance between the peaks and the breadth of the lower peak indicate methylene stretches as well. While the $\pm 45° pp$ interference spectra are approximately half the intensity of the ppp spectrum, the differences indicate chirality in both major peaks. The pure chiral spp spectrum is nonzero from 2925-2975 cm^{-1}.

The middle right of **Figure *11*** and **Figure *12*** compares the pure and interference θpp and θsp chiral SFG results for the chiral, adsorbed ubiquitin. The difference spectrum shows three peaks—two negative at 2870 cm^{-1} and 2960 cm^{-1}, and one positive at 2920 cm^{-1}. While the two negative peaks are approximately the location of methyl stretches, the peak at 2920 cm^{-1} is likely a methylene (CH_2) stretch. Although the width of the 2925-2975 cm^{-1} peak in the pure chiral spp spectrum could allow one to speculate that it is two unresolved peaks, the difference interference spectrum clearly resolves the two peaks, because of the phase difference between the peaks. The difference interference spectrum's negative peak at 2870 cm^{-1} does not appear in the pure chiral spp spectrum. This unexpected peak could indicate that the chiral signal here is very small and needs interference with the larger achiral signal to appear above the signal-to-noise threshold.

The pure chiral psp spectrum is quite similar to the pure chiral spp spectrum—nonzero from 2925 to 2975 cm^{-1}. This is a very encouraging result that suggests that psp and spp are probing the same $\chi^{(2)}_{zyx}$ element, as predicted for the C_∞ point group above. There is also a tiny peak in the pure chiral psp spectrum at 2860 cm^{-1}. Although this peak is small, it is slightly above the signal-to-noise threshold apparent in the baseline. The peak could be the same resonance that appears as a negative peak at 2870 cm^{-1} in both the $\pm 45° pp$ and $\pm 45° sp$ difference interference spectra. The $+45° sp - -45° sp$ difference interference spectrum is nonzero across the aliphatic CH stretching region with a negative peak at 2860 cm^{-1} and a broad positive peak from 2900-2975 cm^{-1}. While the $\pm 45° pp$ difference interference spectrum clearly resolved the broad peak in this region into a positive peak at 2920 cm^{-1} and negative peak at 2960 cm^{-1}, here the two peaks must have the same phase in the $\pm 45° sp$ spectra. Similarly to the $\pm 45° pp$ difference spectrum, it is not obvious why the $\pm 45° sp$ difference spectrum is nonzero where the pure chiral psp spectrum is zero. The interference method could be amplifying peaks that are very small in the pure chiral signal.

The bottom right of **Figure *11*** and **Figure *12*** shows the self-referenced θpp and θsp chiral SFG results for the chiral, adsorbed ubiquitin. The self-referencing spectrum removes the chiral signal. The pure chiral spp and psp spectra are empty and the $\pm 45° pp$ and $\pm 45° sp$ interference spectra are approximately half the intensity of the ppp spectrum and identical.

Unfortunately, nonresonance in background scans affected the baseline certainty of these samples. The background had to be manually subtracted as shown in **Figure *13***

below, causing baseline uncertainty.

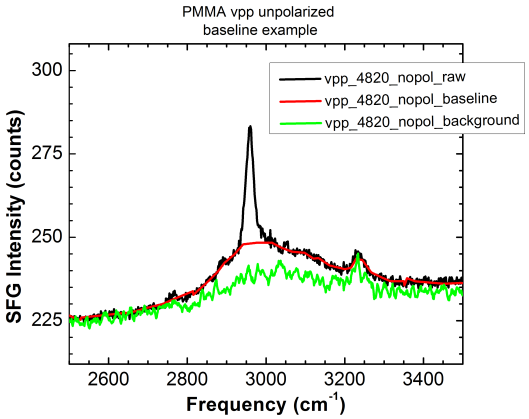

Figure 13. Manual background subtraction *Unknown sources of nonresonance in the baseline for some of the chiral SFG data collection for this section of the dissertation. Here the ppp achiral SFG of the CH stretch of PMMA is shown with the background scan. Although the peak is clear in the sample spectrum (black), the background (green) has apparent nonresonance. Therefore, a manual background (red) is subtracted, leading to some baseline uncertainty for this data.*

The top right of **Figure *14*** and **Figure *15*** show the θpp and θsp chiral SFG results for the achiral OTS SAM. The ppp OTS spectrum has peaks at 2890 cm^{-1} and 2960 cm^{-1}, which are the methyl stretches. The ssp OTS spectrum has methyl stretch peaks at 2880 cm^{-1} and 2950 cm^{-1}. The shoulders at 2850 cm^{-1} and 2920 cm^{-1} correspond to the methylene stretches and indicate that the monolayer is imperfect. Methylene stretches cancel in all-trans configurations. In other words, there are cis bonds in the alkyl tails that allow non-vanishing methylene stretches. The $\pm 45° pp$ and $\pm 45° sp$ interference spectra are each half of the ppp and ssp spectrum as expected for an achiral sample. The p-polarized SFG and s-polarized SFG are simply split by the beam displacer. The middle left of **Figure *14*** and **Figure *15*** compares the pure and

interference θpp and θsp chiral SFG results for the achiral OTS SAM. The difference and pure chiral spectra show no chirality. The bottom left of **Figure *14*** and **Figure *15*** shows the self-referencing θpp and θsp chiral SFG results for the achiral OTS SAM. The self-referencing spectra in the top left of **Figure *14*** and **Figure *15*** is identical to the spectra in the bottom left of **Figure *14*** and **Figure *15*** as expected for achiral samples.

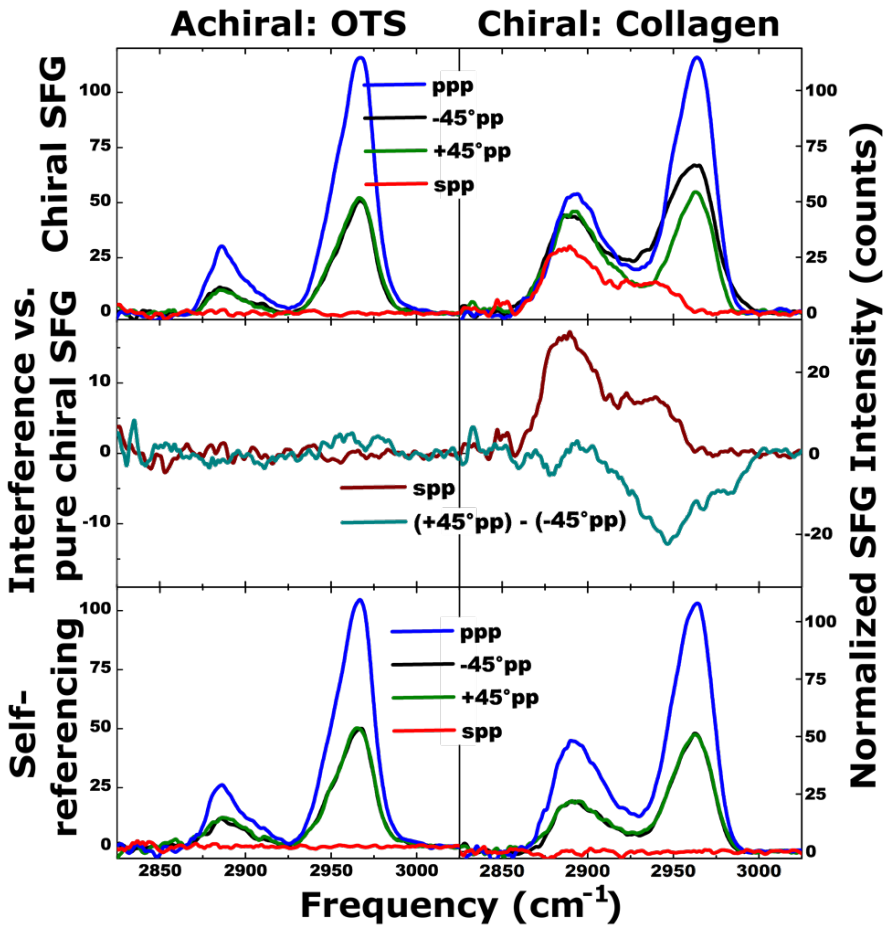

Figure 14. OTS and collagen *mpp* chiral SFG results
θpp chiral SFG of the CH stretch of the OTS SAM (left column) and the chiral, drop-casted collagen (right column). Top: ±45°pp interference and pure chiral SFG. Middle: Interference and chiral SFG comparison. Bottom: Self-referencing.

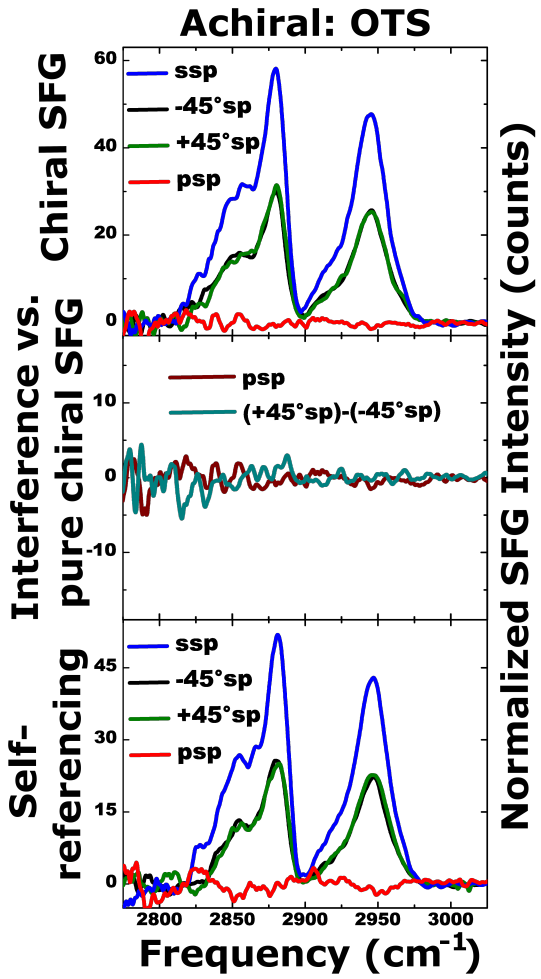

Figure 15. OTS *mpp* chiral SFG results
θsp chiral SFG of the CH stretch of the OTS. Top: ±45°pp interference and pure chiral SFG. Middle: Interference and chiral SFG comparison. Bottom: Self-referencing.

The top right of **Figure *14*** shows the *θpp* chiral SFG results for the chiral, drop-casted collagen. The *ppp* SFG spectra of collagen shows methyl stretch peaks at 2890 cm^{-1} and 2960 cm^{-1}. Additionally, the nonzero resonance between the peaks indicates methylene stretches. While the ±45°*pp* interference spectra are approximately half the intensity of the *ppp* spectrum, the differences indicate chirality. Correspondingly, the pure chiral *spp* spectrum is nonzero from 2860-2960 cm^{-1}.

The middle right of **Figure *14*** compares the pure and interference θpp chiral SFG results for the chiral, drop-casted collagen. The difference spectrum is negative and structured across the region with minima at 2880 cm^{-1}, 2950 cm^{-1}, and 2990 cm^{-1}. The negative peaks across the spectrum indicate that the chiral $\chi^{(2)}_{spp}$ term has the same phase relationship with the $\chi^{(2)}_{ppp}$ term across the spectrum The pure chiral spp spectrum is positive from 2860-2960 cm^{-1} with peaks at 2900 cm^{-1} and 2950 cm^{-1}. The pure chiral spp spectrum has no phase information. Therefore, the fact that it is positive while the difference spectrum is negative is not meaningful. Furthermore, the difference in structure and peak location in the difference spectrum as compared to the pure chiral spectrum is not surprising. The difference spectrum is proportional to the product of the $\chi^{(2)}_{spp}$ and $\chi^{(2)}_{ppp}$ terms, causing a complicated structure that is not necessarily straightforward to interpret as resonant stretches. As with the ubiquitin spectra above, the difference spectrum is nonzero up to 3000 cm^{-1} where the pure chiral spp spectrum is zero. The interference method could be amplifying peaks that are very small in the pure chiral signal.

The bottom right of **Figure *14*** shows the self-referencing θpp chiral SFG results for the chiral, drop-casted collagen. The self-referencing spectrum removes the chiral signal. The pure chiral spp spectrum is empty and the $\pm 45° pp$ interference spectra are approximately half the intensity of the ppp spectrum and identical. Unfortunately, the collagen sample was contaminated before the θsp chiral SFG could be collected.

Like normal heterodyning, the difference between the $+45°$ and $-45°$ interference signals reflects the phase of modes. However, unlike in normal

heterodyning, where the strong reference signal is a slowly varying nonresonant signal with a constant phase, the reference signal in interference chiral SFG is the resonant achiral SFG signal with a variable phase across the spectrum. Consequently, analysis of the interference chiral SFG signal has been challenging. Interference chiral SFG gives more information than pure chiral SFG, because it includes phase information on the chiral signal, but this phase information must be analyzed carefully, because it is in reference to the peaks of the achiral signal.

An example of interpreting the interference chiral SFG in reference to the achiral SFG is the chiral SFG of DNA from the Geiger group.[56] The work takes the difference between the $p + 45°p$ and $p - 45°p$ for the solid-air surface of two monolayers of double-stranded DNA. One strand has the surface-bound silanated all-thymine 15-mer hybridized with an all-adenine 15-mer (T_{15}:A_{15}). The difference spectrum via interference chiral SFG shows two negative peaks—one for the stereocenter on the deoxyribose methane stretch (2900 cm^{-1}) and one for structural helical chirality of the methyl groups of thymine (2960 cm^{-1}). The other strand has a surface-bound 15-mer with three thymines and 12 adenines and the complementary hybridizing strand (T_3A_{12}:$T_{12}A_3$). The difference spectrum via interference chiral SFG for this strand shows a positive peak for the structural helical chirality of the methyl groups of thymine (2960 cm^{-1}). The peak of the deoxyribose methane stretch (2900 cm^{-1}) remains negative. The helical twist of the thymines starts from the 3' end in the first strand and the 5' end in the second strand. In other words, while the absolute chirality should remain the same (i.e. right-handed), the chirality vs. the surface for the majority of the thymine groups flips by changing the sequence and surface-binding direction. The difference spectra in

this case are proportional to chiral second-order susceptibilities from the achiral ppp polarization and from the chiral psp polarization. The ppp term should not change sign between the two sequences, but the psp apparently flips phase by 180°, resulting in a change in sign for the difference spectrum peak.[42] The local chirality of the deoxyribose methane is insensitive to the direction of the surface and remains negative for both sequences. The experiment is an impressive display of the rigor of chiral SFG, but also points out that interpreting the phase of the interference chiral SFG results is nontrivial. In this case, a second sample was required before the phase could be interpreted.

Conclusion

In summary, robust self-referenced, polarization-multiplexed interference and pure chiral SFG was developed and demonstrated. The method is facile, cheap, and an improvement on existing chiral SFG detection schemes. Polarization multiplexing was applied to chiral SFG for the first time, allowing simultaneous collection of orthogonal interference chiral SFG signals or of orthogonal pure achiral and chiral SFG signals. When used for interference chiral SFG, simultaneous detection of positively and negatively interfered chiral and achiral SFG signals eliminates systematic error from alignment and laser fluctuations. When used for pure chiral SFG, simultaneous detection collects all generated sum frequency and eliminates error from leak-through. The beam displacer replaces the SFG polarizer that discards one polarization of generated SFG signal. Self-referencing was introduced as a novel benchmark for chiral samples. The self-referencing polarizer ensures that chiral signals genuine by blocking the weak chiral signal and validating that the achiral signal splits into two equal parts. Relying on the polarizer to block the smaller chiral signal reduces the impact of error

from leakthrough or polarization error. The introduced methods—self-referencing and polarization-multiplexing—are implemented in the detection arm of the SFG spectrometer. By placing the additional optics after the sample, the optics can be inserted, rotated, and altered without changing the overlap or timing of the visible and infrared beams at the sample. For future time-resolved experiments, the thick beam displacer will not cause dispersion or delay of beams at the sample. The new method can be used in both pure and interference chiral SFG experiments and should be implemented in any chiral SFG spectrometer to increase robustness, acquisition speed, and signal-to-noise ratios.

Chapter 3: The Chiral Spine of Hydration of DNA

Introduction

The first few layers of water around DNA are critical to its structure and biological function. Dehydration can change the structure from the classic right-handed B-form to the shorter and wider A-form and the left-handed Z-form. Furthermore, interactions of DNA strands with small molecules and proteins are mediated by the solvation structure. As such, the hydrating waters form an activation barrier for molecular drugs targeting the major and minor grooves of DNA; essential biological processes such as DNA transcription or biomolecular binding involve displacing the solvation shell.[62–65] Consequently, DNA's hydration shell has been studied extensively with X-ray crystallography,[66–70] neutron scattering,[71] NMR spectroscopy,[72–74] electronic[15] and vibrational spectroscopy[75] and molecular dynamics (MD) simulations.[18,76] X-ray experiments performed at cryogenic temperatures have shown structural waters in the minor groove of DNA, giving notion to the presence of a spine of hydration in the DNA minor groove. However, NMR experiments have obtained conflicting results concerning the dynamics of the solvation structure of DNA at ambient conditions ranging from a modest slowdown of a factor of 2-3 compared to bulk water to greatly slowed down waters.[73,74] Similarly, time-resolved fluorescence measurements have suggested evidence of slow water molecules in the hydration shell[15] but the interpretation of these measurements have been questioned.[18] Recent MD simulations have shown a broad range of water dynamics in the DNA solvation structure and identified very slow water molecules in the minor groove of DNA consistent with

the structural waters observed in the X-ray experiments.[76] To differentiate the bulk water response from the response of the relatively few hydration waters, many of the previous experimental methods have relied on cryogenic temperatures, indirect probes, dehydrated DNA, or other methods that likely disrupt the biologically relevant equilibrium hydration structure.[18,77] Second-order nonlinear vibrational spectroscopy, however, is capable of probing interfacial and chiral structures in situ without relying on labels.[42] The fundamental idea of this study is that if structural waters persist at room temperature, they should form an ordered, and chiral, helical structure surrounding DNA. Here we use chiral sum-frequency generation (SFG) spectroscopy to examine the vibrational frequencies of the hydration waters of two DNA sequences bound to a self-assembled monolayer under near-biological conditions (room temperature and 100 mM NaCl solution). We observed that DNA imprints its chirality on the surrounding waters, generating a chiral SFG water response, confirming the existence of a DNA minor groove spine of hydration at room temperature.

Chiral SFG has emerged as a powerful tool for studying chiral biomolecules.[41,42,49,56] SFG is a nonlinear optical method in which an infrared and a visible photon interact with the sample producing a photon with the sum of the incident frequencies (energies). Second-order nonlinear optical techniques like SFG require a lack of inversion symmetry under the electric dipole approximation.[23,57] Chiral-specific SFG spectroscopy is possible because chirality, by definition, breaks inversion symmetry. Where the chiral response in linear vibrational circular dichroism is on the order of 0.1%, the chiral SFG response can be on the same order of magnitude as the achiral SFG response.[33] In linear spectroscopy, the small chiral response is separated

from the large achiral responses by taking a difference between two large signals containing both contributions, e.g. right and left handed polarized light. SFG spectroscopy involves three light fields that can be polarized either parallel (*p*) or perpendicular (*s*) to the plane of incident, giving rise to eight distinct polarization combinations. For a surface that is isotropic with respect to rotations within the plane (C_∞), the polarizations, pure chiral signals can be measured directly by selecting specific polarization combinations of the incident and emitted photons, viz. *spp*, *psp, or pps* (polarizations are listed in descending order of photon frequency, i.e. *spp* indicated *s*-polarized SFG, *p*-polarized visible, and *p*-polarized IR beams).[33,42]

However, as a nonlinear optical method, chiral SFG typically suffers from a relatively poor signal-to-noise ratio making it very difficult to detect a subtle chiral solvation structure. Alternatively, an enhanced chiral signature can be extracted by taking the difference between SFG signals,[40,41,49,54,56] where each of the beams is linearly polarized at +45 and -45 degrees, analogous to circular dichroism. Recent advancements in our laboratory have improved the sensitivity and reliability of chiral SFG, improving the signal-to-noise ratio by more than an order of magnitude, making the present experiments possible.[49]

Experimental Methods

The SFG spectrometer is the same as reported previously.[49] A 3 mJ beam from a Ti:sapphire amplifier (Coherent, Legend Elite Duo, 793 nm, 1 kHz, 25 fs, 38 nm FWHM) pumps an OPA (OPerA Solo, Coherent) to generate mid-infrared laser pulses. To cover the breadth of the OH stretch region, the OPA centered at eight positions (2500, 2600, 2650, 2700, 3100, 3300, 3500, and 3700 nm) with approximately 250 cm^{-}

[1] FWHM and 30 μJ pulse energy, as shown in **Figure *16***.

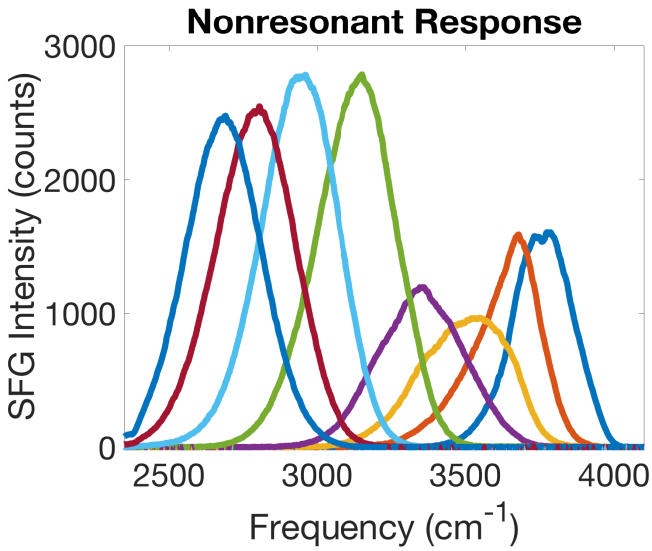

Figure 16. Infrared pulse envelopes
Eight broadband IR pulses used to span the OH stretch region for SFG experiments. IR envelopes are collected using the non-resonant signal of gold spots on sample prisms.

The infrared is filtered (quartz, Spectrogon) and focused at the sample at an incident angle of 65° with a pulse energy at the sample of 5 μJ. A separate 793 nm beam from the amplifier is filtered by an etalon (TecOptics, 795nm, 0.6 nm, 10 cm^{-1}). Higher and lower order Fabry-Pérot transmission fringes are filtered out with a bandpass filter (Thorlabs, 10 nm FWHM) angle-tuned to maximize throughput. The narrowband 793 nm pulse is then focused on the sample at an incident angle of 60° with a pulse energy of 5 μJ. The incident photons induce a second-order polarization that emits a photon at the sum of the frequencies.

To create seamless spectra of the broad OH region, each of the eight frequency spectra are cut off when the intensity is below 5% of the maximum and the intensities are added. The gold spectra are normalized 0 to 1, then the sample spectra are divided

by the normalized gold spectra to produce referenced sample spectra, as shown in **Figure *17***.

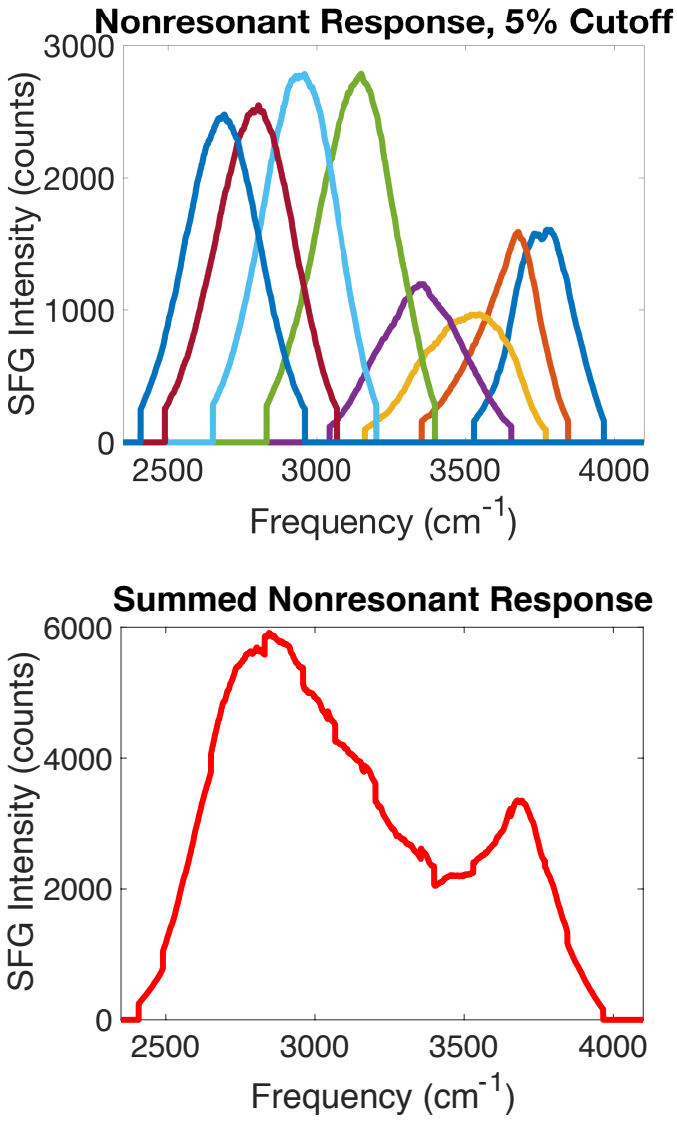

Figure 17. Combined infrared envelope
5% cutoffs of OPA pulse envelopes collected from non-resonant gold spectra (left) and resulting summed and normalized infrared envelope (right).

The dispersion of the SiO_2-coated CaF_2 prisms (discussed below) causes temporal walk-off that must be accommodated. Cross-correlations were taken on the

non-resonant gold signal and the temporal walk-off was adjusted with stage positioning, as shown in **Table *1***.

Table 1. Temporal walk-off
Temporal walk-off at each OPA position caused by dispersion in sample prisms.

OPA λ	t_0
3700 nm	0 fs
3500	20
3300	60
3100	160
2700	280
2650	300
2650	300
2500	440

Figure 18 shows the self-referenced setup and resulting OH stretch spectrum around a 24 base pair double-stranded DNA strand consisting of alternating guanine and cytosine bases. The identical +45°*pp* (wine) and –45°*pp* (olive) signals with the polarizer verify the chiral sensitivity of the experiment once the polarizer is removed.

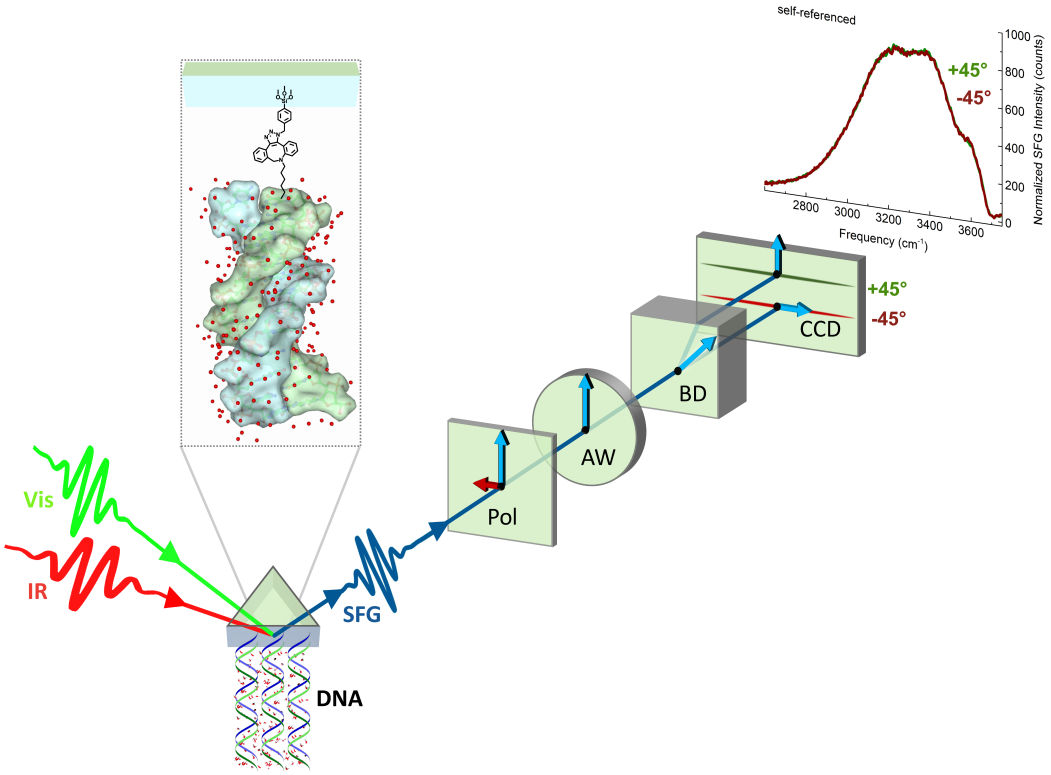

Figure 18. Self-referenced SFG setup.
Incident visible (green) and infrared (red) beams produce a second-order SFG signal (blue) at the buried surface-bound DNA/water interface. The polarizer (Pol) blocks the chiral signal (red arrow). The achromatic waveplate (AW) rotates the achiral signal (blue arrow) by 45°. The beam is then split into vertical and horizontal polarizations by a beam displacer (BD). Finally, the +45° and -45° polarized SFG responses are collected simultaneously by a CCD camera (CCD). The +45° and -45° polarized SFG responses are identical in the self-referencing setup.

When the polarizer is removed, **Figure 19** shows the self-referenced setup and spectrum of the OH stretch around a 24 base pair double-stranded DNA strand consisting of alternating guanine and cytosine bases. The non-identical +45°*pp* (wine) and –45°*pp* (olive) signals without the polarizer reflect the chirality of the OH stretch around the DNA.

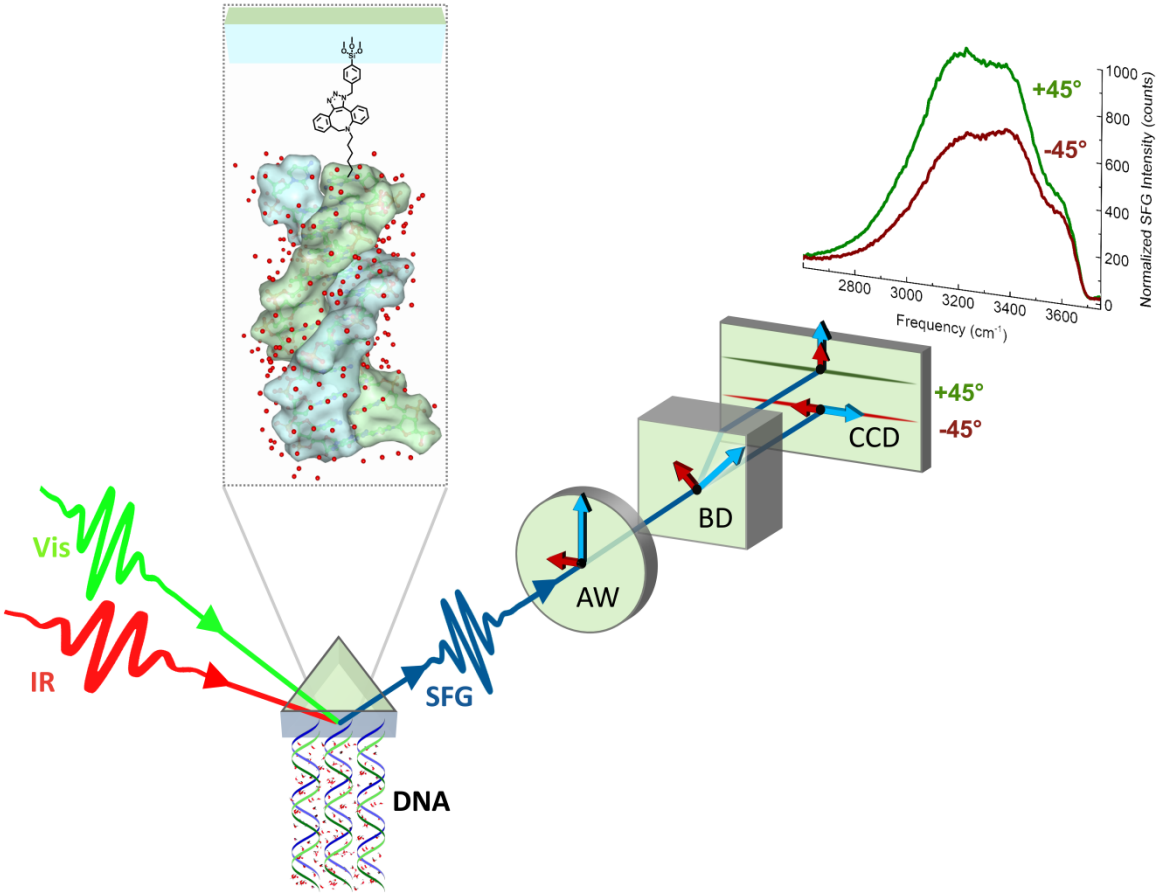

Figure 19. DNA chiral SFG setup.
Incident visible (green) and infrared (red) beams produce a second-order SFG signal (blue) at the buried surface-bound DNA/water interface. The inset shows click chemistry linking the DNA to a SiO_2-coated CaF_2 prism. The SFG beam's polarization is rotated 45° by an achromatic waveplate (AW). The beam is then split into vertical and horizontal polarizations by a beam displacer (BD). Finally, the +45° and -45° polarized SFG responses are collected simultaneously (CCD).

Sample Preparation

Flat windows offer very poor reflection from the buried wet surface for the incident beam angles used here. Therefore, 10 mm x 10 mm 60° equilateral CaF_2 prisms (Crystran) were used for better Fresnel coefficients for the reflected SFG signal. A homemade Teflon flow cell holds the prisms for the SFG experiments. The CaF_2 prisms were coated with a 125 nm thick SiO_2 layer using an atomic layer deposition system

with 110°C plasma (Oxford Instruments ALD FlexAL). The SiO_2 coatings were annealed at 800°C for 30 minutes in a high vacuum furnace (Lindberg). A gold band was added to a section of each sample prism. First, a 5 nm thick titanium adhesion layer was applied, followed by a 150 nm thick gold layer by magnetron argon sputtering through a stainless steel mask. With a skin depth of 16.2 nm for 792.5 nm light and 33.5 nm for 3400 nm light, the titanium adhesion layer does not influence the gold non-resonant SFG response. The non-resonant gold response allows collection of the infrared envelope of the SFG spectrometer.

The SiO_2-coated CaF_2 prisms were then reacted with azidomethyltrimethoxytrichlorosilane (Gelest) using a modified version of a literature gas-phase silanization procedure.[78] Briefly, a 2 L desiccator was dried at 140°C for four hours, then cooled for less than 10 minutes. Silane (200 μL) was added to filter paper. The filter paper and 800 mg of $MgSO_4$ were placed in the desiccator. A homebuilt steel prism holder was placed in the desiccator above the reactants. The desiccator was evacuated for 60 seconds and placed in a 110°C oven for 1 hour. Deposition was verified by FTIR spectroscopy of the azide absorbance at 2100 cm^{-1}, as shown in **Figure *20***.

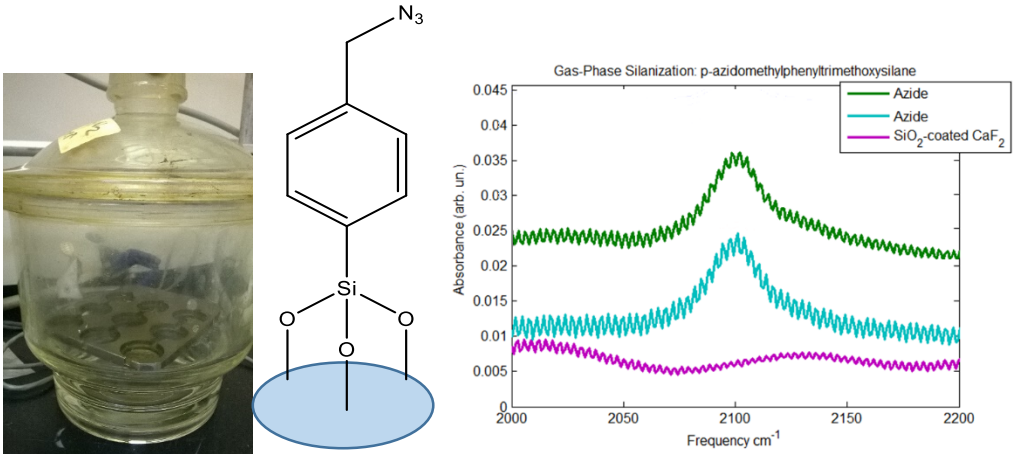

Figure 20. Gas phase azide silanization synopsis.

Photo of gas-phase silanization chamber (left), azidomethylphenyltrimethoxysilane SAM on window (middle), and FTIR (right) of azide-terminated SAM.

DNA was attached to the azide SAM using dibenzocyclooctyl copper-free click chemistry. Dibenzocyclooctyl-modified 24-base pair DNA sequences were purchased from the Keck Oligonucleotide Synthesis Resource at Yale University. The purchased sequences were alternating guanines and cytosines (XCGCGCGCGCGCGCGCGCGCGCG, where X=5'-DBCO-TEG Phosphoramidite) and alternating thymines and adenines (XATATATATATATATATATATATAT) along with the complementary strands. The strained octyne-modified DNA sequences were dissolved to 60 μM concentration in phosphate buffered saline (PBS) and placed in contact with the azide SAM-modified SiO_2-coated CaF_2 prisms for 1 day at room temperature. The DNA-modified prisms were then rinsed with 250 mM NaCl solution to remove any non-bonded DNA. The presence of the DNA was verified by FTIR spectroscopy of the CH-stretches of the DNA and by XPS presence of phosphate, as shown in **Figure *21***. The complementary DNA strands were dissolved in PBS solution and paired with the immobilized DNA by exposure for 1 hour at room temperature. Non-bonded DNA was removed by rinsing with 250 mM NaCl aqueous solution. Azide SAMs and DNA samples were subjected to chiral SFG experiments in contact with 100 mM NaCl aqueous solution.

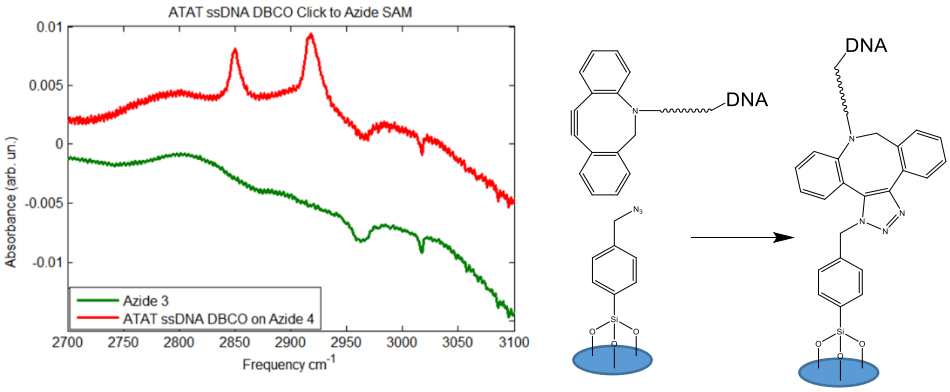

Figure 21. DNA immobilization.
FTIR (left) and chemical structure (right) of DNA-terminated SAM.

Results

Figure 22 and **Error! Reference source not found.** display the SFG spectra for both the GCGC and ATAT double-stranded DNA samples in contact with water. The left columns of each figure show the pure and interference chiral SFG data, while the right columns of each figure show the corresponding self-referenced spectra. In the top row of each figure, the pure achiral *ppp* spectra are shown in blue, the pure chiral *spp* spectra are shown in red, and the *-45°* and *+45°* interference chiral spectra are shown in black and green, respectively.

Of particular interest in the top left plots of each figure are the differences between the *-45°* and *+45°* interference chiral spectra and the non-zero intensities in the pure chiral *spp* spectra. These features indicate chirality in the samples. In the top right plots, these features disappear with the introduction of the self-referencing polarizer. Also of note in the top rows' plots are the constancy of the pure achiral *ppp* spectra. The introduction of the self-referencing polarizer does not disrupt the achiral polarization.

The chiral signals are highlighted in the bottom row. In the bottom left plots of each figure, the pure chiral spectra *spp* are shown in red and the interference chiral

spectra *+45°pp - -45°pp* are shown in gray. The increased signal to noise in the interference chiral SFG technique is apparent. In the bottom right plots of each figure, the self-referencing eliminates the chirality for both the pure and interference methods.

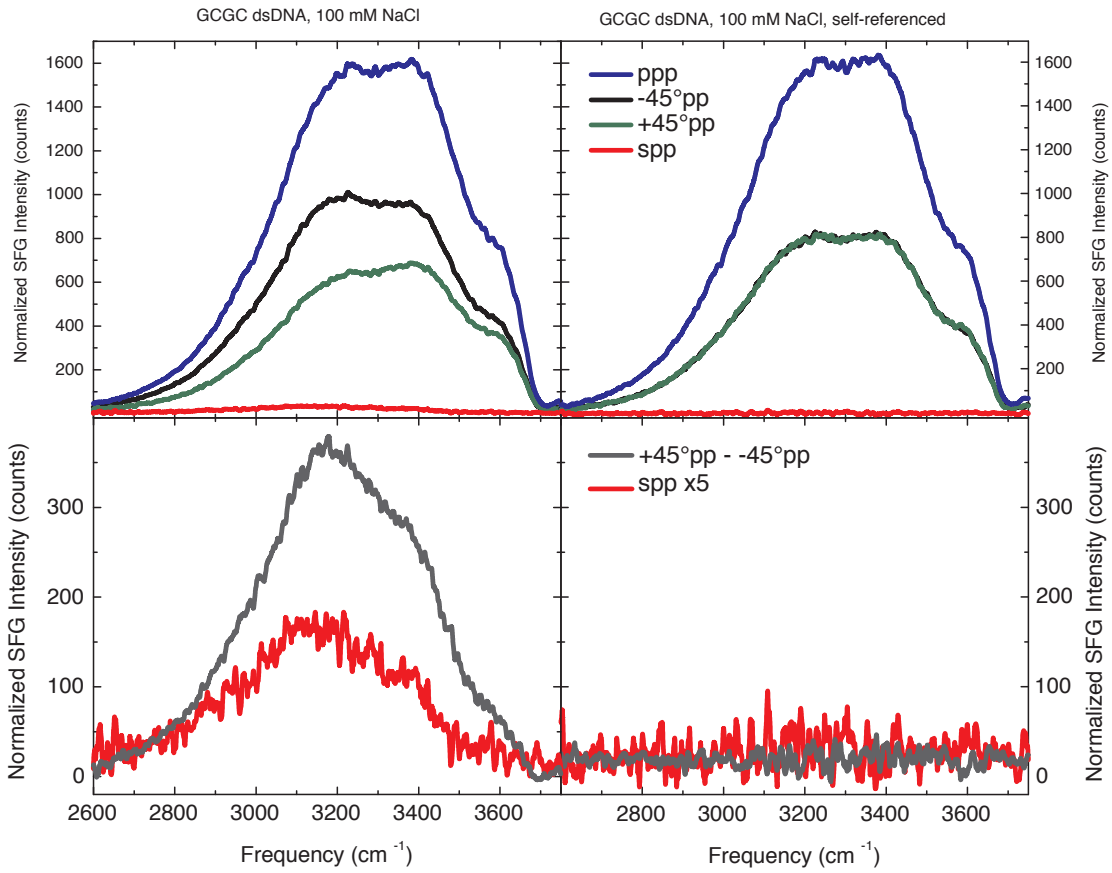

Figure 22. GCGC chiral SFG results.
The chiral SFG results for the immobilized double-strand 24-base pair GCGC DNA sequence in 100 mM NaCl. The left column shows the chiral SFG results and the right column shows the self-referenced results. The chirality of the OH stretch of the sample is clear by comparing the left column to the right column and seeing the non-zero intensities in the pure chiral spectra spp *and the interference chiral spectra* +45°pp - -45°pp.

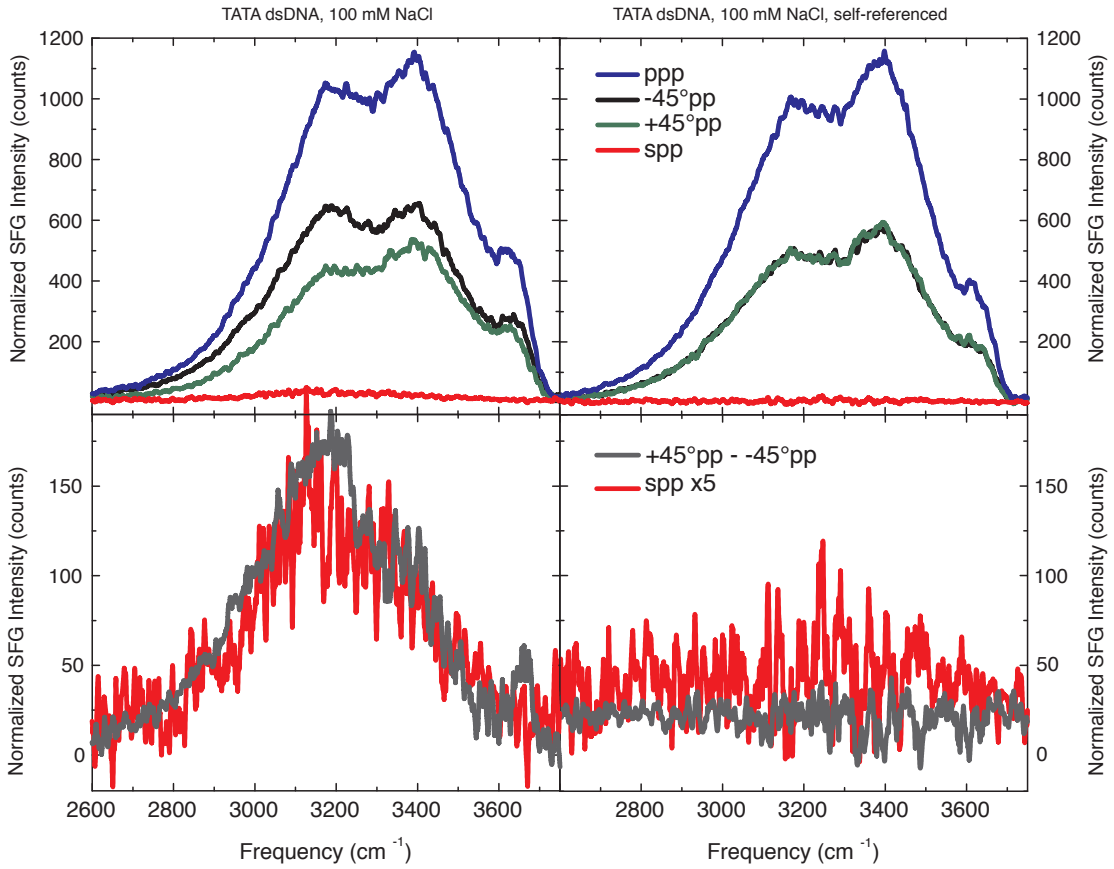

Figure 23. ATAT chiral SFG results.
The chiral SFG results for the immobilized double-strand 24-base pair ATAT DNA sequence in 100 mM NaCl. The left column shows the chiral SFG results and the right column shows the self-referenced results. The chirality of the OH stretch of the sample is clear by comparing the left column to the right column and seeing the non-zero intensities in the pure chiral spectra spp *and the interference chiral spectra* +45°pp - -45°pp.

The results presented here are the first SFG experiments focused on the water OH stretch region surrounding DNA. Previous experiments examined the CH stretch region of surface bound DNA in contact with air using chiral SFG[56] and in contact with water using achiral SFG,[79] showing that SFG is a sensitive probe of the structural chirality of DNA. The water OH stretch vibrational frequency probed here is very sensitive to the local hydrogen-bonded network with lower vibrational frequencies corresponding to stronger hydrogen-bonded configurations.[7] Bulk water OH stretches

spans the frequency range of 3000-3750 cm^{-1}, but water strongly hydrogen-bonded to biological systems can exhibit lower vibrational frequencies. Within the same range, the NH stretch vibrations between DNA base pairs appear as two narrower features at 3200 and 3350 cm^{-1} in bulk measurements[75] but since these are orientated perpendicular to the DNA strain they do not contribute to a net chiral super-structure. The strong differences between the *+45°pp* and *-45°pp* spectra shown in **Figure *22*** and **Figure *23*** across the water OH stretch vibrational frequency region demonstrates that there exists a chiral water structure surrounding the DNA duplex. This chiral water super-structure is templated by the DNA helical structure and is a result of the strong interaction between the DNA and the surrounding solvation shell. **Figure *24*** compares the pure chiral *spp* SFG signal and the difference spectrum taken between the *+45°pp* and *-45°pp* polarized SFG responses shown in **Figure *22*** and **Figure *23*** for the two DNA duplexes with 24 alternating GC or AT base pairs. Both sequences display a chiral water structure showing that the chiral structure is not sequence specific. The chiral signatures measured by the pure and interference methods agree well, where the interference method exhibits improved signal strength.

In addition to establishing the existence of a chiral water structure surrounding DNA at ambient conditions, our results facilitate characterizing the hydrogen-bonding strength of the chirally ordered water super-structure. **Figure *24*** also compares the achiral and difference chiral SFG responses for the GCGC and ATAT duplexes. The achiral *ppp* spectra display a broad spectral OH stretch feature reflecting the broad range of hydrogen-bonding interactions in the solvation shell. The achiral SFG spectrum is consistent with the linear spectrum of DNA in weakly hydrated films.[75] Compared to

the achiral *ppp* spectrum, the difference chiral *mpp* spectra for both the GCGC and ATAT sequences are shifted to lower frequencies while still exhibiting a broad frequency distribution. This shift reveals that the chiral water structure around DNA is more strongly hydrogen-bonded than the general achiral solvation shell as expected due to the strong interaction of localized waters with the DNA base pairs.

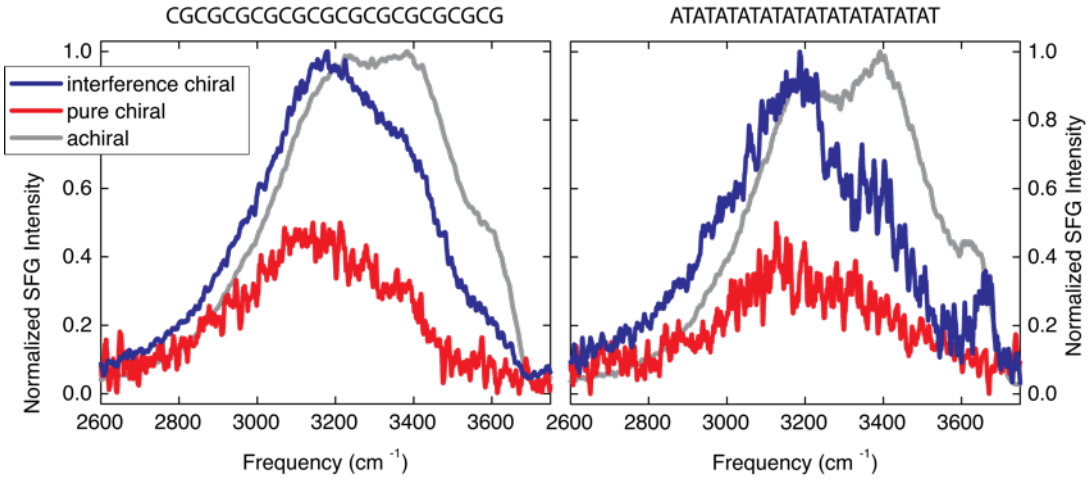

Figure 24. DNA chiral comparison spectra.
Comparison of the interference chiral (+45°pp - -45°pp*), pure chiral (*spp*), and achiral (*ppp*) spectra for the GCGC (left) and ATAT (right) immobilized double-strand 24-base pair DNA sequences in 100 mM NaCl. The interference chiral and achiral spectra are normalized to 1 and the pure chiral spectra are normalized to 0.5 for clarity.*

The chiral water structure around the ATAT sequence further displays a population of non-hydrogen-bonded OH stretch vibrations in contact with a hydrophobic structure at 3660 cm^{-1}. Such non-hydrogen-bonded OH vibrations have previously been observed at the interface between water and hydrophobic surfaces.[80,81] The observation of non-hydrogen-bonded OH vibrations in the solvation shell of DNA is initially surprising. However, it is known that the minor groove at AT base pairs is quite narrow.[82] Accordingly, we attribute the non-hydrogen-bonded OH vibrations to water molecules that donate a single hydrogen-bond to a neighboring water molecule or

DNA base but, due to the narrow width of the minor groove in the ATAT sequence, are not able to find another hydrogen-bonding partner. Our results thus show that the chiral water structure is a general phenomenon but some sequence-specific fine structure exists.

Discussion

Having observed the existence of a chiral water structure surrounding DNA, the question arises as to its origin. While the intrinsic chiral response of stereocenters dominates linear chiroptical signals, structural chirality of achiral molecules arranged in ordered chiral structures dominates chiral SFG.[31–33] Chiral SFG has thus the unique capability of being able to isolate the response of the water molecules that interact strongly with, and thus adapt the overall chiral structure of, DNA. X-ray experiments have shown the existence of structural waters inside the minor groove of DNA around the central AATT region of the Drew-Dickerson dodecamer (CGCGAATTCGCG) at cryogenic temperatures.[66,67] MD simulations of water around the same sequence found that while the dynamics of water in the solvation shell of DNA exhibit a broad range of reorientation times, the structural minor groove water molecules are greatly slowed down at ambient conditions, where those in the rest of the solvation shell are only slowed down to a minor extent as compared to the bulk.[76] The chiral water structure observed here is consistent with the structural minor groove waters but a small contribution from the net alignment of major groove waters cannot be excluded, as depicted in **Figure *25***. This contribution should be small since the water in the major groove should be more disordered due to the larger groove size. Therefore, we conclude that the measured chiral signal is dominated by the waters in intimate contact with the

DNA strands, likely in the minor groove. Our results confirm the existence of structural waters under ambient conditions and that this is a general effect occurring for both GCGC and ATAT sequences.

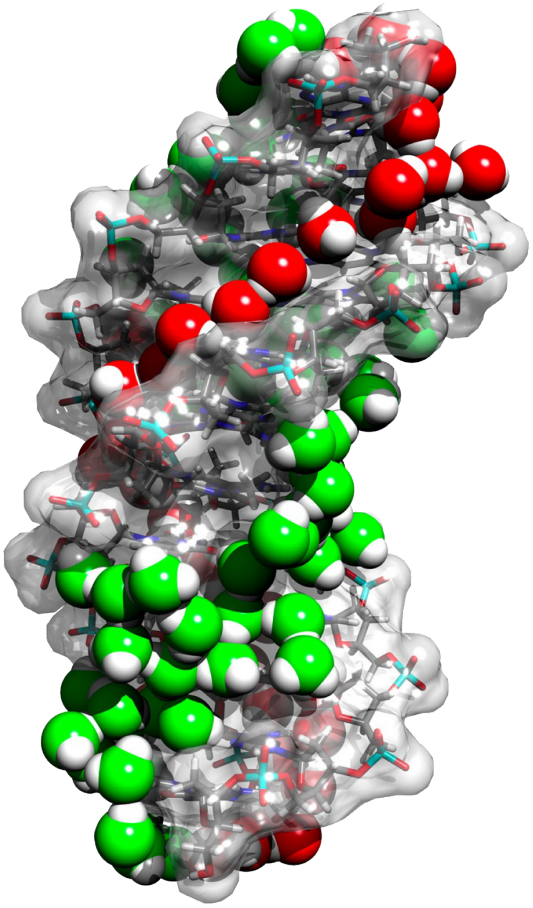

Figure 25. DNA hydration geometry.
The hydration structure in the major (green) and minor (red) grooves for the Drew-Dickerson dodecamer (CGCGAATTCGCG). The narrow minor groove features a strongly bound single hydration layer. The broader major groove has several more loosely bound hydration layers. The observed chiral water structure is consistent with the chirally ordered water structure in the minor groove but a small contribution from the new orientation of water molecules in the major groove cannot be ruled out. Figure courtesy of Steven Corcelli.

The current study is the first direct measurement of the hydration shell of DNA under ambient solvated conditions. The spectroscopic results presented here reveal that the chiral structure of DNA is imprinted on the solvation structure resulting in a chiral spine of hydration surrounding DNA. This chiral water super-structure exhibits a broad range of hydrogen-bonding strengths reflecting the large heterogeneity of the water structure and dynamics in the solvation shell of DNA, but is generally more strongly hydrogen-bonded than the achiral solvation structure. This structure is observed for both ATAT and GCGC sequences showing that the chiral spine of hydration is a general phenomenon not confined to specific sequences. However, sequence-specific differences occur, where non-hydrogen-bonded waters are observed for the ATAT duplex, which exhibits a narrower minor groove compared to GCGC. This is consistent with the idea that a narrower minor groove would confine the water more, and limit the extent to which there are additional solvation shells. This study confirms the existence of structural waters and the spine of hydration surrounding DNA under ambient conditions and further provides a new tool for examining the solvation structure of DNA.

The examination of the chiral nature of the water super-structure provides a means for directly targeting and characterizing the hydrogen-bonding strength of the hydration water molecules and the local environment around DNA more generally. Chiral SFG spectroscopy can now be used to examine how the solvation structure of DNA might transform under different hydration conditions and under interactions with salts, biomolecules, and drugs. For example, since water molecules in the minor groove

of DNA can present a barrier to drug binding, the strongly hydrogen-bonded water can be monitored as the binding event occurs, thereby providing a means of elucidating a mechanism. Given the abundance of chirality in biology, this technique could provide a general method for studying the local water structure in biological settings.

Chapter 4: Conclusion

Water in biology is often perceived as an ordinary, ubiquitous background. Water's role in a wealth of biochemical process, however, presents water as a versatile biomolecule. Therefore, we must characterize not only the structure of biomolecules at interfaces, but also the structure of the surrounding water.

Specifically with DNA, the role of water in DNA's structure, flexibility, and function is often ignored. Without water, DNA loses its characteristic right-handed double-helical B-form and cannot perform functions that are necessary for life. Tools for studying the water around DNA are greatly needed.

As a label-free, surface-specific, chiral-sensitive, nonlinear vibrational spectroscopy, chiral SFG is an ideal tool for studying chiral biomolecules and the water around them. By controlling the frequency of incident and emitted beams in SFG experiments, we can study both biomolecules and their surrounding water. By controlling the polarization of incident and emitted beams, we can selectively study chiral structures.

As a second-order nonlinear technique, chiral SFG is uniquely powerful. Whereas the chiral response in circular dichroism is about 0.1% of the achiral response, the chiral SFG response can be the same order of magnitude as the achiral SFG signal. (Our lab has seen chiral signals nearly one third as intense as their achiral counterparts). However, dilute or weak chromophores are still limited by the attainable signal-to-noise of the weak nonlinear signals.

The chiral water around DNA is not only a weak chromophore, but also dilute.

Therefore, we developed a more robust chiral SFG method to increase signal-to-noise and dependability of chiral SFG results. Next, we applied the new method to the water around DNA and showed that chiral water structure exists and is more heterogeneous than previously reported.

Summary of Dissertation

Chapter 1 addressed the biological importance of studying interfacial water using vibrational spectroscopy.

Chapter 2 discussed the development of a robust, self-referencing method of chiral sum frequency generation spectroscopy. Vibrational SFG was described mathematically to illustrate the origin its interfacial sensitivity. The chiral SFG was also explained mathematically to demonstrate the selectivity of chiral SFG polarizations. We demonstrated the method on solid–air surfaces with achiral and chiral molecules: PMMA, OTS, ubiquitin, and collagen, respectively. We applied polarization multiplexing to chiral SFG for the first time, facilitating simultaneous collection of orthogonal interference chiral SFG signals or of pure achiral and chiral SFG signals. For interference chiral SFG, simultaneous detection of positively and negatively interfered chiral and achiral SFG signals eliminated systematic error from alignment and laser fluctuations. For pure chiral SFG, replacing the SFG polarizer with the beam displacer allowed all generated sum frequency to be collected and eliminated error from leak-through. We employed self-referencing to calibrate alignment for each sample individually using a polarizer in the detection arm. Self-referencing ensured that chiral signals were purely chiral by blocking the weak chiral signal and validating that the achiral signal splits into two equal parts. Our self-referencing, polarization-multiplexed

chiral SFG increased signal-to-noise, reduced the detection time, and provided robustness to both interference and pure chiral SFG results. The method is inexpensive, facile to implement, and beneficial for all existing chiral SFG detection schemes

Chapter 3 described the application of the newly developed chiral SFG method to water around DNA. The interference method of chiral SFG isolated the chiral OH stretch response of water around two 24-base pair sequences of DNA: alternating thymines and adenines and alternating guanines and cytosines. The chiral response was nonzero across the OH stretch region, indicating that water arranged chirally around DNA has a breadth of hydrogen bonding strengths. The presence of strongly hydrogen-bonded waters at 3000 cm^{-1} supports the presence of strong DNA-water H-bonds in the minor groove spine of hydration. Peaks at 3400 cm^{-1} and at 3660 cm^{-1} furthermore show a chiral subpopulation of more weakly and non-hydrogen-bonded water molecules. The heterogeneous waters in the minor groove are likely the origin of the chiral SFG signal. However, alternative interpretations were discussed. The heterogeneity of hydrogen bond strengths represented in the chiral SFG spectra of water around DNA could help explain the many ways DNA can interact with other biomolecules. Sequence-specific hydration differences were also discussed.

The appendices presented below discuss several ongoing studies of interfacial water and other topics. Appendix A describes the synthesis of a metal carbonyl SAM as a vibrational SFG probe of hydration. While direct study of water is possible, the weakness of the OH stretch response can disrupt more complex studies such as transient SFG or 2D-SFG. The vibrational response of metal carbonyls, on the other hand, is very strong and sensitive to the hydration environment. The development of the metal

carbonyl probe is still underway. Preliminary results and future applications are described.

Appendix B chronicles the development of 2DIR lipid membrane samples in collaboration with the Freed group. Methods developed in the Freed group and Petersen group allow creation of model lipid membrane samples with tunable hydration, temperature, and composition. Control over these variables will allow systematic 2DIR study of the role of water in lipid phases and transmembrane protein function. Sample preparation method development is discussed to combat scattering in 2DIR experiments.

Appendix C outlines work on 2DIR investigations of aqueous proton transfer. While the general description of aqueous proton transfer via the Grotthuss mechanism is widely agreed upon, open questions remain. In particular, detailed experimental studies have not yet determined the equilibrium structure of the excess proton in water. Aqueous proton transfer is essential in biology, chemistry, and engineering. Preparation of robust samples is documented and preliminary results are briefly mentioned.

Future Outlook

Access to the water directly at the DNA surface opens up new directions for the study of DNA-ligand interactions. One interesting possibility would be the observation of the water around DNA with and without a minor groove binder like Hoechst stains. Minor groove ligands need to displace water to insert themselves in the groove. Observation of the minor groove waters before, during, and after binding could shed light on specific mechanisms. As mentioned above, DNA can take the

biologically relevant double helix B-form or the looser coiled A-form. However, there is also a left-handed Z-form double helix in the presence of some ions and hydration conditions. Chiral SFG study of the water around DNA as it transitions from B-form to Z-form will provide further insight into the role of chirality and DNA in biology.

Another avenue would be sequence-specific binding. Many sequence-specific DNA ligands interact with the major groove. Although the major groove waters are less tightly bound than minor groove waters, the results above indicate that the major groove waters are also chiral. Comparison of the major and minor groove waters' interactions with major and minor groove ligands could give more insight into the mechanisms of life at the cellular level.

Appendix A: Metal Carbonyl Probes of Interfacial Water

with Marta Sulima (Cornell Chemistry B.S. '14)

Interfacial water plays an important, but poorly understood, role in biological systems. Understanding how water mediates reactions at cell membranes or around proteins is essential for future progress in medicine and biology. Studying interfacial water is also crucial for atmospheric and oceanic chemistry, where water at the surface of particulates and aerosols impacts global climate through mechanisms such as ice nucleation for cloud formation. With ever more pressing concerns about global climate change, studies of interfacial water are urgently needed for better climate modeling.

As discussed throughout this work, vibrational sum frequency generation spectroscopy (SFG) is a second-order nonlinear phenomenon that can produce surface-specific vibrational spectra. SFG spectra of interfacial water can reveal molecular orientation, vibrational coupling, and hydrogen bond network. The fourth-order counterparts of SFG, such as transient SFG or 2D-SFG, are not only surface-specific, but can also reveal valuable information on surface dynamics. Second-order experiments on water are common, but fourth-order experiments are limited by the relatively weak infrared and Raman response of water.

Therefore, we are developing metal carbonyls as probes of interfacial water. The vibrational response of metal carbonyls is not only very strong and sensitive to the hydration environment, but also in an uncluttered region for background free spectroscopy. Recently, the Kubarych group has carried out third-order nonlinear experiments (e.g. 2DIR) using a chromium tricarbonyl probe to study water at biological

surfaces.[83,84] Although 2DIR is a bulk technique, the probe was placed at surface sites in a membrane and on a protein in order to probe surface dynamics. The crucial scientific insight of this technique is the dependence of the symmetric and asymmetric carbonyl stretch frequencies on the polarity of the surrounding solvent.

Following this work, we are developing a metal tricarbonyl probe for surface-specific spectroscopy. Benzoic acid chromium tricarbonyl has a strong carbonyl chromophore and a carboxylic acid for anchoring to a titanium dioxide surface. To prepare the benzoic acid chromium tricarbonyl compound, 240 mg ethyl benzoate chromium tricarbonyl (Sigma) was stirred in an aqueous basic solution in the dark for 16 h as shown in **Figure *26***. Ether extraction and acid wash to quench the base resulted in the desired metal carbonyl carboxylic acid. ATR-FTIR spectra of the dry starting reagent and final product are shown as shown in **Figure *27***. Only the starting reagent's UV-Vis is shown.

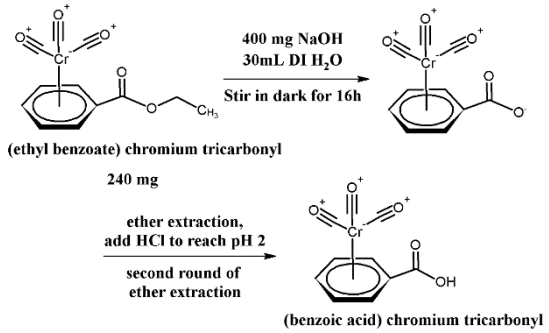

Figure 26. Synthesis of benzoic acid chromium tricarbonyl

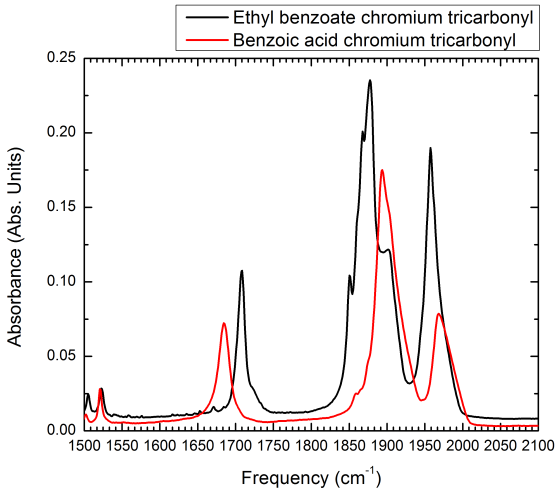

Figure 27. ATR-FTIR spectra of metal carbonyl compounds

ATR-FTIR of ethyl benzoate chromium tricarbonyl and benzoic acid chromium tricarbonyl. The three main peaks in the FTIR, in ascending frequency, are the carboxylic acid / ester peak, the metal carbonyl degenerate asymmetric modes and the metal carbonyl symmetric mode.

As in the literature basis for this work, the final product is insoluble in many solvents. Therefore, a 1 mm path length liquid FTIR cell with ZnSe windows was used to collect FTIR spectra of the starting reagent, ethyl benzoate chromium tricarbonyl as shown in **Figure *28***. The frequency dependence of the metal carbonyl stretches on the polarity of the solvent should be similar for both the starting reagent and final product.

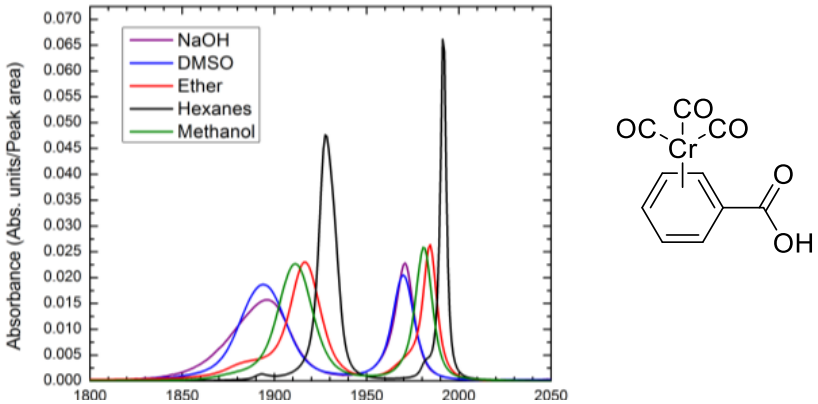

Figure 28. Solvatochromatic shift of metal carbonyl vibration

Solvatochromatic shift of symmetric and asymmetric carbonyl stretches in FTIR spectra of ethyl benzoate chromium tricarbonyl. The vibrational frequencies of the carbonyl stretches report on the polarity of the local environment. The two peaks in the FTIR, in ascending frequency, are the metal carbonyl degenerate asymmetric modes and the metal carbonyl symmetric mode.

The metal tricarbonyl carboxylic acid was then sensitized onto single crystal TiO_2. As with all work here, glassware was placed in Nochromix (Godax Laboratories) solution for 30 min, then rinsed with ultrapure water (Millipore Milli-Q, 18.2 MΩ·cm, ≤5 ppb total organic carbon) until neutral pH was achieved. Two side polished, single crystal rutile (001) TiO_2 substrates (MTI Corporation) were cleaned according to a modified literature procedure.[85,86] The substrates were sonicated in piranha solution (3:1 H_2SO_4/30% aq. H_2O_2) for 1 h, then rinsed with ultrapure water until reaching neutral pH. *Warning: Piranha solution reacts violently with organic compounds and should be handled with extreme caution*. Cleaned substrates were soaked in 1 M NaOH for 5 min, followed by ultrapure water rinse, then soaked in 1 M HCl for 5 min. The soaking substrates were covered with a PELCO quartz substrate disk (Ted Pella, Inc.) and exposed to UV radiation for 10 min using a UVO cleaner (Jelight Company Inc., model 42). The substrates were rinsed with ethanol and immediately immersed in saturated ethanolic solution of benzoic acid chromium tricarbonyl. Surface functionalization of the catalyst occurred overnight in a dark environment. The sensitized crystals were then rinsed thoroughly with ethanol to remove physisorbed catalyst.

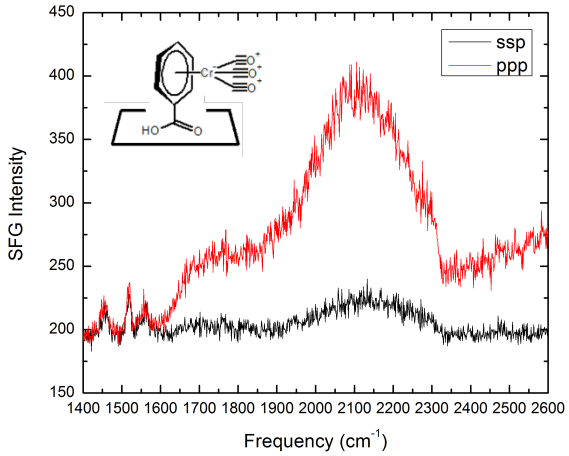

Figure 29. SFG spectra of benzoic acid chromium tricarbonyl on titanium dioxide *SFG spectra of benzoic acid chromium tricarbonyl sensitized to single crystalline rutile <001> TiO_2 in* ssp *and* ppp *polarizations. The only response is the non-resonant response of the TiO_2, indicating that the sensitization was not successful or the dipoles were completely in the plane of the sample and rotationally isotropic.*

SFG spectroscopy of the benzoic acid chromium tricarbonyl-sensitized <001> rutile TiO_2 was accomplished with 4850 nm broadband infrared light and 30 s exposure time, but only resulted in nonresonant signal as shown in **Figure *29***. The sensitization procedure may have failed (and has since been changed) or the carbonyl dipole may be in-plane with the TiO_2 and rotationally isotropic, resulting in no SFG signal.

Therefore, another strategy was developed to covalently link the metal tricarbonyl to a self-assembled monolayer (SAM). Recent 2DIR experiments were accomplished on a rhenium tricarbonyl complex attached to a SAM using copper-catalyzed azide-alkyne cycloaddition (click chemistry).[87] Here we adapt the strategy for the chromium tricarbonyl complex. A chlorobenzene chromium tricarbonyl complex was formed by refluxing chromium hexacarbonyl and chlorobenzene for 20 h in di-*n*-

butyl ether with catalytic THF as shown in **Figure *30***. The chlorobenzene chromium tricarbonyl was then coupled with an alkyne trimethyl silane using a palladium-copper catalysis.[88] The trimethyl silane was then reduced to a terminal hydrogen. NMR spectra and photos of the intermediate products and final product are shown in **Figure *31***. Proton shifts above 5 ppm are aromatic protons and shifts below that are the alkane (0.25 ppm) or alkyne (2.9 ppm) protons. UV-Vis and ATR-FTIR spectra of the final product alkyne are also shown in **Figure *32***.

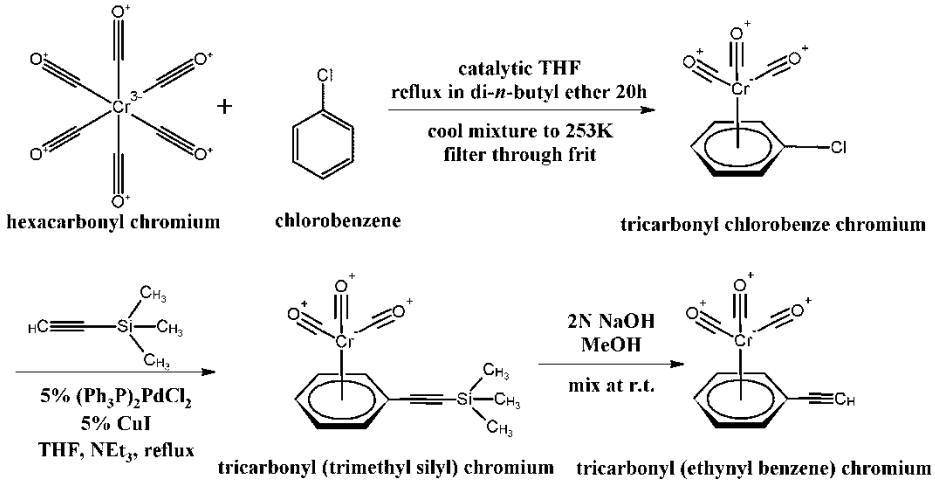

Figure 30. Synthesis of ethynyl benzene chromium tricarbonyl

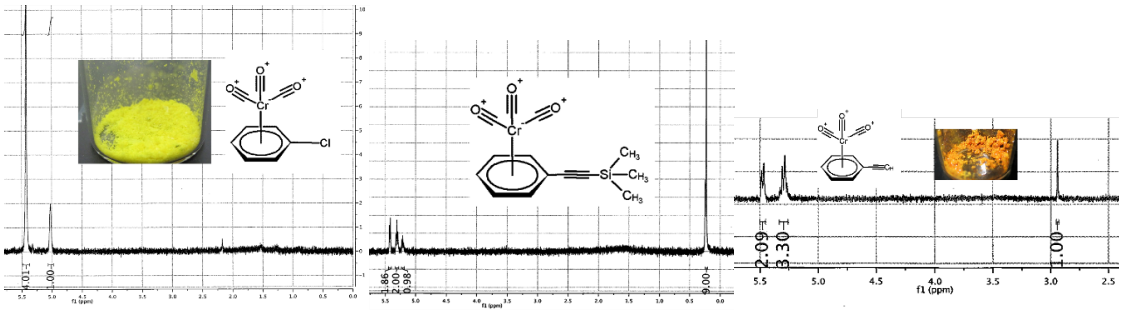

Figure 31. NMR spectra of intermediate and final metal carbonyl compounds
Chlorobenzene chromium tricarbonyl (left), trimethylsilyl ethynyl chromium tricarbonyl (center), and ethynyl benzene chromium tricarbonyl (right). Proton shifts above 5 ppm are aromatic protons and shifts below that are the alkane (0.25 ppm) or alkyne (2.9 ppm) protons. NMR spectra support the success of the reaction.

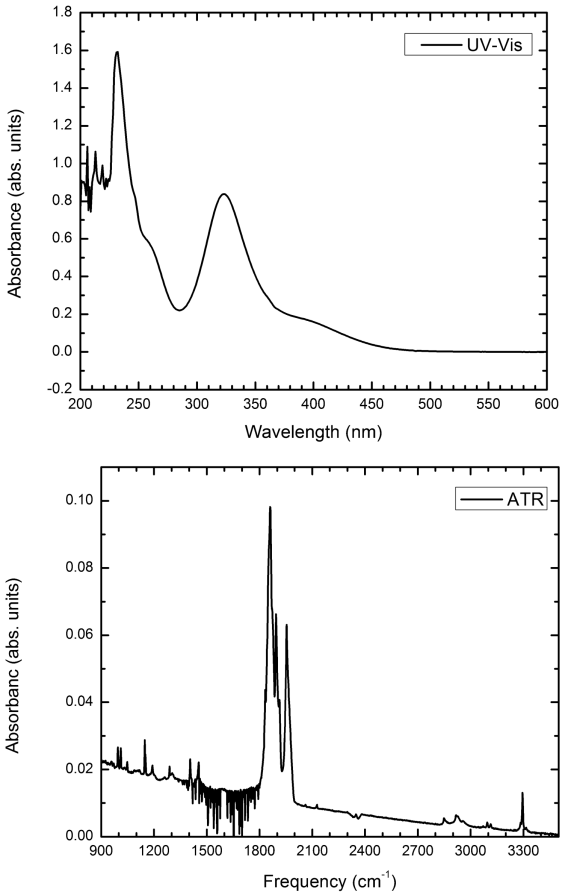

Figure 32. UV-Vis and ATR-FTIR of chromium tricarbonyl compound
UV-Vis (top) and ATR-FTIR (bottom) of ethynyl benzene chromium tricarbonyl. The two peaks in the FTIR, in ascending frequency, are the metal carbonyl degenerate asymmetric modes and the metal carbonyl symmetric mode.

An azide-terminated SAM was synthesized following literature methods as shown in **Figure *33***.[89] However, the chromium tricarbonyl click reaction appeared to be unsuccessful when examined by FTIR and SFG as shown in **Figure *34***.

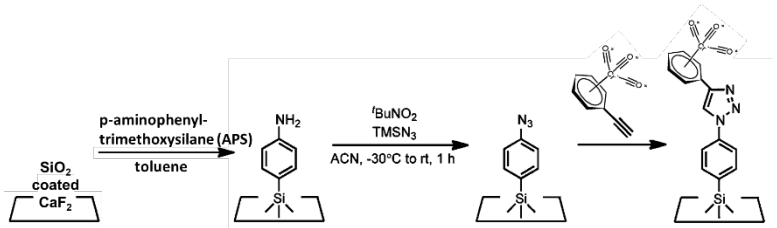

Figure 33. Synthesis of azide SAM and click chemistry
Synthesis of azide-terminated SAM and click chemistry with ethynyl benzene chromium tricarbonyl.

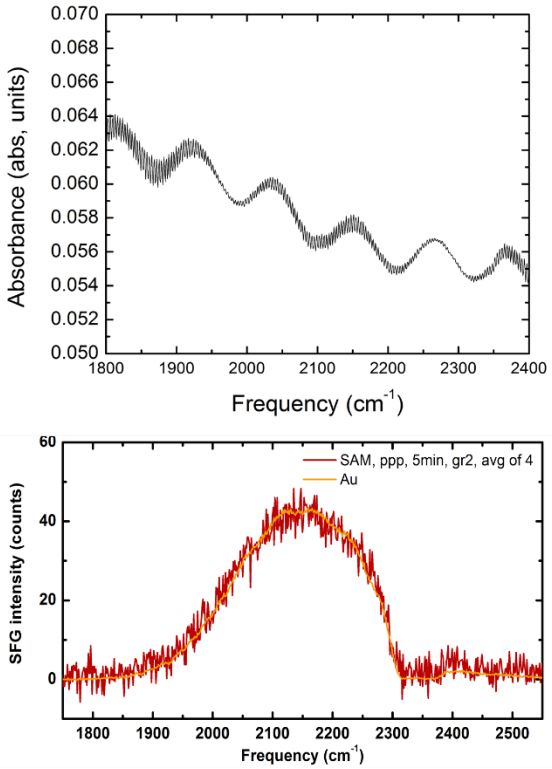

Figure 34. FTIR and SFG of chromium tricarbonyl click SAM
FTIR (top) and SFG (bottom) ethynyl benzene chromium tricarbonyl clicked to azide-terminated SAM. The FTIR and SFG only show the non-resonant signal of the window. The synthesis was not successful.

Another synthesis route was attempted using the azidomethylphenyl-trimethoxysilane (Gelest) used in the DNA work above and following different literature procedures.[90] However, FTIR showed that the tricarbonyl did not attach to the surface. The probable reason for the synthesis failure is the low solubility of the ethynyl

benzoate tricarbonyl chromium in aqueous solutions necessary for the catalysts and Cu(I) of the click procedures used. Ethynyl benzoate tricarbonyl chromium is nearly insoluble in most common reaction solvents. One exception is the relatively good solubility in acetone. However, one additional concern is the small amount (milligrams) left of the alkynyl chromium complex. Therefore, the synthesis needs to be carried out carefully. The suggested future work is to react the small amount of chromium alkyne complex in acetone sandwiched between the azide-terminated SAM on a SiO_2-coated CaF_2 window and a copper window, following the squish procedure found in literature.[91]

Appendix B: Ultrafast Infrared Spectroscopy of Hydration of Lipid Membranes

with Siddarth Chandrasekaran and Boris Dzikovski (Freed Group)

Aligned Model Membranes with Tunable Hydration, Temperature, and Composition

Water in biology is often perceived as an ordinary, ubiquitous background. However, the confined nature of the cell causes properties of water at biological interfaces to differ significantly from those of bulk water, as suggested by theoretical investigations and indirect experiments. But few quantitative measures of the water structure and dynamics in biological systems have been performed. Here we aim to examine the structure and dynamics of the water layer in stacked hydrated lipid membranes using static and time-resolved IR spectroscopy including 2DIR.

2DIR spectroscopy probes vibrational couplings and ultrafast spectral diffusion dynamics on the femtosecond and picosecond time scales. Previous studies have primarily focused on studying the OH vibrations of both neat water and other aqueous systems.[92] In such experiments the 2DIR response averages all the OH vibrations within the entire sample, making it very difficult to unambiguously describe specific hydration structures within the sample. Here we take advantage of methods available at Cornell to manufacture aligned model membranes with tunable hydration, temperature, and composition.[93,94] Control over the sample allows focused study of lipid hydration.

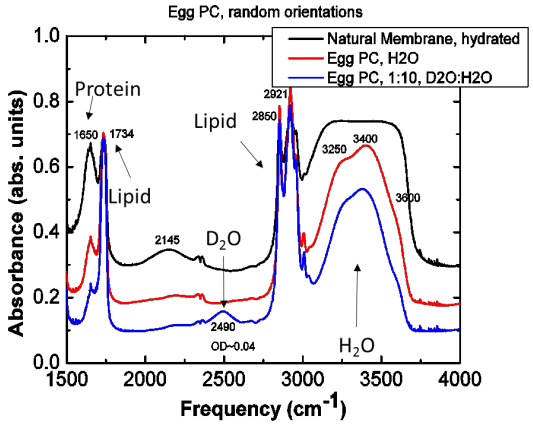

Figure 35. FTIR spectra of egg phosphocholine

FTIR spectra of egg phospho-choline samples at different hydration levels showing vibrational stretches for proteins, lipids, D_2O and H_2O.

Aligned lipid hydration levels are possible through Isopotential Spin-dry Ultracentrifugation (IDSU) adapted by the Freed Group at Cornell (the National Biomedical Research Center for AdvanCed ESR Technology (ACERT)). Aqueous lipid solutions are placed in custom-built ISDU cells that fit inside the buckets of the ultracentrifuge rotor (Beckman SW-27). The centrifugal force is applied normal to the lipid membrane sample surface, aligning the membranes as they dry. The ultracentrifugation takes place under vacuum, removing water over hours or days. By tuning the length of the ultracentrifugation, the model lipid membranes can be dried to exact hydration levels from full hydration (40 water molecules per lipid headgroup) to essentially dry (<2 water molecules per lipid headgroup). Previous 2DIR experiments have been accomplished on artificial membranes consisting of dilauroyl phosphatidylcholine (DLPC) and followed with atomistic simulations.[95–98] However, the sample preparation method in that experiment does not allow tuning of sample

composition as in the work here.

Table 2. Synopsis of DPPC ISDU samples
Weight and thickness of DPPC ISDU samples in H_2O and D_2O alongside a picture of a 4 mg DPPC ISDU-prepared model lipid membrane sample (disk on right) with a razor blade for scale.

DPPC	H_2O	D_2O
2 mg	76 μm	--
4	140	101 μm
10	216	216

Hydration levels of the lipid membranes can be determined approximately by FTIR or more quantitatively by thermogravimetric analysis (TGA). Three ISDU samples of dipalmitoyl phosphocholine (DPPC) at 40 h spin-drying were studied by TGA as shown in **Figure *36***. The mean hydration of the three samples was 1.45 water molecules per DPPC, which is extremely dry.

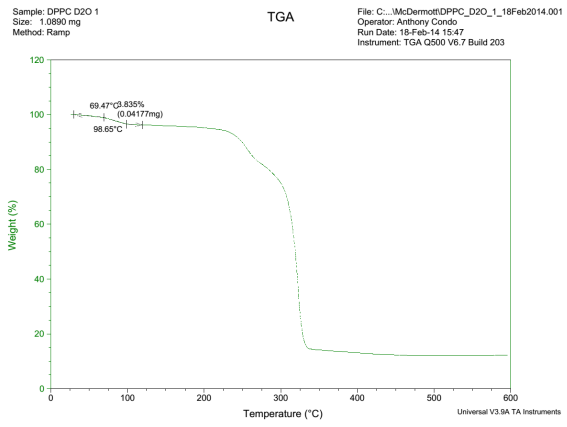

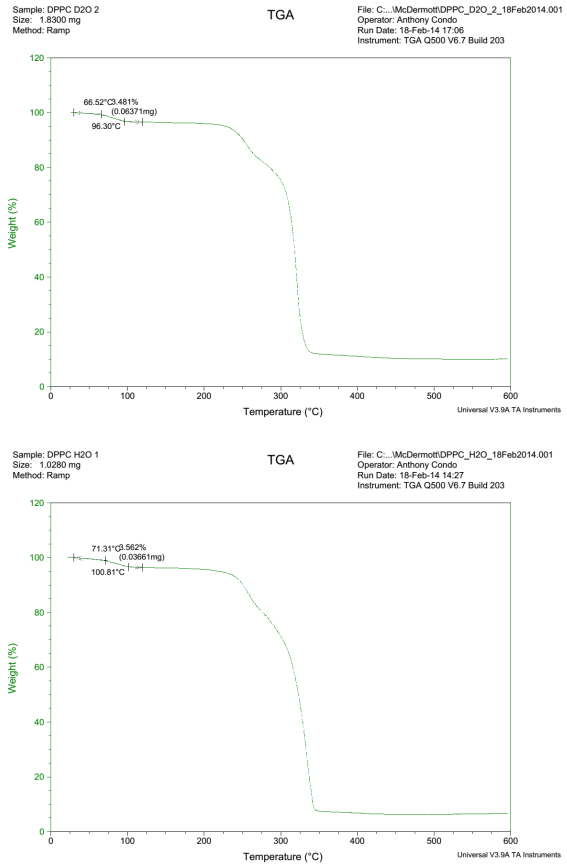

Figure 36. TGA results for DPPC ISDU samples

Top: 4 mg DPPC in D_2O, with 3.835% (41.77 µg of 1.0890 mg) mass lost from 69.47-98.65°C and 22:78 H:D isotope ratio (using Beer's law on the FTIR spectra below) for a water molar mass of 19.56 g/mol and DPPC molar mass of 734.04 g/mol, giving 1.497 water molecules per DPPC molecule. Middle: 10 mg DPPC in D_2O, with 3.481% (63.71 µg of 1.8300 mg) mass lost from 66.52-96.30°C for a total of 1.353 water molecules per DPPC. Bottom: 10 mg DPPC in H_2O, with 3.562% (36.61 µg of 1.0280 mg) mass lost from 71.31-100.81°C for a total of 1.505 water molecules per DPPC.

Composition of the aligned lipid membranes can be tuned by adding different lipids and membrane proteins to the aqueous lipid solutions. Homogeneity and

formation of giant unilamellar vesicles is accomplished through sonication at elevated temperatures (40°C). Compositional variables that have been tested are isotopic dilution of the water with D_2O, addition of transmembrane proteins such as Gramicidin D, ionic solutions such as Ca^{2+} ions for the Gramicidin ion channel, and a variety of phospholipids and phospholipid mixtures.

Isotopic dilution with D_2O allows examination of isolated OH or OD vibrational modes. The study of the isotopically dilute OD stretch of HOD in H_2O is uncoupled from the OH bond on the same molecule and provides a simplified spectrum that is less difficult to interpret.

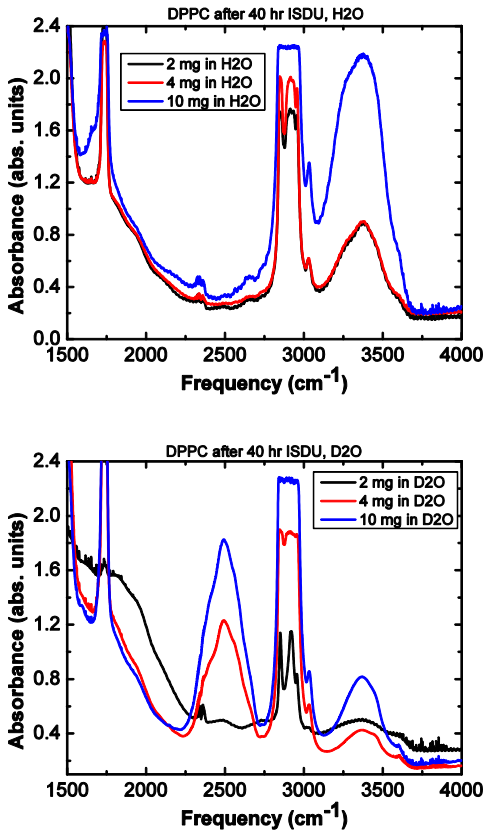

Figure 37. FTIR spectra of DPPC ISDU lipid samples
FTIR spectra of DPPC ISDU lipid samples prepared with different weights in H_2O (top)

or D_2O (bottom). Samples were ultracentrifuged for 40 h. Not all OH stretch protons can be replaced with the deuterium from the D_2O.

Experiments on water-ordering transmembrane proteins provide information on active and passive transport through lipid membranes. Aquaporins are transmembrane proteins that form pores that allow water to diffuse rapidly through the phospholipid bilayer. Aquaporins are also known as water channels and were one of the bases of the 2003 Nobel Prize in Chemistry. Gramicidin D is a mixture of antibiotic transmembrane proteins that allow monovalent cations to pass through bacterial cell membranes, thus disrupting bacterial ion gradients. Divalent cations like Ca^{2+} can block the Gramicidin pore. The Gramicidin channel is lined with a single file of six water molecules, which travel along with the ions. Therefore, the introduction of different transmembrane channels and ions can provide further insight on the role of water molecules in transmembrane transport.

Phospholipid composition of model lipid membranes can drastically change the physical properties of the layer. For example, DPPC consists of two sixteen carbon fully hydrogenated acyl chains. With a melting point of 41°C, DPPC is fully in the liquid phase at room temperature. Lengthening the acyl chains will increase the melting point, while dehydrogenating the acyl chains will decrease the melting point. Therefore, the phase of the model membrane can be controlled by altering either the membrane composition or temperature. Temperature control in a homemade copper cell can induce lipid phase transitions *in situ*.

2DIR experiments are very sensitive to scattering of the incident IR laser pulses

by the sample. 2DIR experiments on ISDU lipid bilayers were disrupted by scattering. Therefore, several actions were taken to reduce to the scattering. The samples were prepared on several substrates to avoid any handling of the sample that could be causing dust or other disruption of the smooth surface. First, 1 mm thick, 13 mm diameter CaF_2 windows (Crystran) were placed on Teflon tape on custom machines aluminum plates for the ISDU cells. Three of the first four CaF_2 window cracked during ISDU. The aluminum plates may have been slightly too wide for the centrifuge tubes and became stuck. The centrifuge tubes were heated to remove stuck samples. Therefore another run was attempted. While the CaF_2 windows did not crack, they did stick to the Teflon tape, requiring significant handling of the sample to free the membrane. Therefore, a second substrate tested was 300 μm thick, 12.5 mm diameter fused silica microscope coverslips. While the samples were successful, the baseline scattering or absorbance in FTIR suggested the samples would still be problematic for 2DIR experiments.

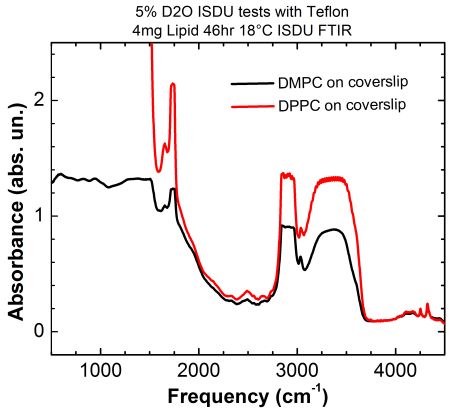

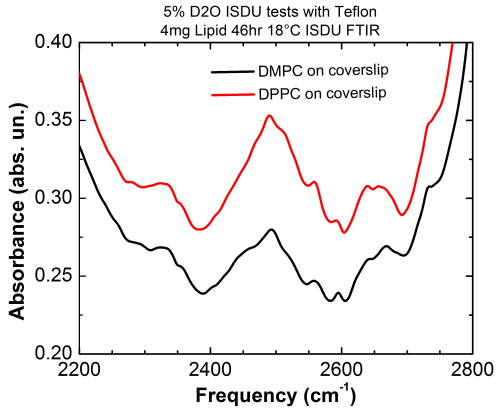

Figure 38. FTIR spectra of lipid samples prepared on fused silica microscope coverslips

FTIR spectra of 4 mg DMPC (dimyristoyl phosphocholine) and DPPC ISDU samples prepared on fused silica microscope coverslips. Full spectrum (top) and OD stretch (bottom). The samples were prepared via ISDU for 46 h at 18°C to avoid the DMPC transition at 25°C. The fused silica coverslip appears to create a very high absorbance baseline (~0.2 abs. un.).

Thirdly, samples were prepared on circles hand cut from 0.040" thick Teflon film (McMaster). ISDU samples prepared in this way appeared smooth. Although Teflon shows a problematic absorbance near the OD stretch, the ISDU lipid samples came easily away from the Teflon circle, resulting in freestanding lipid samples. Although the Teflon preparation technique was successful in producing optically smooth, freestanding samples, the baseline was still high (~0.1 abs. un.) and 2DIR experiments were unsuccessful, indicating that scattering may still have been a problem.

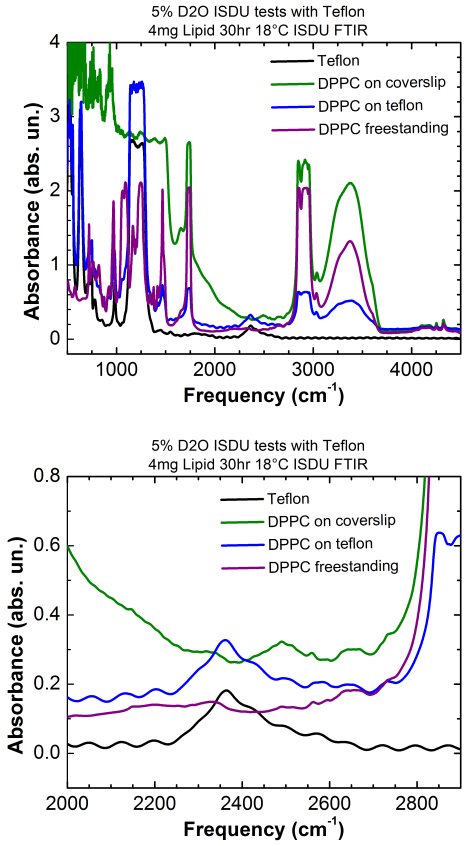

Figure 39. FTIR spectra of lipid samples prepared on Teflon films
Comparison of 4 mg DPPC ISDU lipid samples prepared with microscope coverslips and Teflon films and freestanding lipid samples removed from Teflon films. The full spectrum (top) and OD stretch (bottom) are shown. While the baseline of the freestanding film is lower than that with the Teflon or coverslip, the baseline is still relatively significant (~0.1 abs. un.).

Examination of the ISDU lipid samples by polarized light microscopy revealed that another source of scattering may be roughness or contamination of the samples. The procedures and equipment used in the Freed lab are not designed for optical cleanliness that may be necessary for 2DIR experiments, especially when the current setup has problems with scattering in liquid samples. Future work must attempt more rigorously

clean preparation of ISDU samples to determine whether sample contamination is the source of scattering issues. Issues with roughness may require careful handling of the Teflon film or thicker Teflon films to prevent creasing and other damage to the lipid sample surface.

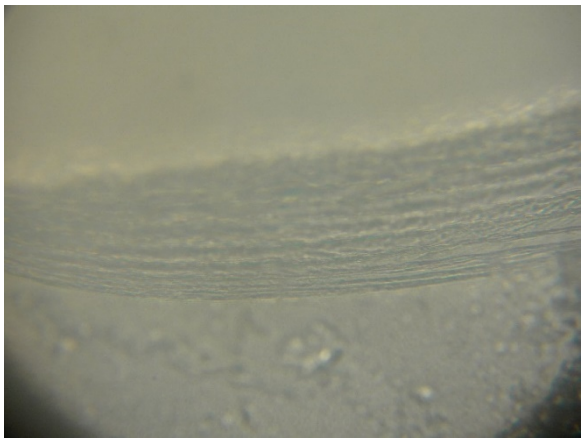

Figure 40. Polarized light microscopy of ISDU lipid layers

Polarized light microscopy (40x magnification) of a 10mg DPPC sample prepared in 5% D_2O and subjected to 24 h ISDU at 25°C. Tearing the ISDU samples reveals the dense layering of the aligned lipid membranes (~5 µm per line).

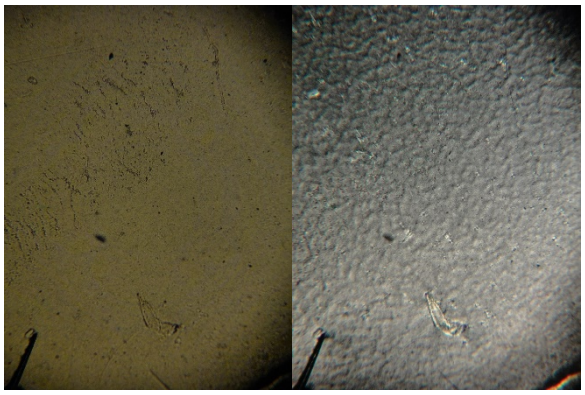

Figure 41. Polarized light microscopy of ISDU lipid teflon film prepared surface roughness

Polarized light microscopy (10x magnification) of a 10mg DPPC sample prepared in 5% D_2O and subjected to 24 h

ISDU at 25°C. The bright field image (left) and the crossed polarizers image (right) are compared. The heterogeneous birefringence shown in the crossed polarizers image suggests that the sample is more rough and variable than apparent in the bright field image. For scale, the black line in the bottom left is ~20 µm wide.

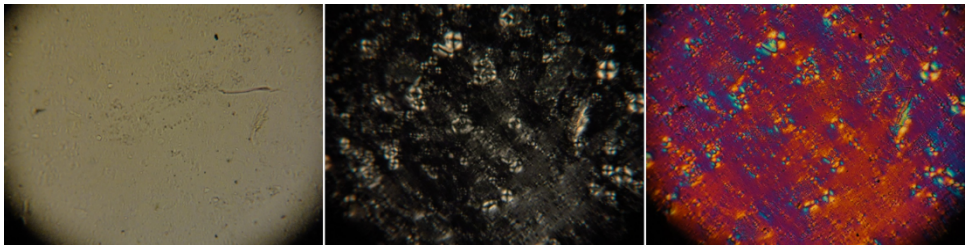

Figure 42. Polarized light microscopy of spherulites in ISDU lipid sample
Polarized light microscopy (10x magnification) of a 10mg DPPC sample with 2% by weight Gramicidin D prepared in 5% D_2O and subjected to 24 h ISDU at 25°C. The bright field image (left) and the crossed polarizers image (middle) and crossed polarizers with quartz waveplate image (right) are compared. Some samples like this one showed birefringent spherulites that indicate an unknown source of contamination that is not apparent in the bright field image.

Probing the Hydration of Lipid Membranes with Metal Carbonyl labels Using a Dual Approach of Two-dimensional Infrared (2DIR) Spectroscopy and Electron Nuclear Double

Another proposed method of studying the model lipid phases is introduction of metal carbonyl labels such as that discussed in Appendix A. The following is part of a minor user proposal with ACERT.

Metal carbonyl labels such as chromium carbonyl complexes exhibits a strong response in both 2DIR[99,100] and ENDOR spectroscopy[101–103] enabling a dual spectroscopic approach to study the hydration of lipids membranes and membrane proteins. A vibrational probe label can localize the signal to only the water molecules directly hydrogen-bonded to the label, providing specific information on the local

hydration dynamics.[99] The hydration sensitivity of a metal carbonyl (chromium tricarbonyl) label is illustrated by the solvatochromatic shift shown in **Figure *28***.

Molecular probes used in visible spectroscopy are sensitive to the entire dielectric environment around the probe and are, thus, essentially nonlocal probes of the hydration, which have led to controversial interpretations in the literature. In contrast, vibrational and ENDOR (electron-nuclear double resonance) molecular labels are local probes and only sensitive to the structure and dynamics of the water molecules directly hydrogen-bonded to the label. The metal carbonyl 2DIR and ENDOR label thus offers insight into the local hydration structure and dynamics of a targeted site.

In addition to being a vibrational probe, metal carbonyl labels can also provide a strong ENDOR response depending in the spin state of the metal.[101] A proposed project will develop a new technique for probing the structure and dynamics of the hydration water based on an unambiguous, dual spectroscopic approach 2DIR spectroscopy will provide information on the timescale with which hydrogen bonds are formed and broken in the liquid state. ENDOR spectroscopy will analyze the same sample, frozen into a glassy state, and will report in detail on the structure and geometry of the metal carbonyl probe and the closely hydrogen-bonded waters. The information from both 2DIR and ENDOR therefore are complementary and help form a complete picture of the structure–dynamics relationship of local hydrogen-bonding network at the site of the metal carbonyl probe.

In initial studies, the metal carbonyl probe will be attached to the phospholipid headgroup of lipid membranes, as shown in **Figure *43***,[104,105] and aligned lipid samples that contain the metal carbonyl label will be produced with differing lipid composition

and hydration levels through isopotential spin-dry ultracentrifugation (ISDU).[106,107] This will provide information on the interplay between the hydration dynamics and the lipid composition phase diagram as well as the effect of water confinement on the hydration dynamics, i.e. how the dynamics of the water molecules in the first solvation shell hydrogen-bonded to the label is affected by the thickness of the water layer between the stacked lipid bilayers. Note that Q-band ENDOR on oriented samples (such as the aligned membrane) offers very detailed resolution of structural changes, as demonstrated previously for different spin centers.[108]

To further extend the methodology, we will further utilize Electron Spin Echo Envelope Modulation (ESEEM) spectroscopy. This third technique has been usefully applied with other types of probes to study the local density of both water and lipid molecules that are near but not directly hydrogen bonded to the label.[109] The ESEEM experiments will be complimented by 2DIR experiments on the water OH vibrations providing a comparable non-local probe on the hydration dynamics offering even further information on the hydration structure of lipid bilayers. Finally, we note that the chemistry involved in the labeling scheme is very general, and can easily be adapted to transform our multi-spectroscopic approach into a tool for site-directed labeling and probing of the hydration dynamics on the surface of a protein.

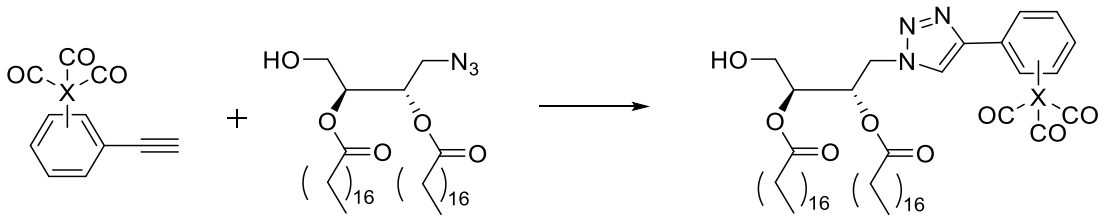

Figure 43. Synthesis of tricarbonyl benzene metal-tagged lipid.
The metal is denoted by X in the figure.

Appendix C: 2DIR Studies on the Role of Zundel and Eigen Cations in Aqueous Proton Transfer

with Ashley Stingel (Ph.D. '16)

Aqueous proton transfer is at the heart of important biology. There are a host of important proton transfer mechanisms that already have significant theoretical and experimental attention. For example, cytochrome c oxidase, a proton pump, is a part of the mitochondrial electron transport chain and cellular respiration. Aquaporin-1 is a transmembrane protein that facilitates rapid water exchange across a membrane, but blocks the diffusion of all cations, including protons. Carbonic anhydrase catalyzes the conversion of carbon dioxide to bicarbonate and an excess proton, facilitating CO_2 transport, gluconeogenesis, uriogenesis, and bicarbonate buffering. The influenza A M2 channel is a proton-selective ion channel and an archetypal drug target. Gramicidin is a set of antibiotic transmembrane proteins that allow monovalent cations to pass through bacterial cell membranes. The green fluorescent protein (GFP) mechanism involves light-driven conversion between the neutral and anionic chromophore via excited state proton transfer (ESPT). Even crucial biological functions such as ATP synthesis are dependent on proton transfer.

Besides biological applications, studying proton transfer has a host of other important applications such as acid-base chemistry, redox reactions, materials for fuel cells, and understanding of fundamental processes such as the autoionization of water. As a physical problem, proton transfer in water is a fascinating problem.

Proton mobility in water is anomalously fast, as can be shown by comparison with similarly sized cations. The Stokes-Einstein relation relates diffusion of an ion with

the solvent friction: $D=kT/f$. Stokes's relation further relates the friction with the radius of the ion, α, and the viscosity of the solvent, η: $f=6\pi a\eta$. For small ions, α is the hydrodynamic radius (a.k.a. the Stokes radius) and not the ionic radius, because small ions have very high electric fields due to small surface area ($E\propto ze/r^2$) and drag along many solvent molecules. Therefore, diffusion should be comparable for the smallest possible protonated water cluster (H_3O^+) with a radius of ~3 Å and hydrated K^+ with a hydrodynamic radius of 3.3 Å. However, **Table *3*** shows that H^+ (and OH^-) mobility is anomalously high and cannot be explained by hydrodynamic diffusion. The H_3O^+ water cluster moves ~6.5 times faster than expected and the OH^- ion moves ~3.3 times faster than expected. Similar results can be shown for ion mobility in an electric field.

Table 3. Diffusion coefficients in water
Diffusion coefficients, D, in water at 298 K in units 10^{-9} m^2/s. Proton and hydroxide mobility are anomalously high in relation to comparably sized ions. Similar results can be shown for ion mobilities within an electric field.[110]

Diffusion coefficients in water at 298K, D (10^{-9} m^2 s^{-1})	
H^+	9.31
Na^+	1.33
K^+	1.96
OH^-	5.03
Cl^-	2.03
Br^-	2.08
Water	2.26

The basic explanation for the abnormally high mobility of the proton and hydroxide is proton hopping—the passing of the protons from one water molecule to another. The movement of the charge and not the ion itself was first proposed in 1806 through a stroke of brilliance by Freiherr Christian J. Theodor von Grotthuss, who studied the galvanic decomposition of water into hydrogen and oxygen gases using Volta's recently created battery.[111,112] Grotthuss proposed that water is decomposed into two oppositely charged particles that move to the respective electrodes. At a time when water was thought to contain only one hydrogen atom and one oxygen atom, Grotthuss guessed that the H must be transferred between an OH molecule and a dissociated O along a chain of water molecules that followed something like the (yet to be discovered) Faraday lines of electric field between the two electrodes. The consecutive transfers of H between OH and O molecules facilitated the charge transfer.

Discovery of tetrahedral hydrogen-bonding of water and the Zundel ($H_9O_4^+$) and Eigen ($H_5O_2^+$) cations updated the Grotthuss mechanism.[113,114] In the modern mechanism, the proton hop is followed by reorientation to a new equilibrium and further priming for the next hop. As the mechanism became more refined, one important question was: What is the rate limiting step of aqueous proton transfer?

Agmon theorized in 1995 that the speed of the actual proton motion indicated that the rate-limiting step must be the solvent reorganization.[115] The breaking of a hydrogen bond in the secondary shell of waters around the excess proton primes the solvent structure for proton transfer through the Zundel cation. Agmon summarized his theory with a picture of Moses parting the Red Sea:

> *"Concluding, proton migration may be envisioned as a process propelled by hydrogen-bond cleavage, taking place in front of the moving proton, and hydrogen-bond formation in its back. If an allegoric description is required, it may be found in Moses crossing the sea, with waves parting before him and reclosing behind his track."*[115]

Agmon was followed shortly by a team headed by Parrinello, who used ab initio path integral MD simulations that confirmed Agmon's intuition that the rate-limiting step for the transfer of the excess proton is the concerted dynamics of the proton's second hydration shell.[116,117] Despite some continuing controversy, there is general agreement on the rate-limiting role of the second-shell solvation on aqueous proton transfer. One important remaining question is: What is the equilibrium structure of the excess proton in water?

Quantum Car-Parrinello simulations found both the Eigen ($H_5O_2^+$) and Zundel ($H_9O_4^+$) cations.[118] While classical simulations slightly favored the Zundel cation, the relative difference was less than kT and the lowest vibrational state reached the top of the classical barrier with the zero-point energy.

Some theorists found that the equilibrium Zundel cation passed through an intermediate Eigen cation only briefly during proton transfer,[119–122] while others concluded that there is a local energy minimum at the Eigen and the Zundel is the intermediate state.[123,124] In this view, any of the three protons on the Eigen cation fluctuate between the oxygen of the Eigen cation and the oxygen of the nearest neighboring water. Random fluctuations select one of these protons to begin to rattle back and forth between the Eigen oxygen and neighboring oxygen in a "special pair

dance" that forms a Zundel cation.[125] Finally, the proton moves to the new oxygen and forms a new Eigen cation. Ab initio MD simulations of the vertical ionization potential of acidic water photoelectron spectroscopy better match the Eigen cation as equilibrium state.[126]

One of the key simulation evidences for the Eigen equilibrium state is the shift of the radial distribution function from two slight maxima before proton transfer to one maximum immediately after proton transfer.[124] However, radial pair distribution functions are ideal for solids with fixed structure, but average out most of the subtle features of a liquid. Radial pair distribution functions are also relatively insensitive to the applied theoretical potential and are experimentally determined.[127]

Therefore, there is great need for experimental evidence on the role of Eigen and Zundel cations in aqueous proton transfer. Gas-phase vibrational spectra of argon cluster-mediated trapped protonated water clusters mapped the Zundel and Eigen stretch and bends. While other gas-phase work was done by others, comprehensive identification across the mid-infrared region was accomplished by the Johnson group.[128] The Zundel proton shuttling resonates at about 1100 cm^{-1}; the Zundel bend resonates at 1760 cm^{-1}; and the Zundel stretch resonates at 3175 cm^{-1}. The Eigen stretch appears at 2500-2900 cm^{-1}.

Liquid-phase ultrafast vibrational spectroscopy has followed the gas-phase work. Transient absorption of the stretching region of a 5 M HCl sample when pumping the Eigen stretch band at 2935 cm^{-1} found interconversion between the Eigen ($H_5O_2^+$) and Zundel ($H_9O_4^+$) cations was faster than the time resolution of the experiment (100 fs).[129] Similar work pumping 40 μm 0.5 M HCl solutions at 2800 cm^{-1} with 150 fs pulses

found vibrational lifetimes of 170 fs for the deconvoluted Eigen proton.[130] Recent work on 4 M HCl solutions between 1 mm CaF_2 windows (with no spacer) from the Tokmakoff group pumped with 45 fs broadband pulses centered at 3150 cm^{-1} (i.e. the Zundel stretch) and probed with <70fs Continuum IR pulses spanning 1500 to 4000 cm^{-1} to collect transient absorption and 2DIR spectra.[9] The time-dependent shift of the cross-peak of the Zundel stretch (3200 cm^{-1}) and Zundel bend (1760 cm^{-1}) had a lifetime of at least 480 fs, which indicated that the Zundel complex is more than an intermediate state in aqueous proton transfer.

However, previous work has been limited to probing above 1500 cm^{-1} and pumping the Zundel stretch, which overlaps significantly with the water stretch and possibly some Eigen stretch. Potentially distinct features could be achieved by pumping at frequencies other than the OH stretch region. We propose three pump frequencies: the Zundel proton shuttling (1200 cm^{-1}), the Zundel bend (1760 cm^{-1}) and the Eigen stretch (2750 cm^{-1}). By pumping regions where the Zundel, Eigen, and water species do not overlap, unambiguous spectra can be collected across the detectable range (1000 to 4000 cm^{-1}). ATR-FTIR and transmission FTIR studies of water and varying concentrations of HCl are shown in the below figures. Temperature control shown in **Figure *47*** also allows study of the hot ground state found in literature.[9]

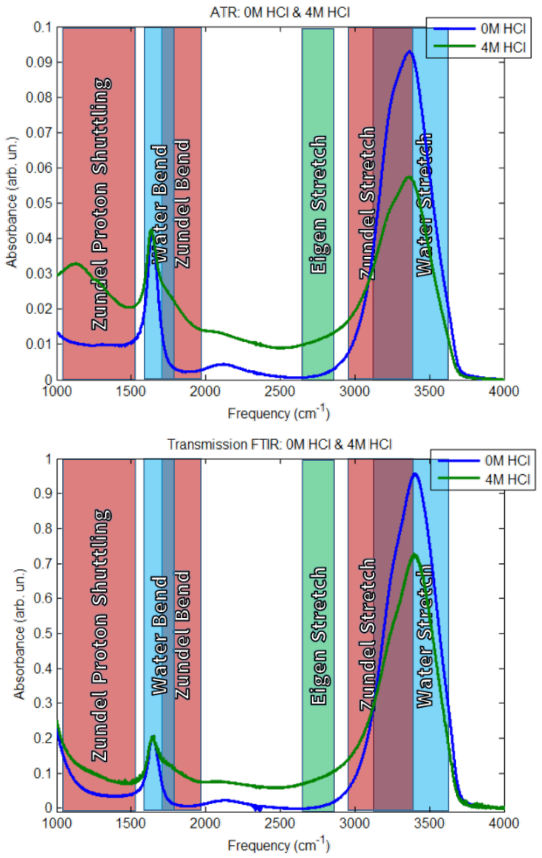

Figure 44. ATR-FTIR and transmission FTIR of HCl solutions

ATR-FTIR (top) and transmission FTIR (middle) of 0 M and 4 M aqueous HCl solutions with peak assignments. Difference spectrum (bottom) of ATR-FTIR of 0 M and 4 M aqueous HCl solutions with several peak frequencies labeled. The ATR used a Germanium window. The transmission cell used two 1 mm CaF2 windows with no spacer.

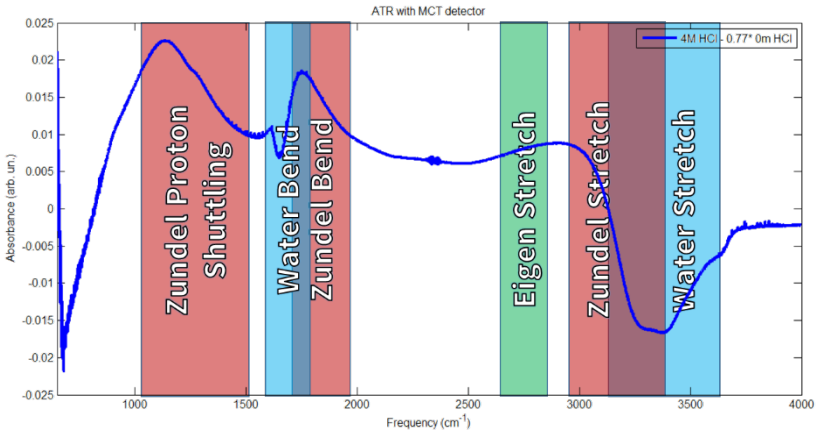

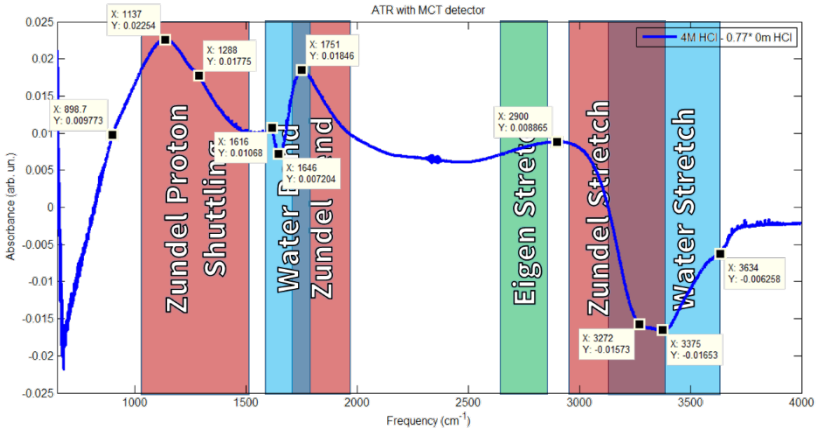

Figure 45. ATR-FTIR difference spectra HCl solutions
Difference spectra of ATR-FTIR of 0 M and 4 M aqueous HCl solutions without (top) and with (bottom) extrema frequencies labeled and with frequency region assignments. A scalar was multiplied by the 0 M HCl spectrum before subtraction to most closely match literature.[9]

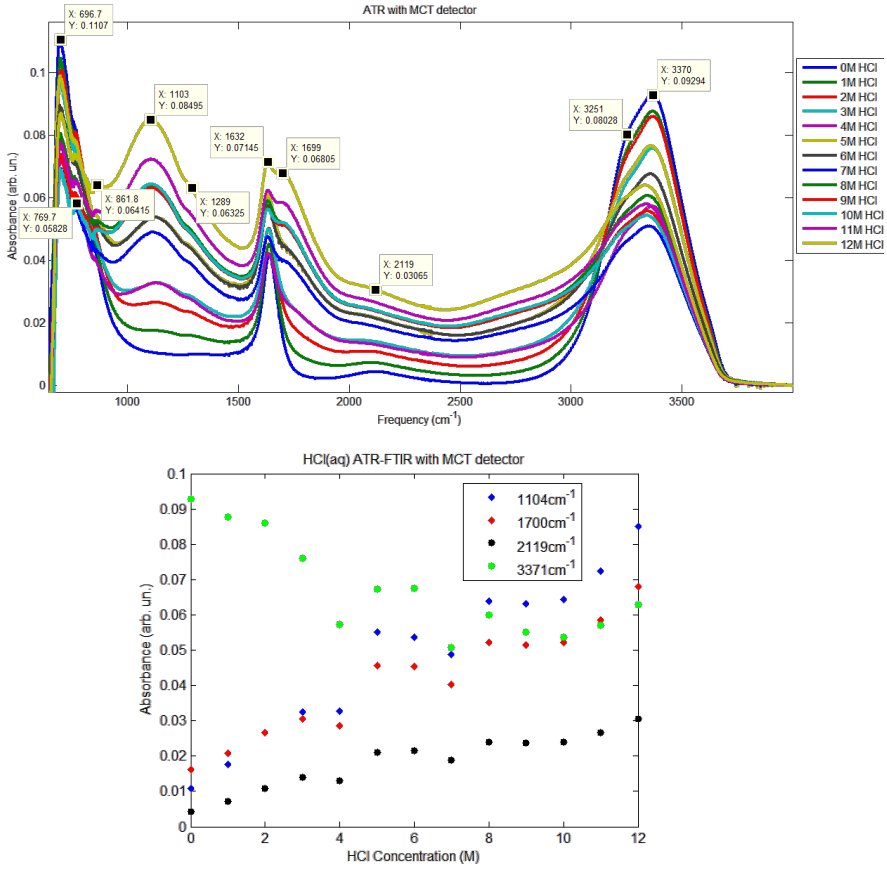

Figure 46. ATR-FTIR peak amplitude vs. concentration for HCl solutions
ATR-FTIR spectra (top) for HCl solutions

from 0 M to 12 M (in 1 M HCl increments). Amplitude-concentration correlation for several peak frequencies (bottom). While Beer's Law does hold, the noise in the data from concentration uncertainty is problematic. Evaporation during collection of samples open to the air during ATR-FTIR spectra is likely one source of uncertainty.

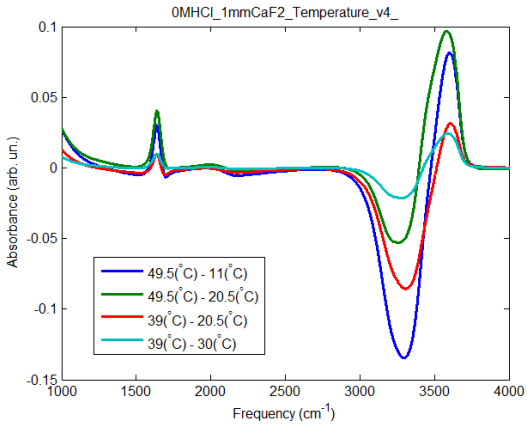

Figure 47. FTIR study of hot ground state of water

Temperature difference FTIR spectra of water (0 M HCl) between 1 mm CaF_2 using homebuilt copper temperature cell.

Deconvolution of the HCl ATR-FTIR spectra was attempted in the hope that Zundel-specific and Eigen-specific spectra could be obtained. MCR (Multivariate Curve Resolution) techniques were adapted from Raman experiments with customized Matlab code downloaded from http://www.mcrals.info/.[131] However, only the two-component deconvolution correlates well with concentration as shown in **Figure *48***. Concentration uncertainty is problematic. Evaporation during collection of samples open to the air during ATR-FTIR spectra is a possible source of uncertainty. Another possible problem is that the equilibrium between Eigen, Zundel, and other species is not weighted strongly. In other words, the noise in the curve deconvolution could overwhelm the subtle predominance of one species.

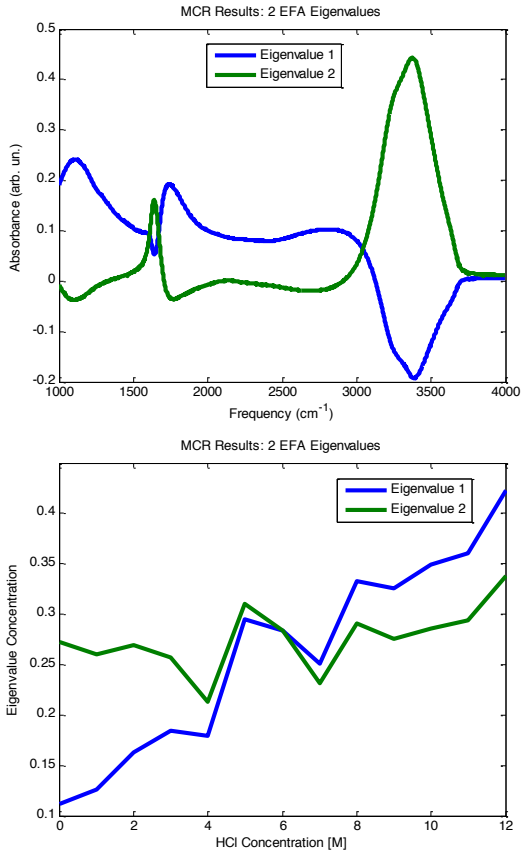

Figure 48. Deconvolution of ATR-FTIR of HCl solutions into two components

ATR-FTIR-MCR (Multivariate Curve Resolution) of HCl solutions from 0 M to 12 M in 1 M increments. Deconvolution into two components. The component spectra (top) and the component weight versus acid concentration (bottom).

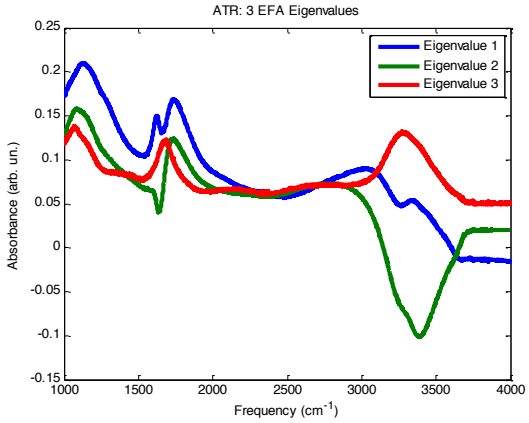

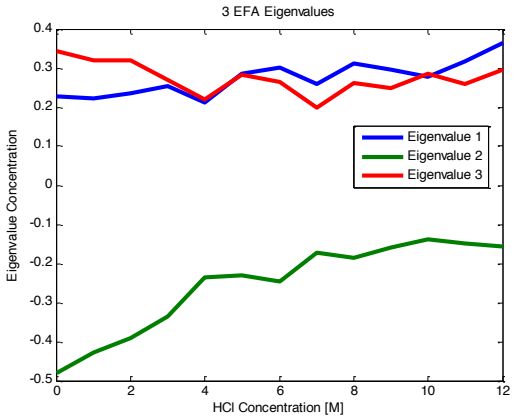

Figure 49. Deconvolution of ATR-FTIR of HCl solutions into three components
ATR-FTIR-MCR (Multivariate Curve Resolution) of HCl solutions from 0 M to 12 M in 1 M increments. Deconvolution into three components. The component spectra (top) and the component weight versus acid concentration (bottom).

To counteract dispersion, several sample window preparations were investigated. Silicon nitride (Si_3N_4) windows can be made very thin while still retaining relative strength. To attach the silicon nitride windows to an aluminum sample window, several glues and epoxies were attempted. Masterbond EP62-1 epoxy was rated for acid resistance, but did not cure well in the confined space or the acid and epoxy and aluminum combination did not work as shown in **Figure *50***.

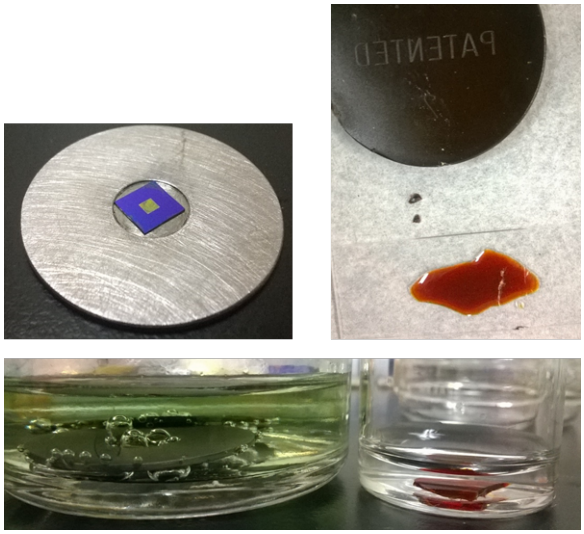

Figure 50. Synopsis of epoxy attachment of silicon nitride windows
Left: Silicon Nitride (Si_3N_4) window (5x5 mm Si frame, with 200nm thick, 1.5x1.5 mm Si_3N_4 window attached with Masterbond EP62-1 Epoxy to custom machined aluminum frame). Right: Masterbond EP62-1 Epoxy sample disk and purchased epoxy after curing. Bottom: Exposure of Si_3N_4 window and cured epoxy to 3 M HCl for 24 h. The window sample reacts while the epoxy alone does not.

The silicon nitride windows were not necessary, as 200 μm thick CaF_2 windows were purchased from Crystran (overstock) and caused minimal dispersion over the frequency range of interest. Samples were successfully made with a 13 mm diameter, 200 μm thick CaF_2 window in front, no spacer, 3 μL of sample, and a 1 mm thick CaF_2 window in back. Sample edges were wrapped with Krytox lubricant (PTFE-based). The Krytox step is optional. Samples were then wrapped in Parafilm and finally loaded in Harrick Scientific FTIR flow cells with the 200 μm thick CaF_2 window in the front of the sample. The Harrick Scientific demountable liquid FTIR flow cell (DLC2 PTFE transmission liquid cell Stock #: DLC-F13-125) is designed for samples using 2 mm thick windows and needs an extra o-ring for the smaller samples. One Viton o-ring

(Stock #: ORV-012; 0.504 OD (13mm), 0.364 ID) was placed after the sample and two Viton o-rings were placed in front of the sample. The sample was screwed together and the flow cell ports were also wrapped in Parafilm.

Preliminary 2DIR and transient absorption spectra of 4 M HCl samples were collected successfully using the CaF_2 window samples and compared to similarly prepared pure water samples. The preliminary results show promising signs of distinguishable Eigen, Zundel, and water contributions. Further data collection is necessary before publication.

Bibliography

(1) Ball, P. Water as a Biomolecule. *Chemphyschem* **2008**, *9* (18), 2677–2685.

(2) Ball, P. Water as an Active Constituent in Cell Biology. *Chem. Rev.* **2008**, *108* (1), 74–108.

(3) Jungwirth, P. Biological Water or Rather Water in Biology? *J. Phys. Chem. Lett.* **2015**, *6* (13), 2449–2451.

(4) Novak, A. Hydrogen Bonding in Solids Correlation of Spectroscopic and Crystallographic Data. In *Large Molecules*; Springer: Berlin, Heidelberg, 1974; pp 177–216.

(5) Bakker, H. J.; Skinner, J. L. Vibrational Spectroscopy as a Probe of Structure and Dynamics in Liquid Water. *Chem. Rev.* **2010**, *110* (3), 1498–1517.

(6) Pieniazek, P. a; Tainter, C. J.; Skinner, J. L. Surface of Liquid Water: Three-Body Interactions and Vibrational Sum-Frequency Spectroscopy. *J. Am. Chem. Soc.* **2011**, *133* (27), 10360–10363.

(7) Auer, B. M.; Skinner, J. L. Water: Hydrogen Bonding and Vibrational Spectroscopy, in the Bulk Liquid and at the Liquid/vapor Interface. *Chem. Phys. Lett.* **2009**, *470* (1–3), 13–20.

(8) Mandal, A.; Ramasesha, K.; De Marco, L.; Tokmakoff, A. Collective Vibrations of Water-Solvated Hydroxide Ions Investigated with Broadband 2DIR Spectroscopy. *J. Chem. Phys.* **2014**, *140* (20), 204508.

(9) Thamer, M.; De Marco, L.; Ramasesha, K.; Mandal, A.; Tokmakoff, A. Ultrafast 2D IR Spectroscopy of the Excess Proton in Liquid Water. *Science*

2015, *350* (6256), 78–82.

(10) McGuire, J. A.; Shen, Y. R. Ultrafast Vibrational Dynamics at Water Interfaces. *Science* **2006**, *313* (5795), 1945–1948.

(11) Shi, L.; Skinner, J. L.; Jansen, T. L. C. Two-Dimensional Infrared Spectroscopy of Neat Ice I H. *Phys. Chem. Chem. Phys.* **2016**, *18* (5), 3772–3779.

(12) Levy, Y.; Onuchic, J. N. Water Mediation in Protein Folding and Molecular Recognition. *Annu. Rev. Biophys. Biomol. Struct.* **2006**, *35*, 389–415.

(13) Fuxreiter, M.; Mezei, M.; Simon, I.; Osman, R. Interfacial Water as A "hydration Fingerprint" in the Noncognate Complex of BamHI. *Biophys. J.* **2005**, *89* (2), 903–911.

(14) Pal, S. K.; Zhao, L.; Xia, T.; Zewail, A. H. Site- and Sequence-Selective Ultrafast Hydration of DNA. *Proc. Natl. Acad. Sci. U. S. A.* **2003**, *100* (24), 13746–13751.

(15) Pal, S. K.; Zhao, L.; Zewail, A. H. Water at DNA Surfaces: Ultrafast Dynamics in Minor Groove Recognition. *Proc. Natl. Acad. Sci. U. S. A.* **2003**, *100* (14), 8113–8118.

(16) Halle, B.; Denisov, V. P. Water and Monovalent Ions in the Minor Groove of B-DNA Oligonucleotides as Seen by NMR. *Biopolymers* **1998**, *48* (4), 210–233.

(17) Halle, B.; Nilsson, L. Does the Dynamic Stokes Shift Report on Slow Protein Hydration Dynamics? *J. Phys. Chem. B* **2009**, *113* (24), 8210–8213.

(18) Furse, K. E.; Corcelli, S. a. The Dynamics of Water at DNA Interfaces: Computational Studies of Hoechst 33258 Bound to DNA. *J. Am. Chem. Soc.*

2008, *130* (39), 13103–13109.

(19) Yang, M.; Szyc, Ł.; Elsaesser, T. Decelerated Water Dynamics and Vibrational Couplings of Hydrated DNA Mapped by Two-Dimensional Infrared Spectroscopy. *J. Phys. Chem. B* **2011**, *115* (44), 13093–13100.

(20) Furse, K. E.; Corcelli, S. A. Molecular Dynamics Simulations of DNA Solvation Dynamics. *J. Phys. Chem. Lett.* **2010**, *1* (12), 1813–1820.

(21) Furse, K. E.; Corcelli, S. a. Effects of an Unnatural Base Pair Replacement on the Structure and Dynamics of DNA and Neighboring Water and Ions. *J. Phys. Chem. B* **2010**, *114* (30), 9934–9945.

(22) Greve, C.; Elsaesser, T. Ultrafast Two-Dimensional Infrared Spectroscopy of Guanine-Cytosine Base Pairs in DNA Oligomers. *J. Phys. Chem. B* **2013**.

(23) Eisenthal, K. B. Liquid Interfaces Probed by Second-Harmonic and Sum-Frequency Spectroscopy. *Chem. Rev.* **1996**, *96* (4), 1343–1360.

(24) Stiopkin, I. V; Weeraman, C.; Pieniazek, P. a; Shalhout, F. Y.; Skinner, J. L.; Benderskii, A. V. Hydrogen Bonding at the Water Surface Revealed by Isotopic Dilution Spectroscopy. *Nature* **2011**, *474* (7350), 192–195.

(25) Jungwirth, P. Physical Chemistry: Water's Wafer-Thin Surface. *Nature* **2011**, *474* (7350), 168–169.

(26) Gopalakrishnan, S.; Liu, D.; Allen, H. C.; Kuo, M.; Shultz, M. J. Vibrational Spectroscopic Studies of Aqueous Interfaces: Salts, Acids, Bases, and Nanodrops. *Chem. Rev.* **2006**, *106* (4), 1155–1175.

(27) Jena, K. C.; Covert, P. A.; Hore, D. K. The Effect of Salt on the Water Structure at a Charged Solid Surface: Differentiating Second- and Third-Order Nonlinear

Contributions. *J. Phys. Chem. Lett.* **2011**, *2* (9), 1056–1061.

(28) Moad, A. J.; Simpson, G. J. A Unified Treatment of Selection Rules and Symmetry Relations for Sum-Frequency and Second Harmonic Spectroscopies. *J. Phys. Chem. B* **2004**, *108* (11), 3548–3562.

(29) Fu, L.; Wang, Z.; Yan, E. C. Y. Chiral Vibrational Structures of Proteins at Interfaces Probed by Sum Frequency Generation Spectroscopy. *Int. J. Mol. Sci.* **2011**, *12* (12), 9404–9425.

(30) Simpson, G. J. Molecular Origins of the Remarkable Chiral Sensitivity of Second-Order Nonlinear Optics. *Chemphyschem* **2004**, *5* (9), 1301–1310.

(31) Wang, H.-F. In Situ Measurement of Chirality of Molecules and Molecular Assemblies with Surface Nonlinear Spectroscopy. In *Comprehensive Chiroptical Spectroscopy: Instrumentation, Methodologies, and Theoretical Simulations*; 2011; Vol. 1, pp 373–407.

(32) Verbiest, T.; Kauranen, M.; Persoons, a.; Ikonen, M.; Kurkela, J.; Lemmetyinen, H. Nonlinear Optical Activity and Biomolecular Chirality. *J. Am. Chem. Soc.* **1994**, *116* (13), 9203–9205.

(33) Haupert, L. M.; Simpson, G. J. Chirality in Nonlinear Optics. *Annu. Rev. Phys. Chem.* **2009**, *60*, 345–365.

(34) Cameron, R.; Tabisz, G. C. Observation of Two-Photon Optical Rotation by Molecules. *Mol. Phys.* **1997**, *90* (2), 159–164.

(35) Mesnil, H.; Hache, F. Experimental Evidence of Third-Order Nonlinear Dichroism in a Liquid of Chiral Molecules. *Phys. Rev. Lett.* **2000**, *85* (20), 4257–4260.

(36) Alexandre, M.; Lemercier, G.; Andraud, C.; Mesnil, H.; Schanne-Klein, M. C.; Hache, F. Third-Order Nonlinear Circular Dichroism in a Liquid of Chiral Molecules. *Synth. Met.* **2002**, *127* (1–3), 135–138.

(37) Petralli-Mallow, T.; Wong, T. M.; Byers, J. D.; Yee, H. I.; Hicks, J. M. Circular Dichroism Spectroscopy at Interfaces: A Surface Second Harmonic Generation Study. *J. Phys. Chem.* **1993**, *97* (7), 1383–1388.

(38) Byers, J. D.; Yee, H. I.; Hicks, J. M. A Second Harmonic Generation Analog of Optical Rotatory Dispersion for the Study of Chiral Monolayers. *J. Chem. Phys.* **1994**, *101* (7), 6233.

(39) Maki, J. J.; Verbiest, T.; Kauranen, M.; Van Elshocht, S.; Persoons, a. Comparison of Linearly and Circularly Polarized Probes of Second-Order Optical Activity of Chiral Surfaces. *J. Chem. Phys.* **1996**, *105*, 767–772.

(40) Belkin, M. A.; Kulakov, T. A.; Ernst, K.-H.; Yan, L.; Shen, Y. R. Sum-Frequency Vibrational Spectroscopy on Chiral Liquids: A Novel Technique to Probe Molecular Chirality. *Phys. Rev. Lett.* **2000**, *85* (21), 4474–4477.

(41) Wang, J.; Chen, X.; Clarke, M. L.; Chen, Z. Detection of Chiral Sum Frequency Generation Vibrational Spectra of Proteins and Peptides at Interfaces in Situ. *Proc. Natl. Acad. Sci.* **2005**, *102* (14), 4978–4983.

(42) Yan, E. C. Y.; Fu, L.; Wang, Z.; Liu, W. Biological Macromolecules at Interfaces Probed by Chiral Vibrational Sum Frequency Generation Spectroscopy. *Chem. Rev.* **2014**, *114* (17), 8471–8498.

(43) Tong, Y.; Zhao, Y.; Li, N.; Osawa, M.; Davies, P. B.; Ye, S. Interference Effects in the Sum Frequency Generation Spectra of Thin Organic Films. I.

Theoretical Modeling and Simulation. *J. Chem. Phys.* **2010**, *133* (3), 34704.

(44) Wang, H.-F.; Velarde, L.; Gan, W.; Fu, L. Quantitative Sum-Frequency Generation Vibrational Spectroscopy of Molecular Surfaces and Interfaces: Lineshape, Polarization, and Orientation. *Annu. Rev. Phys. Chem.* **2015**, *66* (1), 189–216.

(45) Belkin, M.; Kulakov, T.; Ernst, K.; Han, S.; Shen, Y. Resonant Sum-Frequency Generation in Chiral Liquids. *Opt. Mater. (Amst).* **2002**, *21* (1–3), 1–5.

(46) Okuno, M.; Ishibashi, T. Chirality Discriminated by Heterodyne-Detected Vibrational Sum Frequency Generation. *J. Phys. Chem. Lett.* **2014**, *5* (16), 2874–2878.

(47) Lotze, S.; Versluis, J.; Olijve, L. L. C.; van Schijndel, L.; Milroy, L. G.; Voets, I. K.; Bakker, H. J. Communication: Probing the Absolute Configuration of Chiral Molecules at Aqueous Interfaces. *J. Chem. Phys.* **2015**, *143* (20), 201101.

(48) Nguyen, K. T. An Electronically Enhanced Chiral Sum Frequency Generation Vibrational Spectroscopy Study of Lipid-Bound Cytochrome c. *Chem. Commun.* **2015**, *51* (1), 195–197.

(49) McDermott, M. L.; Petersen, P. B. Robust Self-Referencing Method for Chiral Sum Frequency Generation Spectroscopy. *J. Phys. Chem. B* **2015**, *119* (38), 12417–12423.

(50) Fu, L.; Ma, G.; Yan, E. C. Y. In Situ Misfolding of Human Islet Amyloid Polypeptide at Interfaces Probed by Vibrational Sum Frequency Generation. *J. Am. Chem. Soc.* **2010**, *132* (15), 5405–5412.

(51) Xiao, D.; Fu, L.; Liu, J.; Batista, V. S.; Yan, E. C. Y. Amphiphilic Adsorption of Human Islet Amyloid Polypeptide Aggregates to Lipid/aqueous Interfaces. *J. Mol. Biol.* **2012**, *421* (4–5), 537–547.

(52) Fu, L.; Liu, J.; Yan, E. C. Y. Chiral Sum Frequency Generation Spectroscopy for Characterizing Protein Secondary Structures at Interfaces. *J. Am. Chem. Soc.* **2011**, *133* (21), 8094–8097.

(53) Meister, K.; Lotze, S.; Olijve, L. L. C.; DeVries, A. L.; Duman, J. G.; Voets, I. K.; Bakker, H. J. Investigation of the Ice-Binding Site of an Insect Antifreeze Protein Using Sum-Frequency Generation Spectroscopy. *J. Phys. Chem. Lett.* **2015**, 1162–1167.

(54) Fu, L.; Zhang, Y.; Wei, Z.; Wang, H. Intrinsic Chirality and Prochirality at Air/R-(+)- and S-(-)-Limonene Interfaces: Spectral Signatures With Interference Chiral Sum-Frequency Generation Vibrational Spectroscopy. *Chirality* **2014**, *26* (9), 509–520.

(55) Wei, F.; Xu, Y.; Guo, Y.; Liu, S.; Wang, H. Quantitative Surface Chirality Detection with Sum Frequency Generation Vibrational Spectroscopy: Twin Polarization Angle Approach. *Chinese J. Chem. Phys.* **2009**, *22* (6), 592–600.

(56) Stokes, G. Y.; Gibbs-Davis, J. M.; Boman, F. C.; Stepp, B. R.; Condie, A. G.; Nguyen, S. T.; Geiger, F. M. Making "sense" of DNA. *J. Am. Chem. Soc.* **2007**, *129* (24), 7492–7493.

(57) Belkin, M. A.; Shen, Y. R. Non-Linear Optical Spectroscopy as a Novel Probe for Molecular Chirality. *Int. Rev. Phys. Chem.* **2005**, *24* (2), 257–299.

(58) Anglin, T. C.; Massari, A. M. Polarization-Multiplexed Vibrational Sum

Frequency Generation for Comprehensive Simultaneous Characterization of Interfaces. *Opt. Lett.* **2012**, *37* (10), 1754–1756.

(59) Pászti, Z.; Wang, J.; Clarke, M. L.; Chen, Z. Sum Frequency Generation Vibrational Spectroscopy Studies of Protein Adsorption on Oxide-Covered Ti Surfaces. *J. Phys. Chem. B* **2004**, *108* (23), 7779–7787.

(60) Han, Y.; Hsu, J.; Ge, N.-H.; Potma, E. O. Polarization-Sensitive Sum-Frequency Generation Microscopy of Collagen Fibers. *J. Phys. Chem. B* **2015**, *119* (8), 3356–3365.

(61) Rocha-Mendoza, I.; Yankelevich, D. R.; Wang, M.; Reiser, K. M.; Frank, C. W.; Knoesen, A. Sum Frequency Vibrational Spectroscopy: The Molecular Origins of the Optical Second-Order Nonlinearity of Collagen. *Biophys. J.* **2007**, *93* (12), 4433–4444.

(62) Schwabe, J. W. The Role of Water in Protein-DNA Interactions. *Curr. Opin. Struct. Biol.* **1997**, *7* (1), 126–134.

(63) Jayaram, B.; Jain, T. The Role of Water in Protein-DNA Recognition. *Annu. Rev. Biophys. Biomol. Struct.* **2004**, *33* (1), 343–361.

(64) Privalov, P. L.; Dragan, A. I.; Crane-Robinson, C.; Breslauer, K. J.; Remeta, D. P.; Minetti, C. A. S. A. What Drives Proteins into the Major or Minor Grooves of DNA? *J. Mol. Biol.* **2007**, *365* (1), 1–9.

(65) Spitzer, G. M.; Fuchs, J. E.; Markt, P.; Kirchmair, J.; Wellenzohn, B.; Langer, T.; Liedl, K. R. Sequence-Specific Positions of Water Molecules at the Interface between DNA and Minor Groove Binders. *ChemPhysChem* **2008**, *9* (18), 2766–2771.

(66) Drew, H. R.; Dickerson, R. E. Structure of a B-DNA Dodecamer. III. Geometry of Hydration. *J. Mol. Biol.* **1981**, *151* (3), 535–556.

(67) Kopka, M. L.; Fratini, A. V.; Drew, H. R.; Dickerson, R. E. Ordered Water Structure around a B-DNA Dodecamer. A Quantitative Study. *J. Mol. Biol.* **1983**, *163* (1), 129–146.

(68) Schneider, B.; Cohen, D.; Berman, H. M. Hydration of DNA Bases: Analysis of Crystallographic Data. *Biopolymers* **1992**, *32* (7), 725–750.

(69) Egli, M.; Tereshko, V.; Teplova, M.; Minasov, G.; Joachimiak, A.; Sanishvili, R.; Weeks, C. M.; Miller, R.; Maier, M. A.; An, H.; et al. X-Ray Crystallographic Analysis of the Hydration of A- and B-Form DNA at Atomic Resolution. *Biopolymers* **1998**, *48* (4), 234–252.

(70) Tereshko, V.; Minasov, G.; Egli, M. A "Hydrat-Ion" Spine in a B-DNA Minor Groove. *J. Am. Chem. Soc.* **1999**, *121* (March), 3590–3595.

(71) Chen, S. H.; Liu, L.; Chu, X.; Zhang, Y.; Fratini, E.; Baglioni, P.; Faraone, A.; Mamontov, E. Experimental Evidence of Fragile-to-Strong Dynamic Crossover in DNA Hydration Water. *J. Chem. Phys.* **2006**, *125* (17).

(72) Denisov, V. P.; Carlström, G.; Venu, K.; Halle, B. Kinetics of DNA Hydration. *J. Mol. Biol.* **1997**, *268* (1), 118–136.

(73) Liepinsh, E.; Otting, G.; Wüthrich, K. NMR Observation of Individual Molecules of Hydration Water Bound to DNA Duplexes: Direct Evidence for a Spine of Hydration Water Present in Aqueous Solution. *Nucleic Acids Res.* **1992**, *20* (24), 6549–6553.

(74) Franck, J. M.; Ding, Y.; Stone, K.; Qin, P. Z.; Han, S. Anomalously Rapid

Hydration Water Diffusion Dynamics Near DNA Surfaces. *J. Am. Chem. Soc.* **2015**, *137* (37), 12013–12023.

(75) Szyc, Ł.; Yang, M.; Nibbering, E. T. J.; Elsaesser, T. Ultrafast Vibrational Dynamics and Local Interactions of Hydrated DNA. *Angew. Chem. Int. Ed. Engl.* **2010**, *49* (21), 3598–3610.

(76) Duboué-Dijon, E.; Fogarty, A. C.; Hynes, J. T.; Laage, D. Dynamical Disorder in the DNA Hydration Shell. *J. Am. Chem. Soc.* **2016**, *138* (24), 7610–7620.

(77) Denisov, V. P.; Halle, B. Sequence-Specific Binding of Counterions to B-DNA. *Proc. Natl. Acad. Sci. U.S.A.* **2000**, *97* (2), 629–633.

(78) Lowe, R. D.; Pellow, M. a.; Stack, T. D. P.; Chidsey, C. E. D. Deposition of Dense Siloxane Monolayers from Water and Trimethoxyorganosilane Vapor. *Langmuir* **2011**, *27* (16), 9928–9935.

(79) Li, Z.; Weeraman, C. N.; Azam, M. S.; Osman, E.; Gibbs-Davis, J. M. The Thermal Reorganization of DNA Immobilized at the Silica/buffer Interface: A Vibrational Sum Frequency Generation Investigation. *Phys. Chem. Chem. Phys.* **2015**, *17* (19), 12452–12457.

(80) Du, Quan; Freysz, Eric, Shen, Y. R. Surface Vibrational Spectroscopic Studies of Hydrogen Bonding and Hydrophobicity. *Science (80-.).* **1994**, *264*, 826–828.

(81) Scatena, L. F.; Brown, M. G.; Richmond, G. L. Water at Hydrophobic Surfaces: Weak Hydrogen Bonding and Strong Orientation Effects. *Science (80-.).* **2001**, *292* (5518), 908–912.

(82) Yoon, C.; Privé, G. G.; Goodsell, D. S.; Dickerson, R. E. Structure of an Alternating B-DNA Helix and Its Relationship to A-Tract DNA. *Proc. Natl.*

Acad. Sci. U. S. A. **1988**, *85* (17), 6332–6336.

(83) King, J. T.; Kubarych, K. J. Site-Specific Coupling of Hydration Water and Protein Flexibility Studied in Solution with Ultrafast 2D-IR Spectroscopy. *J. Am. Chem. Soc.* **2012**, *134* (45), 18705–18712.

(84) Osborne, D. G.; King, J. T.; Dunbar, J. a.; White, A. M.; Kubarych, K. J. Ultrafast 2DIR Probe of a Host-Guest Inclusion Complex: Structural and Dynamical Constraints of Nanoconfinement. *J. Chem. Phys.* **2013**, *138* (14), 144501.

(85) Anfuso, C. L.; Snoeberger, R. C.; Ricks, A. M.; Liu, W.; Xiao, D.; Batista, V. S.; Lian, T. Covalent Attachment of a Rhenium Bipyridyl CO2 Reduction Catalyst to Rutile TiO2. *J. Am. Chem. Soc.* **2011**, *133* (18), 6922–6925.

(86) Lindahl, C.; Borchardt, P.; Lausmaa, J.; Xia, W.; Engqvist, H. Studies of Early Growth Mechanisms of Hydroxyapatite on Single Crystalline Rutile: A Model System for Bioactive Surfaces. *J. Mater. Sci. Mater. Med.* **2010**, *21* (10), 2743–2749.

(87) Rosenfeld, D. E.; Gengeliczki, Z.; Smith, B. J.; Stack, T. D. P.; Fayer, M. D. Structural Dynamics of a Catalytic Monolayer Probed by Ultrafast 2D IR Vibrational Echoes. *Science* **2011**, *334* (6056), 634–639.

(88) Müller, T. J. J.; Lindner, H. J. Palladium-Copper-Catalyzed Coupling of Tricarbonylchromium-Complexed Phenylacetylene with Iodoarenes – A Facile Access to Alkynyl-Bridged Cr(CO)3-Complexed Benzenes. *Chem. Ber.* **1996**, *129* (6), 607–613.

(89) Chen, E. H.; Walter, S. R.; Nguyen, S. T.; Geiger, F. M. Arylsilanated SiOx

Surfaces for Mild and Simple Two-Step Click Functionalization with Small Molecules and Oligonucleotides. *J. Phys. Chem. C* **2012**, *116* (37), 19886–19892.

(90) Azam, M. S.; Fenwick, S. L.; Gibbs-Davis, J. M. Orthogonally Reactive SAMs as a General Platform for Bifunctional Silica Surfaces. *Langmuir* **2011**, *27*, 741–750.

(91) Pellow, M. A.; Stack, T. D. P.; Chidsey, C. E. D. Squish and CuAAC: Additive-Free Covalent Monolayers of Discrete Molecules in Seconds. *Langmuir* **2013**, *29* (18), 5383–5387.

(92) Zhao, W.; Moilanen, D. E.; Fenn, E. E.; Fayer, M. D. Water at the Surfaces of Aligned Phospholipid Multibilayer Model Membranes Probed with Ultrafast Vibrational Spectroscopy. *J. Am. Chem. Soc.* **2008**, *130* (42), 13927–13937.

(93) Ge, M.; Budil, D. E.; Freed, J. H. ESR Studies of Spin-Labeled Membranes Aligned by Isopotential Spin-Dry Ultracentrifugation: Lipid-Protein Interactions. *Biophys. J.* **1994**, *67* (6), 2326–2344.

(94) Dzikovski, B. G.; Borbat, P. P.; Freed, J. H. Spin-Labeled Gramicidin a: Channel Formation and Dissociation. *Biophys. J.* **2004**, *87* (5), 3504–3517.

(95) Zhao, W.; Moilanen, D. E.; Fenn, E. E.; Fayer, M. D. Water at the Surfaces of Aligned Phospholipid Multibilayer Model Membranes Probed with Ultrafast Vibrational Spectroscopy. *J. Am. Chem. Soc.* **2008**, *130* (42), 13927–13937.

(96) Gruenbaum, S. M.; Skinner, J. L. Vibrational Spectroscopy of Water in Hydrated Lipid Multi-Bilayers. I. Infrared Spectra and Ultrafast Pump-Probe Observables. *J. Chem. Phys.* **2011**, *135* (7), 75101.

(97) Gruenbaum, S. M.; Pieniazek, P. a; Skinner, J. L. Vibrational Spectroscopy of Water in Hydrated Lipid Multi-Bilayers. II. Two-Dimensional Infrared and Peak Shift Observables within Different Theoretical Approximations. *J. Chem. Phys.* **2011**, *135* (16), 164506.

(98) Gruenbaum, S. M.; Skinner, J. L. Vibrational Spectroscopy of Water in Hydrated Lipid Multi-Bilayers. III. Water Clustering and Vibrational Energy Transfer. *J. Chem. Phys.* **2013**, *139* (17), 175103.

(99) Osborne, D. G.; King, J. T.; Dunbar, J. a.; White, A. M.; Kubarych, K. J. Ultrafast 2DIR Probe of a Host-Guest Inclusion Complex: Structural and Dynamical Constraints of Nanoconfinement. *J. Chem. Phys.* **2013**, *138* (14), 144501.

(100) King, J. T.; Kubarych, K. J. Site-Specific Coupling of Hydration Water and Protein Flexibility Studied in Solution with Ultrafast 2D-IR Spectroscopy. *J. Am. Chem. Soc.* **2012**, *134* (45), 18705–18712.

(101) McDyre, L. E.; Hamilton, T.; Murphy, D. M.; Cavell, K. J.; Gabrielli, W. F.; Hanton, M. J.; Smith, D. M. A Cw EPR and ENDOR Investigation on a Series of Cr(I) Carbonyl Complexes with Relevance to Alkene Oligomerization Catalysis: [Cr(CO)4L]+ (L = Ph2PN(R)PPh2, Ph2P(R)PPh2). *Dalton Trans.* **2010**, *39* (33), 7792–7799.

(102) Cummings, D. A.; McMaster, J.; Rieger, A. L.; Rieger, P. H. EPR Spectroscopic and Theoretical Study of Chromium(I) Carbonyl Phosphine and Phosphonite Complexes. *Organometallics* **1997**, *16* (20), 4362–4368.

(103) Krusic, P. .; McLain, S. .; Morton, J. .; Preston, K. .; Le Page, Y. The EPR

Spectrum of CpCr(CO)3 in a Single Crystal of CpMn(CO)3 at 20 K. *J. Magn. Reson.* **1987**, *74* (1), 72–81.

(104) Smith, M. D.; Gong, D.; Sudhahar, C. G.; Reno, J. C.; Stahelin, R. V.; Best, M. D. Synthesis and Convenient Functionalization of Azide-Labeled Diacylglycerol Analogues for Modular Access to Biologically Active Lipid Probes. *Bioconjug. Chem.* **2008**, *19* (9), 1855–1863.

(105) Best, M. D.; Rowland, M. M.; Bostic, H. E. Exploiting Bioorthogonal Chemistry to Elucidate Protein-Lipid Binding Interactions and Other Biological Roles of Phospholipids. *Acc. Chem. Res.* **2011**, *44* (9), 686–698.

(106) Müller, T. J. J.; Lindner, H. J. Palladium-Copper-Catalyzed Coupling of Tricarbonylchromium-Complexed Phenylacetylene with Iodoarenes – A Facile Access to Alkynyl-Bridged Cr(CO)3-Complexed Benzenes. *Chem. Ber.* **1996**, *129* (6), 607–613.

(107) Ge, M.; Budil, D. E.; Freed, J. H. ESR Studies of Spin-Labeled Membranes Aligned by Isopotential Spin-Dry Ultracentrifugation: Lipid-Protein Interactions. *Biophys. J.* **1994**, *67* (6), 2326–2344.

(108) Flores, M.; Isaacson, R. A.; Calvo, R.; Feher, G.; Lubitz, W. Probing Hydrogen Bonding to Quinone Anion Radicals by 1H and 2H ENDOR Spectroscopy at 35 GHz. *Chem. Phys.* **2003**, *294* (3), 401–413.

(109) Gordon-Grossman, M.; Zimmermann, H.; Wolf, S. G.; Shai, Y.; Goldfarb, D. Investigation of Model Membrane Disruption Mechanism by Melittin Using Pulse Electron Paramagnetic Resonance Spectroscopy and Cryogenic Transmission Electron Microscopy. *J. Phys. Chem. B* **2012**, *116* (1), 179–188.

(110) Atkins, P.; de Paula, J. *Physical Chemistry*, 8th ed.; W. H. Freeman and Company: New York, 2006.

(111) de Grotthuss, C. J. T. Sur La Décomposition de L'eau et Des Corps Qu'elle Tient En Dissolution À L'aide de L'électricité. *Galvanique. Ann. Chim* **1806**, *58*, 54–74.

(112) de Grotthuss, C. J. T. Memoir on the Decomposition of Water and of the Bodies That It Holds in Solution by Means of Galvanic Electricity. *Biochim. Biophys. Acta - Bioenerg.* **2006**, *1757* (8), 871–875.

(113) Eigen, M. Proton Transfer, Acid-Base Catalysis, and Enzymatic Hydrolysis. Part I: ELEMENTARY PROCESSES. *Angew. Chemie Int. Ed. English* **1964**, *3* (1), 1–19.

(114) Zundel, G. Easily Polarizable Hydrogen Bonds - Their Interactions with the Environment - IR Continuum and Anomalous Large Proton Conductivity. In *The Hydrogen bond: Recent Developments in Theory and Experiments*; Schuster, P., Zundel, G., Sandorfy, C., Eds.; North-Holland Publishing Company: Amsterdam, 1976; pp 685–766.

(115) Agmon, N. The Grotthuss Mechanism. *Chem. Phys. Lett.* **1995**, *244* (5–6), 456–462.

(116) Tuckerman, M. E.; Laasonen, K.; Sprik, M.; Parrinello, M. Ab-Initio Molecular-Dynamics Simulation Of The Solvation And Transport Of H3o+ And Oh- Ions In Water. *J. Phys. Chem.* **1995**, *99*, 5749–5752.

(117) Tuckerman, M. E.; Laasonen, K.; Sprik, M.; Parrinello, M. Ab Initio Molecular Dynamics Simulation of the Solvation and Transport of Hydronium and

Hydroxyl Ions in Water. *J. Chem. Phys.* **1995**, *103* (1), 150.

(118) Marx, D.; Tuckerman, M. E.; Hutter, J.; Parrinello, M. The Nature of the Hydrated Excess Proton in Water. *Nature* **1999**, *397* (6720), 601–604.

(119) Vuilleumier, R.; Borgis, D. Quantum Dynamics of an Excess Proton in Water Using an Extended Empirical Valence-Bond Hamiltonian. *J. Phys. Chem. B* **1997**, *102* (22), 4261–4264.

(120) Vuilleumier, R.; Borgis, D. An Extended Empirical Valence Bond Model for Describing Proton Transfer in H+(H2O)n Clusters and Liquid Water. *Chem. Phys. Lett.* **1998**, *284* (1–2), 71–77.

(121) Vuilleumier, R.; Borgis, D. Transport and Spectroscopy of the Hydrated Proton: A Molecular Dynamics Study. *J. Chem. Phys.* **1999**, *111* (9), 4251.

(122) Vuilleumier, R.; Borgis, D. An Extended Empirical Valence Bond Model for Describing Proton Mobility in Water. *Isr. J. Chem.* **1999**, *39* (3–4), 457–467.

(123) Markovitch, O.; Agmon, N. Structure and Energetics of the Hydronium Hydration Shells. *J. Phys. Chem. A* **2007**, *111* (12), 2253–2256.

(124) Markovitch, O.; Chen, H.; Izvekov, S.; Paesani, F.; Voth, G. A.; Agmon, N. Special Pair Dance and Partner Selection: Elementary Steps in Proton Transport in Liquid Water. *J. Phys. Chem. B* **2008**, *112* (31), 9456–9466.

(125) Knight, C.; Voth, G. A. The Curious Case of the Hydrated Proton. *Acc. Chem. Res.* **2012**, *45* (1), 101–109.

(126) Winter, B.; Faubel, M.; Hertel, I. V; Pettenkofer, C.; Bradforth, S. E.; Jagoda-Cwiklik, B.; Cwiklik, L.; Jungwirth, P. Electron Binding Energies of Hydrated H3O+ and OH-: Photoelectron Spectroscopy of Aqueous Acid and Base

Solutions Combined with Electronic Structure Calculations. *J. Am. Chem. Soc.* **2006**, *128* (12), 3864–3865.

(127) Kirchner, B. Eigen or Zundel Ion: News from Calculated and Experimental Photoelectron Spectroscopy. *ChemPhysChem* **2007**, *8* (1), 41–43.

(128) Headrick, J. M.; Diken, E. G.; Walters, R. S.; Hammer, N. I.; Christie, R. A.; Cui, J.; Myshakin, E. M.; Duncan, M. A.; Johnson, M. A.; Jordan, K. D. Spectral Signatures of Hydrated Proton Vibrations in Water Clusters. *Science* **2005**, *308* (5729), 1765–1769.

(129) Woutersen, S.; Bakker, H. J. Ultrafast Vibrational and Structural Dynamics of the Proton in Liquid Water. *Phys. Rev. Lett.* **2006**, *96* (13), 138305.

(130) Amir, W.; Gallot, G.; Hache, F.; Bratos, S.; Leicknam, J.-C.; Vuilleumier, R. Time-Resolved Observation of the Eigen Cation in Liquid Water. *J. Chem. Phys.* **2007**, *126* (3), 34511.

(131) Davis, J. G.; Gierszal, K. P.; Wang, P.; Ben-Amotz, D. Water Structural Transformation at Molecular Hydrophobic Interfaces. *Nature* **2012**, *491* (7425), 582–585.